Distributed Fibre Optic Sensing for Strain and Crack-Width Monitoring in Existing Concrete Structures

A laboratory study on surface-bonded DFOS for concrete

Eshan S. Gharpure

TU Delft

This page is intentionally left blank.

Distributed Fibre Optic Sensing for Strain and Crack-Width Monitoring in Existing Concrete Structures

A laboratory study on surface-bonded DFOS for concrete

by

Eshan S. Gharpure

Thesis submitted in the partial fulfillment for the degree of Master of Science in Civil Engineering

at Delft Univerisity of Technology

Faculty of Civil Engineering and Geosciences

Student number: 5945879

Thesis committee

Dr. ir. Y. Yang	Chair	TU Delft
Ir. E. A. A. Borges	Member	TU Delft
Dr. E. Lourens	Member	TU Delft
Dr. C. (Steve) Guo	Member	TU Delft

Cover photo: The Zeeland Bridge (Zeelandbrug), the Netherlands — photograph and edit by E. S. Gharpure, 2025.

An electronic version of this thesis is available at `https://repository.tudelft.nl/`.

TU Delft

This page is intentionally left blank.

Acknowledgement

Embarking on my master's journey at TU Delft has truly been a dream come true. Four years ago, I remember manifesting the dream of studying at this very university, learning under some of the most renowned experts in the field of Civil Engineering. That manifestation has truly worked out. These past two years have been the most challenging and the most important years of my life. TU Delft has not only tested me intellectually but has also nurtured my growth as a person and as an engineer in ways I could have never imagined.

This thesis represents the culmination of my Master's studies and embodies the countless hours of research, experiments, and dedication that I have invested throughout this journey. It has been both a rigorous academic pursuit and a deeply personal journey into a subject I have always been passionate about.

I would like to express my heartfelt gratitude to my Chair, **Yuguang Yang**, for recognizing my potential and entrusting me with such a challenging and inspiring topic. I remember reading one of your research articles three years ago and wishing that someday I would have the chance to work under your guidance. Being able to do my thesis with you has been the realization of that very wish. I have always admired your immense knowledge and wanted to be like you. That thought has been my constant driving force, motivating me to work harder every single day throughout my thesis. Thank you for always coming up with interesting and challenging ideas in our progress meetings and for guiding me with patience and confidence.

My deepest appreciation goes to **Emilia Andrade Borges** for always being there whenever I needed guidance. I have possibly spent the most time working with you among all my supervisors, and I am truly grateful for that. While you were my academic supervisor, I have always considered you a friend with whom I could be open and honest about my progress. Our weekly Tuesday meetings were something I always looked forward to, as I would go home every time feeling motivated and inspired. Thank you for giving me the opportunity to assist you in your fascinating research and for trusting me with the Distributed Fibre Optic Sensors. For me, you have always been a shining example of dedication and hard work, and it would have been impossible to reach this point without your constant support and guidance. I wish you all the very best for your PhD and sincerely hope to stay in touch.

Thank you so much, **Eliz-Mari Lourens**, for your support, for always being available for meetings, and for sharing thoughtful and critical feedback. I was truly honoured to have you as part of my committee. Your expertise in the field of Structural Health Monitoring brought valuable insights that greatly enriched my research.

A very special thanks to **Steve**. You are an absolute gentleman. I truly appreciate your kindness and for always being there for a discussion, whether academic or simply a light-hearted chat. I have always enjoyed our conversations, your humour, and your stories. Most importantly, your perspective on how research should be approached has deeply influenced me. I genuinely look forward to staying connected with you in the future.

I would also like to thank all the PhD candidates from the Concrete Structures section at TU Delft for helping with my quick questions, and the technicians from the Stevin Lab for going above and beyond to ensure that my experiments ran smoothly. Thank you, **Luka**, for helping me during the experiments and for brightening the atmosphere in the lab with your humour. I wish you the very best with your PhD. Thank you, **Achintya**, for always being ready to help, whether early in the morning or late in the evening, and for constantly motivating me and reminding me of my worth. I will always cherish those moments.

To my friends in back in India, thank you for always motivating me and, at times, giving me the space I needed. It is because of your support and understanding that I stayed grounded and sane during this journey. I would also like to thank my fellow **DISS board members** because of whom my time in Delft

was truly enjoyable. Thank you to my family in Delft **Ansh, Dhrumil, Oorv, Ruchita, Ruchira, Nikhil** and **Vedankur** for all the fun moments and for helping me unwind during stressful times. I would like to thank my housemate, **Mohit**, for selflessly cooking for me during the last two crucial months of my thesis and for ensuring that I never went hungry and focus entirely on my research. My deepest thanks to my best friend **Mrugank** for always being there for me, listening to my daily updates, and standing by me through both the good and the tough times. I have shared this journey with you more closely than with anyone else. I also want to extend my thanks to **Nilay** for being the friend who never let me feel alone in this journey, for every pep talk, every laugh, and for always being there. I am forever grateful to my seniors **Atharva**, **Shriyash**, and **Hrishika** for always having my back and guiding me whenever I needed advice or encouragement.

Lastly, I express my deepest gratitude to the most important people in my life, **my parents**, because of whom I am here today. You have supported me through my successes and failures over the past two years. This achievement is entirely dedicated to you. And thanks to my sister **Esha** for always listening to my random conversations and always setting an example for me since childhood.

To those I might have missed, please know that I am equally grateful to you. And to the ones who have been silently wishing for my success, even from afar, I owe you my heartfelt thanks for your prayers, kindness, and for giving me the time and space I needed. This journey has shaped me in ways I could never have imagined. To everyone who has walked even a small part of this path with me, thank you for leaving your mark on my life and for making this dream a reality.

Ganpati Bappa Morya!

Eshan Sanjeev Gharpure
Delft, December 2025

Abstract

Distributed fibre optic sensing (DFOS) offers millimetre-scale, continuous strain measurements that can reveal the longitudinal behaviour and cracking of concrete members far beyond what conventional point sensors can provide. For existing concrete structures, however, its effective use is still limited by three issues: the lack of an evidence-based installation strategy for surface-bonded fibres, limited quantification of how strain is transferred from concrete to the fibre, and incomplete validation of crack widths derived from DFOS under realistic data conditions.

This thesis addresses these gaps through a combination of literature review and laboratory experiments on reinforced-concrete members with surface-bonded DFOS, complemented by a conceptual application to an existing prestressed concrete box-girder bridge. As a qualitative pilot, an inverted T-girder tested in three-point bending is instrumented with DFOS and digital image correlation (DIC). The distributed strain profiles clearly reveal the formation and growth of flexural and shear cracks, but they also expose weaknesses of generic installation guidelines, such as non-uniform adhesive layers, local debonding and data gaps near steep strain gradients. These observations are used to formulate a refined, evidence-based installation strategy for surface-bonded DFOS on concrete.

In a second phase, four reinforced-concrete beams are tested in four-point bending with DFOS, strain gauges and digital image correlation (DIC). Comparisons between DFOS and strain-gauge measurements in both tension and compression show that the fibre systematically underestimates the true concrete surface strain, but with an almost constant ratio for a given installation. This allows a strain-transfer efficiency factor to be identified so that DFOS strains can be converted into realistic concrete strains in the uncracked range. DFOS-based crack widths, obtained by integrating the corrected strain peaks around cracks, are then validated against DIC. For cracks above a practical resolution limit, good agreement is achieved as long as the DFOS signal around each crack is largely intact. When substantial parts of the peak are missing, the error in DFOS crack widths increases and the results become unreliable.

Overall, the thesis demonstrates that surface-bonded DFOS can be used quantitatively for strain and crack-width monitoring in existing concrete structures, provided that installation is treated as a carefully designed process, strain-transfer efficiency is calibrated, and simple data-quality checks are incorporated into the interpretation of crack measurements.

Contents

List of Figures

List of Tables

1

Introduction

1.1. Background on Structural Health Monitoring (SHM) needs for existing structures

The built environment consists of a vast stock of existing structures, including buildings, bridges, tunnels, parking garages and other civil infrastructure. Many of these structures were designed and constructed several decades ago, often according to earlier generations of design codes and with limited consideration for extended service lives or changing usage patterns. Over time, they are subjected to environmental degradation, increased traffic or occupancy loads, accidental actions and time-dependent effects such as creep and shrinkage in concrete. As a result, questions frequently arise about their current condition, residual capacity and remaining service life.

Traditionally, the assessment of existing structures has relied on a combination of visual inspection, non-destructive testing at selected locations and analytical or numerical modelling. While these methods are indispensable, they also have inherent limitations. Visual inspections provide only snapshot information and may miss hidden or inaccessible damage. Local tests, such as core drilling or point-wise strain and displacement measurements, offer detailed information at a few locations but do not necessarily capture the global structural response. In addition, the behaviour of existing structures can be influenced by uncertainties in material properties, construction details and boundary conditions, which are difficult to fully account for in conventional assessment models.

Structural Health Monitoring (SHM) has emerged as a modern engineering approach to address this need. It is a process aimed at providing accurate and timely information on structural condition and performance [1]. This involves the continuous or periodic collection and analysis of structural response data, such as strain, displacement, vibration, or temperature, to evaluate the integrity and serviceability of a structure throughout its life cycle. The information obtained from the monitoring is generally used to plan and design maintenance activities, increase safety, verify hypotheses, reduce uncertainty, and expand knowledge of the structure being monitored [1]. For existing concrete structures in particular, such information is crucial for detecting and tracking cracking, monitoring serviceability limits and supporting decisions on maintenance, strengthening or replacement.

In practice, the implementation of SHM on existing structures is often constrained by limited access, complex geometry and the need to minimise disruption to users. This places high demands on the sensing systems employed: they should be robust, minimally invasive and capable of capturing the relevant structural response with sufficient spatial and temporal resolution. Against this backdrop, Distributed Fibre Optic Sensing (DFOS) has gained attention as a promising technology for monitoring strain and crack development in existing concrete structures. The present thesis investigates how DFOS can be utilised effectively for this purpose, with a specific focus on strain and crack-width monitoring.

1.2. Potential of Distributed Fibre Optic Sensing (DFOS)

Conventional sensing systems used in Structural Health Monitoring, such as electrical strain gauges, vibrating wire gauges and displacement transducers, typically provide measurements at a limited number of discrete locations [2]. While these instruments can offer high accuracy locally, they may fail to capture the spatial variation of strain and cracking along a structural element, especially in large or complex concrete members. For existing structures where access is often restricted and critical regions may not be known a priori, such point-wise measurements can be insufficient to characterise the global structural response or to reliably detect localised damage.

Distributed Fibre Optic Sensing (DFOS) has emerged as a promising solution to address these challenges. Unlike conventional sensors that measure at isolated points, DFOS provides a continuous strain profile along the entire length of an optical fibre [2], [3], [4]. This enables simultaneous monitoring of both global and local responses, including load-induced strain, crack initiation, and temperature effects. The technique operates based on the scattering of light within the optical fibre-typically Rayleigh, Brillouin, or Raman scattering, allowing for spatial resolutions in the order of millimetres and measurement lengths extending from several meters to kilometres [4], [5]. This combination of high spatial resolution and long measurement range makes DFOS particularly attractive for monitoring extended concrete members and bridge components.

In the context of existing concrete structures, DFOS[1] can be installed in several ways, including embedded inside concrete matrix or along reinforcement, placed in grooves cut into the concrete surface, or surface-bonded using an adhesive layer [2], [6]. Surface-bonded DFOS is often preferred for retrofitting existing structures because it avoids intrusive interventions and can be applied locally in critical regions identified from inspections or structural analyses. When properly installed, a surface-bonded fibre can capture detailed strain profiles along the concrete surface, allowing engineers to identify locations of cracking, monitor the evolution of crack patterns and quantify flexural and shear deformations.

A key advantage of DFOS for damage detection in concrete is its ability to resolve sharp strain concentrations associated with crack formation. Localised peaks in the measured strain profile can be linked to discrete cracks, and under suitable assumptions, these strain peaks can be integrated to estimate corresponding crack widths. At the same time, the distributed nature of the measurement enables simultaneous assessment of the global deformation pattern along the monitored member. In principle, DFOS therefore provides both the local information needed for crack-width evaluation and the global information needed for assessing overall structural behaviour.

However, the effective use of surface-bonded DFOS for strain and crack-width monitoring in existing concrete structures is not straightforward. The measured strain in the fibre does not necessarily coincide with the true strain at the concrete surface, because of strain-transfer effects through the adhesive and fibre coatings. In addition, the quality of the installation, the choice of adhesive, the bondline thickness and the presence of pre-existing cracks can strongly influence the measured strain profile and the reliability of crack-width estimates. As a result, there is a need to better understand how DFOS should be installed on concrete, how the measured strain relates to the actual concrete strain, and under which conditions DFOS-based crack widths can be considered reliable.

These challenges form the basis of the present thesis. The work focuses on experimentally investigating surface-bonded DFOS for strain and crack-width monitoring in reinforced concrete members, with the aim of developing a practical installation strategy, quantifying strain-transfer effects and assessing the reliability of DFOS-derived crack widths in the context of existing concrete structures.

1.3. Problem Definition and Research Gap

The discussion above highlights that Structural Health Monitoring can play a key role in assessing and managing existing concrete structures, and that Distributed Fibre Optic Sensing (DFOS) offers attractive capabilities for this purpose. In particular, surface-bonded DFOS on concrete surfaces has the potential to provide high-resolution strain profiles from which both global deformation patterns and local crack formation can be inferred. However, translating this potential into a reliable monitoring tool for existing structures is not straightforward. Several practical and conceptual issues remain insufficiently

[1] DFOS has been used as an acronym for both Distributed Fibre Optic Sensing and Distributed Fibre Optic Sensors.

resolved, which motivates the present research.

A first issue concerns the *installation strategy* for surface-bonded DFOS on concrete. In practice, installation is often based on manufacturer guidelines or experience from previous projects. These guidelines typically specify general recommendations regarding adhesive selection, curing and fibre handling, but do not provide an experimentally validated strategy tailored to concrete substrates. At present, there is no clear, evidence-based procedure that links installation parameters such as surface preparation, adhesive type, bondline thickness, fibre pretension and routing to the quality of strain transfer and the robustness of the measurements. This motivates the need to identify which installation parameters are critical and how they should be combined into a practical strategy for surface-bonded DFOS on concrete.

A second issue relates to the *relationship between DFOS-measured strain and the true concrete surface strain*. The strain recorded by a surface-bonded fibre is transmitted through the adhesive layer and fibre coatings, and may be influenced by imperfect bonding, local debonding or microcracking. Analytical strain-transfer models exist for idealised configurations of point sensors like Fibre Bragg Grating (FBG), but their applicability to Distributed Fibre Optic Sensors (DFOS) on real installations on reinforced concrete members is not always clear. In many applications, it is implicitly assumed that DFOS strain is equivalent to the concrete surface strain, without explicit quantification of the strain-transfer efficiency. For the purpose of structural assessment and crack-width estimation, this assumption can introduce systematic errors. There is therefore a need to experimentally quantify strain-transfer effects for representative surface-bonded DFOS installations on concrete and to derive a calibrated relationship that allows DFOS-measured strains to be converted into estimates of the concrete surface strains. In addition, there has been limited research on the use of DFOS for measuring compressive strains in concrete. DFOS has demonstrated excellent performance in capturing tensile behaviour, particularly in detecting pre-cracking strain and post-cracking crack widths. Its response under compression, however, is less understood. Understanding strain transfer and measurement accuracy in compression zones is equally important.

A third issue concerns the *reliability of DFOS-derived crack widths*. Methods have been proposed to estimate crack widths by integrating localised strain peaks in DFOS profiles, and promising results have been reported in laboratory studies. However, the accuracy and robustness of these methods under realistic conditions are not yet fully established. In existing structures, DFOS installations may be affected by noise, missing data segments, limited spatial resolution or pre-existing cracks that are not perfectly captured by the fibre. The influence of such effects on the accuracy of crack-width estimates has not been systematically quantified. As a result, it is unclear under which conditions crack widths derived from DFOS can be considered reliable for structural assessment and how sensitive they are to data quality issues.

In summary, while DFOS has significant potential for strain and crack-width monitoring in existing concrete structures, three interrelated gaps hinder its effective use in practice:

- the lack of an experimentally supported installation strategy for surface-bonded DFOS on concrete;
- the limited quantification of strain-transfer effects between the concrete surface and the fibre;
- the incomplete validation of the reliability of DFOS-derived crack widths under realistic data conditions.

These gaps motivate the main research question and the three sub-questions formulated in Section 1.4, and they form the basis for the experimental and analytical work presented in this thesis.

1.4. Research Questions

The previous section highlighted three key challenges for the effective use of Distributed Fibre Optic Sensing (DFOS) in existing concrete structures: the lack of an experimentally supported installation strategy for surface-bonded fibres, the limited quantification of strain-transfer effects between concrete and fibre, and the incomplete validation of DFOS-derived crack widths under realistic data conditions. To address these challenges, this thesis focuses on the experimental investigation of surface-bonded

DFOS applied to reinforced concrete members, combined with insights from the literature to develop practical guidelines for strain and crack-width monitoring in existing concrete structures.

Against this background, the main research question guiding this thesis is formulated as:

> ***How can Distributed Fibre Optic Sensing (DFOS) be effectively utilized for strain and crack-width monitoring in existing concrete structures?***

To address the main research question, the following sub-questions are formulated:

1. What installation strategy for surface-bonded Distributed Fibre Optic Sensors on concrete ensures reliable bonding and effective strain transfer?
2. How can strain-transfer effects be quantified so that DFOS-measured strains can be converted into accurate estimates of the concrete surface strains?
3. How reliable are crack widths obtained from Distributed Fibre Optic Sensing for reinforced concrete members?

1.5. Research Approach

The research approach adopted in this thesis is designed to systematically address the main research question and the three sub-questions introduced in Section 1.4. The overall methodology follows a logical progression from a literature-based identification of knowledge gaps, via an experimental programme on reinforced-concrete members, to quantitative assessment and discussion of the implications for existing concrete structures. An overview of this methodology is shown schematically in Figure 1.1.

The starting point is a critical review of the state of the art (Chapter 2). The literature on structural health monitoring of concrete structures and on Distributed Fibre Optic Sensing (DFOS) is examined to understand current DFOS capabilities, installation practices, strain-transfer models and existing crack-width estimation procedures. This review reveals three key gaps: the absence of an experimentally validated installation strategy for surface-bonded DFOS on concrete, the limited quantification of strain-transfer effects between concrete and the fibre, and the incomplete validation of DFOS-derived crack widths under realistic data conditions. These gaps motivate Sub-question 1 on installation strategy, Sub-question 2 on strain-transfer effects and Sub-question 3 on the reliability of DFOS-based crack widths.

To address these gaps, an experimental programme is designed comprising two complementary test setups on reinforced-concrete members (Chapter 3). First, a three-point bending test on a large-scale inverted T-girder is conducted as a qualitative investigation. DFOS is applied along the girder and the resulting distributed strain measurements are used to observe crack initiation and propagation under shear-dominated loading, in parallel with Digital Image Correlation (DIC). This test serves a dual role: it provides a learning phase for practical installation questions, such as adhesive selection, surface preparation, routing and anchorage, and it offers qualitative insight into the ability of DFOS to detect and localise cracks. Second, a series of four-point bending tests on reinforced-concrete beams is carried out to enable quantitative evaluation. These beams are instrumented with DFOS, electrical strain gauges and DIC, and are loaded in flexure under controlled conditions.

The analysis of the experimental data proceeds in two main branches. In the first branch, the focus is on installation strategy and strain-transfer behaviour (primarily Chapter 3). The qualitative T-girder test is used to identify installation-related issues and to refine a practical installation strategy for surface-bonded DFOS on concrete, contributing to Sub-question 1. The four-point bending tests are then used to quantify strain transfer by comparing DFOS strains with strain-gauge measurements in both tension and compression zones. From these comparisons, a strain-transfer efficiency is derived and a calibrated factor is proposed to convert DFOS-measured strains into estimates of the concrete surface strains, thereby addressing Sub-question 2.

In the second branch, the focus is on the ability of DFOS to provide reliable crack-width information (Chapter 4). The T-girder test is first used to investigate qualitatively how well DFOS can detect and locate cracks along a member, by comparing DFOS strain peaks and crack patterns with DIC. Next, the four-point bending tests are used for a quantitative assessment of crack-width estimation. Crack widths

are derived from DFOS strain profiles and validated against DIC-based crack widths for different load stages and specimens, providing a measure of accuracy. The influence of missing or degraded DFOS data is investigated by introducing the effective gap ratio L_e/L, which allows practical ranges of data quality to be identified within which crack widths derived from DFOS can be considered trustworthy. In this way, Sub-question 3 is addressed using both qualitative and quantitative evidence.

Finally, the findings from both analysis branches are synthesised and interpreted in the context of existing concrete structures (Chapter 5). The refined installation strategy, the calibrated strain-transfer factor and the crack-width reliability limits are combined into practical guidelines for DFOS-based strain and crack-width monitoring. An illustrative example based on an existing prestressed concrete bridge is used to demonstrate how these guidelines can inform DFOS sensor layouts and data interpretation at structure level. Chapter 6 then summarises the main findings, provides explicit answers to the main research question and the three sub-questions, and formulates recommendations for practice and future research.

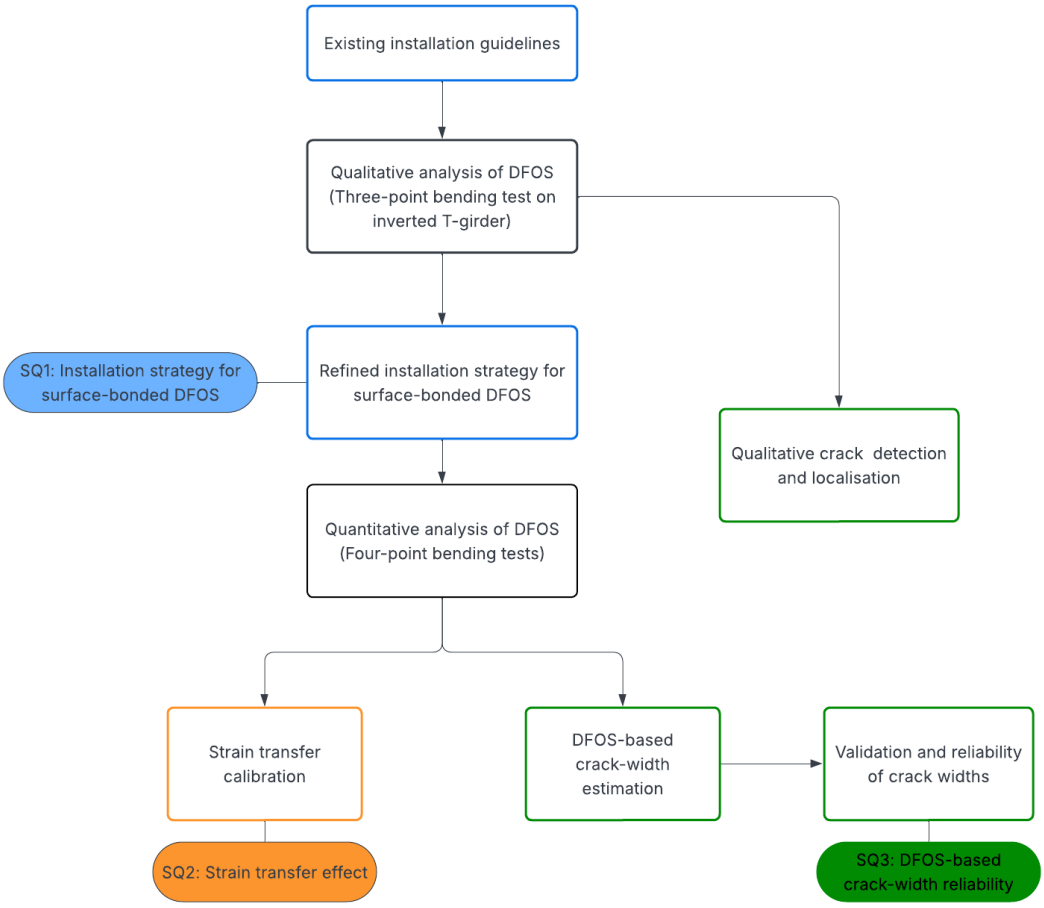

Figure 1.1: Research Methodology

1.6. Research Scope and Limitations

This thesis focuses on the use of surface-bonded Distributed Fibre Optic Sensing (DFOS) for strain and crack-width monitoring in reinforced concrete members, with the aim of informing monitoring strategies for existing concrete structures. The main scope and limitations are summarised below.

Scope

- Laboratory tests on reinforced concrete members: one large inverted T-girder in three-point bend-

ing (shear-dominated) and a series of beams in four-point bending (flexure-dominated).

- DFOS applied *on the concrete surface* using an adhesive bondline; embedded fibres and reinforcement-mounted fibres are not considered.
- A single Rayleigh-based DFOS system is used, with fixed gauge length and spatial sampling.
- Analysis focuses on mechanical strain and crack-width estimation under short-term monotonic loading.

Limitations

- The findings are specific to the tested specimen types, concrete mix, fibre type and adhesive; extrapolation to other configurations should be done with care.
- Only bending- and shear-dominated behaviour under quasi-static loading is studied; long-term effects (creep, shrinkage, environmental degradation, fatigue) are not addressed.
- Temperature effects and combined thermo-mechanical loading are not explicitly investigated.
- No full-scale DFOS monitoring campaign is performed on a real structure and no new finite element model of a particular bridge is developed; the bridge example in this thesis is conceptual.

1.7. Thesis Structure

This thesis is organized into seven chapters that together address the research aim and sub-questions introduced earlier. Each chapter has a distinct objective and contributes to building a comprehensive understanding of how Distributed Fibre Optic Sensors (DFOS) can be effectively applied for the structural health monitoring of concrete structures.

Chapter 1: Introduction presents the background and motivation for monitoring existing concrete structures, with a focus on the potential of Distributed Fibre Optic Sensing (DFOS) for strain and crack-width monitoring. It formulates the problem definition, identifies the research gaps, and states the main research question and three sub-questions. The chapter concludes with the research approach, scope and limitations, and an overview of the thesis structure.

Chapter 2: Literature Review places DFOS in the context of structural health monitoring of concrete structures. It reviews DFOS technology, strain-transfer mechanisms for surface-bonded fibres, existing analytical models for strain transfer, and methods for DFOS-based crack-width estimation. Applications of DFOS in laboratory tests and on real concrete structures are also discussed. This review provides the theoretical basis and identifies the knowledge gaps that motivate Sub-question 1 (installation strategy), Sub-question 2 (strain-transfer effects) and Sub-question 3 (crack-width reliability).

Chapter 3: Experimental Investigation of DFOS strain response first introduces a qualitative three-point bending test on a large-scale inverted T-girder. DFOS measurements are used to observe crack initiation and propagation and are qualitatively compared with Digital Image Correlation (DIC), providing insight into the strain response of surface-bonded DFOS under complex crack patterns and revealing practical installation issues. Subsequently, a series of four-point bending tests on reinforced concrete beams is presented, including specimen details, reinforcement layout, loading configuration, DFOS installation procedures and reference measurements. Using these tests, DFOS strains are compared with strain-gauge measurements in both tension and compression to quantify strain-transfer efficiency. The chapter proposes practical recommendations for an installation strategy for surface-bonded DFOS on concrete and introduces a calibrated strain-transfer factor to convert DFOS-measured strains into estimates of the concrete surface strains.

Chapter 4: Assessment of DFOS-derived crack-widths addresses Sub-question 3. Building on the four-point bending tests introduced in Chapter 3, this chapter evaluates how reliably crack widths can be obtained from DFOS measurements. Crack widths are derived from DFOS strain profiles and compared with crack widths obtained from DIC for different load stages and specimens, providing a quantitative measure of accuracy. The influence of missing or degraded DFOS data is investigated using the effective gap ratio, allowing practical ranges to be defined within which DFOS-based crack widths can be considered reliable for structural assessment.

Chapter 5: Discussion synthesises the results of Chapters 3 and 4 and discusses their implications for DFOS-based monitoring of existing concrete structures. It brings together the installation strategy, the calibrated strain-transfer factor and the crack-width reliability limits to formulate practical guidelines for DFOS installation, strain interpretation and crack-width monitoring in practice. An illustrative example based on an existing prestressed concrete bridge is used to demonstrate how the laboratory insights can inform DFOS sensor layouts and data interpretation at structure level.

Chapter 6: Conclusions and Recommendations summarises the main findings of the thesis and provides explicit answers to the three sub-questions and the main research question. The chapter also offers recommendations for the practical implementation of DFOS in the monitoring of existing concrete structures and identifies directions for future research.

2

Literature Review

This section provides an introduction to Structural Health Monitoring (SHM) in existing concrete structures in Section 2.1. Section 2.2 provides information on Distributed Fibre Optic Sensors and their working principle, the installation strategies used for DFOS in the past. The strain transfer theories developed in the past have been briefly discussed in this section. Information on analysing crack widths through DFOS is discussed in Section 2.3. And Lastly, the prior application of DFOS in laboratory and field applications is discussed in Section 2.4.

2.1. Structural health monitoring of existing concrete structures

2.1.1. Concept and framework of SHM

Structural Health Monitoring (SHM) has been defined in various ways across the literature, depending on the field of application and the scale of observation. Wenzel described SHM as the implementation of a damage identification strategy to the civil engineering infrastructure [7]. Damage is defined as changes in the material and / or geometric properties of these systems, including changes in the boundary conditions and the connectivity of the system [7]. Similiarly, Glišić and Inaudi have defined SHM as the process aimed at providing accurate and in-time information concerning structural condition and performance. It consists of permanent continuous, period or periodically continuous recording of representative parameters, over short or long terms. These damages can affect the current or future performance of these structures and hence need to be monitored during the service life.

The structural monitoring process can be broadly divided into several core activities: selection of monitoring strategy, installation of monitoring system, maintenance of monitoring system, data management and closing activities in the case of interruption of monitoring [1]. Each of these main activities comprises a set of sub-tasks, as outlined by Glišić and Inaudi [1] and shown in Table 2.1. Among them, developing an effective monitoring strategy is considered the most critical, as it directly influences all subsequent activities and determines the overall success of the monitoring programme.

The monitoring strategy itself involves several essential steps:

1. Establishing the monitoring aim
2. Identifying and selecting representative parameters to be monitored
3. Selecting an appropriate monitoring system
4. Designing the sensor network
5. Establishing the monitoring schedule
6. Planning data exploitation
7. Costing the monitoring

Table 2.1: Breakdown structure of the core monitoring activities [1].

Monitoring strategy	**Installation of monitoring system**	**Maintenance of monitoring system**	**Data management**	**Closing activities**
• Monitoring aim	• Installation of sensors	• Providing for electrical supply	• Execution of measurements (reading of sensors)	• Interruption of monitoring
• Selection of monitored parameters	• Installation of accessories (connection boxes, extension cables, etc.)	• Providing for communication lines (wired or wireless)	• Storage of data (local or remote)	• Dismantling of the monitoring system
• Selection of monitoring systems	• Installation of reading units	• Implementation of maintenance plans for different devices	• Providing for access to data	• Storage of monitoring components
• Design of sensor network	• Installation of software	• Repairs and replacements	• Visualization	
• Schedule of monitoring	• Interfacing with users		• Export of data	
• Data exploitation plan			• Interpretation	
• Costs			• Data analysis	
			• The use of data	

2.1.2. Importance of strain monitoring

Strain is a key indicator for supervising the structural condition from a global perspective. Although stresses cannot be measured directly, they are linked to strain through Hooke's law (Equation 2.1, so any change in the stress field is reflected by a change in the strain field. On top of that, several quantities relevant for structural assessment, such as rotations, inclinations and differential settlements, can be derived from static and dynamic measurements of strain and displacement. Expected strain levels are usually evaluated during design and are associated with safety factors that vary between different structural types [8]. For reinforced concrete and steel structures, typical working strains are on the order of several hundred microstrain, and may increase when cracking occurs. Sensors therefore need to detect strain changes that are at least one to two orders of magnitude smaller than these working levels, implying a required accuracy on the order of a few microstrains. The local gauge length should generally be a few times larger than the aggregate size, which for concrete leads to measurement bases of roughly 2–5 cm. The appropriate measurement range, spatial resolution and separation of temperature and mechanical strain depend on the application, but in all cases the sensing system must provide added value to the user while remaining economically justifiable [9].

For linear-elastic behaviour, stress and strain are related by Hooke's law,

$$\sigma = E\,\varepsilon, \tag{2.1}$$

where σ is the normal stress, E is the Young's modulus of the material, and ε is the normal strain. So any change in the stress field is reflected by a corresponding change in the strain field.

In parallel to global response, monitoring local damage is equally important. Local phenomena such as cracking, fatigue, slip, debonding and loss of effective cross-sectional area all manifest themselves through changes in the strain field. Strain can therefore be used to describe deformations, study crack opening and even detect slip or debonding at interfaces [8]. For crack monitoring, the localisation of strain associated with crack formation should enable the early detection and accurate positioning of multiple closely spaced microcracks, typically separated by only a few centimetres. To assess crack openings, the measurement system must be capable of resolving crack-width changes on the order

of a few tenths of a millimetre. Moreover, for long-life infrastructure such as bridges, the sensing system is ideally required to remain functional over decades, approaching the design life of the structure [7]. Meeting these demands has traditionally led structural engineers to rely on high-quality strain and displacement sensors, often combined with surface inspections, for the evaluation of structural performance.

2.1.3. Importance of crack monitoring in concrete structures

Concrete is one of the most widely used construction materials worldwide due to its relatively low cost, robustness, versatility in shaping and its compatibility with steel reinforcement. It is employed in a broad range of structures, including buildings, bridges, tunnels and dams [10]. However, a well-known disadvantage of concrete is its limited tensile strength, which makes cracking almost inevitable during the service life of a structure. Cracks may develop due to a variety of causes, such as inadequate construction quality, temperature and shrinkage effects, external loading, differential settlements or chemical reactions [11]. Once cracks form, they can compromise the protective function of the concrete cover, promote reinforcement corrosion, reduce the load-carrying capacity and, in extreme cases, contribute to partial or global structural failure. For these reasons, crack monitoring has become a key component of structural health monitoring for concrete infrastructure [12].

From a practical point of view, crack monitoring in concrete is challenging. Cracks can initiate at many possible locations and their formation is influenced by complex combinations of mechanical and environmental actions, so predicting where they will appear in advance is difficult. In the early stages, crack widths are often very small, in the sub-millimetre or even micrometre range, which makes them hard to detect reliably by visual inspection alone. Internal cracks that have not yet propagated to the surface are even more difficult, and in many cases impossible, to identify by conventional visual methods.

Because cracks are closely related to tensile strain, traditional crack monitoring approaches often rely on strain measurements at discrete points using sensors such as foil strain gauges, linear variable differential transformers (LVDTs) or Fibre Bragg Gratings (FBGs) [6]. While these devices can measure strain with high accuracy, they only provide information at the locations where they are installed. To monitor large concrete structures comprehensively, a very large number of point sensors would be required, which is often impractical due to cost, installation effort and data handling. Other advanced methods, such as ultrasonic techniques [13] to estimate crack depth, can be effective locally but are not easily scalable for integral monitoring of long linear infrastructure.

Under tensile stress, cracks in concrete typically propagate orthogonally to the principal tensile direction. Material degradation begins with the diffusion of micro-cracks within the cement paste matrix, as illustrated in Figure 2.1. Once the tensile strength of the concrete is exceeded, a softening phase initiates, during which multiple micro-cracks merge to form a macro-crack. This macro-crack signifies a localised discontinuity in the material [8].

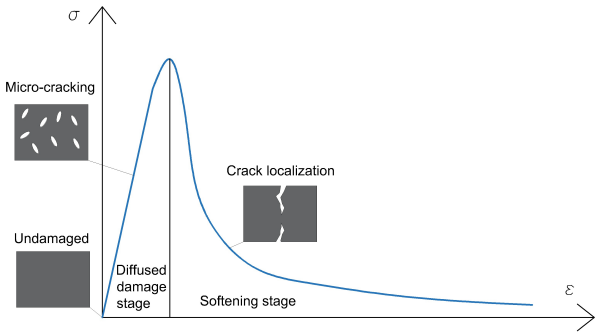

Figure 2.1: Behavior of concrete material under tension loading and its damage evolution [8]

Overall, conventional crack monitoring methods based on local sensors or manual visual inspection tend to be labour-intensive, time-consuming and prone to human error, and they struggle to provide dense, continuous information over large structural elements. This motivates the exploration of alternative sensing technologies that can offer high spatial resolution and automation while remaining

economically feasible. In this context, distributed sensing is particularly attractive, because crack formation and opening lead to localised strain concentrations along the fibre, which can be used to detect, locate and, under appropriate assumptions, estimate crack widths [12]. This potential is one of the main motivations for the present thesis to investigate DFOS-based crack monitoring in reinforced concrete members.

2.2. Distributed Fibre Optic Sensors (DFOS)

A structural health monitoring (SHM) system typically consists of sensors designed to record parameters that reflect the condition and behaviour of a structure. Conventional mechanical and electrical transducer-based sensors have long been used for such measurements. However, fibre optic sensors have emerged as a promising alternative due to their high accuracy, immunity to electromagnetic interference, compact size, and ability to integrate directly within structural components [1]. Although their adoption in civil engineering was initially limited, their advantages, such as reduced maintenance needs, automated data acquisition, and long-term stability, make them particularly suitable for large-scale infrastructure monitoring applications. The main categories of fibre optic sensing technologies are illustrated in Figure 2.2.

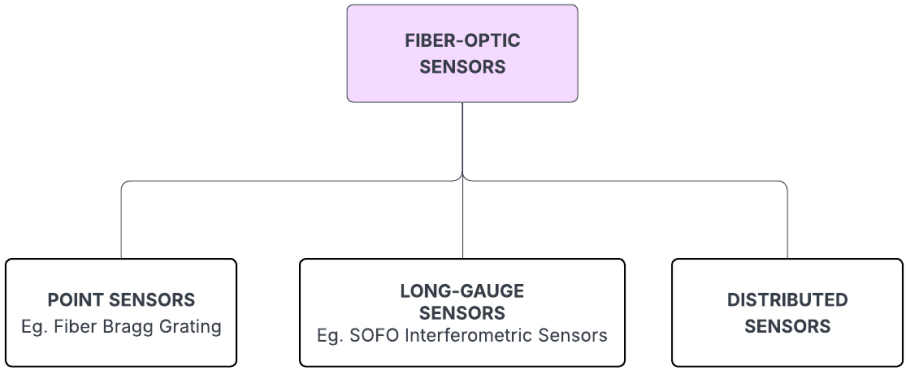

Figure 2.2: Classification of fibre-optic sensing technologies [1].

Among the most widely used point or quasi-distributed systems are Fibre Bragg Grating (FBG) sensors and SOFO interferometric sensors. FBG sensors measure strain or temperature at discrete locations along an optical fibre by detecting wavelength shifts reflected from periodic gratings inscribed in the fibre core (Figure 2.3). Through multiplexing, multiple gratings can be placed along a single fibre to obtain measurements at predefined points [14]. However, this setup requires the measurement points to be known in advance, which can be a limitation for concrete structures where cracks develop unpredictably. The SOFO system (*Surveillance d'Ouvrages par Fibres Optiques*) represents a long-gauge interferometric sensor capable of measuring average deformations over extended gauge lengths (typically several tens of centimetres) with micrometre-level precision [15]. It consists of a pair of single-mode fibres, one reference and one measurement fibre, installed within a protective tube and anchored to the structure at both ends (Figure 2.4). Although FBG and SOFO systems have provided valuable insights in research and field applications, they still measure at discrete or predefined locations, leaving portions of the structure unmonitored.

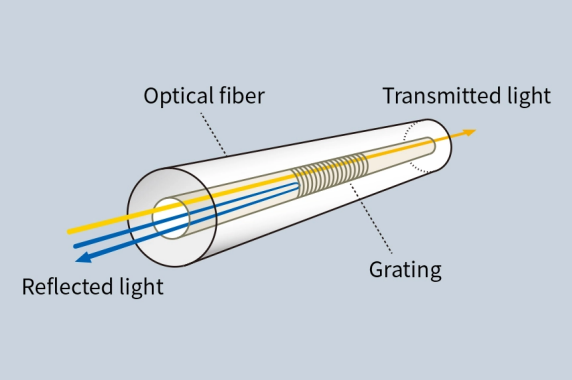

Figure 2.3: Functional principle of FBG sensors [16].

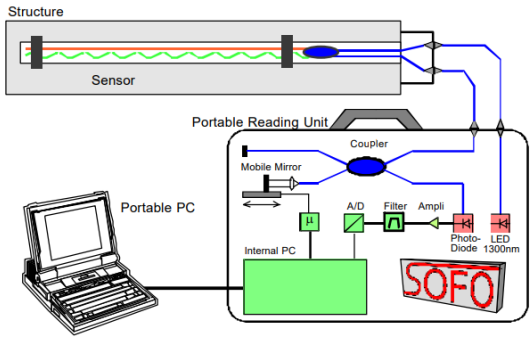

Figure 2.4: Setup of the SOFO interferometric sensor system [15].

To overcome this limitation, Distributed Fibre Optic Sensing (DFOS) technologies have been developed, capable of providing truly continuous strain or temperature measurements along the entire fibre length. These systems detect variations in backscattered light caused by local changes in strain or temperature within the optical fibre, enabling a spatially resolved measurement profile [17]. Depending on the physical scattering mechanism used (Raman, Brillouin, or Rayleigh), different DFOS methods offer distinct measurement ranges, accuracies, and spatial resolutions. Figure 2.5 illustrates the broad applicability of DFOS in monitoring.

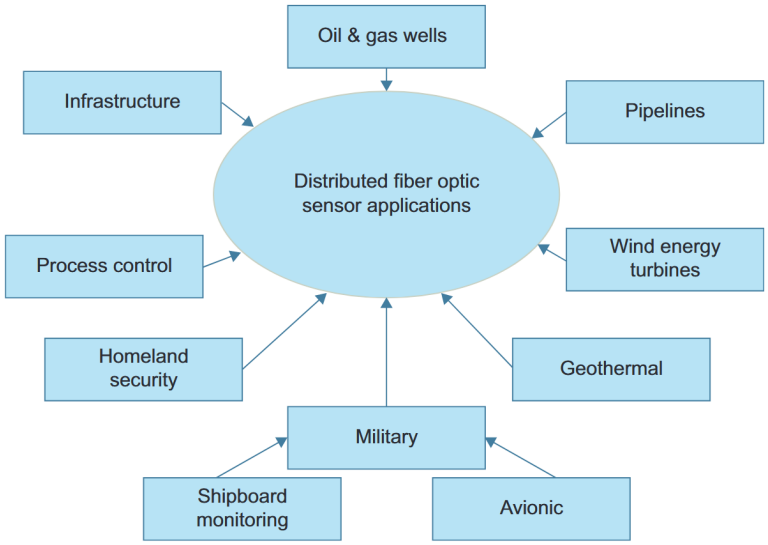

Figure 2.5: Applications of DFOS [18].

2.2.1. Distributed Fibre Optic Sensing technology

Distributed Fibre Optic Sensing (DFOS) systems are based on the interrogation of standard optical fibres using scattering phenomena such as Rayleigh, Brillouin or Raman scattering. In contrast to point fibre-optic sensors, which provide measurements at discrete locations, DFOS instruments analyse the backscattered signal along the fibre and return a spatially resolved profile of strain or temperature along its length. The achievable spatial resolution and measurement range depend on the interrogation principle and hardware configuration, but typically range from millimetres to metres in resolution and from tens of metres to several kilometres in length. The capability has often been compared to a human nervous system: the optical fibre acts as a distributed network of sensing “nerves”, while the interrogator functions as the “brain”, processing and interpreting the incoming optical signals [4]. Such distributed systems facilitate the realisation of intelligent structures that can autonomously monitor strain distribution, crack initiation and propagation, deflection, temperature variations, and vibration response under

both static and dynamic conditions.

Advantages of DFOS

Compared with conventional point sensors and quasi-distributed optical sensors, DFOS offers several advantages [2] that are particularly relevant for monitoring concrete structures:

- **Continuous spatial coverage:** DFOS provides a quasi-continuous strain profile along the fibre, enabling simultaneous observation of global deformation patterns and localised strain concentrations associated with cracking, rather than only at a few discrete sensor locations.
- **High spatial resolution over long distances:** Depending on the technology, millimetre- to centimetre-scale spatial resolution can be achieved over tens to hundreds of metres of fibre, which is well suited for monitoring extended beams, girders or decks.
- **Multiplexing and reduced cabling:** A single optical fibre can replace a large number of conventional strain gauges, reducing the amount of cabling, connectors and data acquisition channels required for dense monitoring layouts.
- **Small size and installation flexibility:** The fibre diameter is of the order of a few hundred micrometres, allowing DFOS to be embedded in concrete, bonded to reinforcement, or surface-bonded to existing members with minimal intrusion.
- **Immunity to electromagnetic interference and corrosion:** Optical fibres are dielectric and non-corrosive, which is advantageous in reinforced concrete structures and harsh environments where electrical sensors may be affected by electromagnetic fields or corrosion.
- **Potential for combined strain and crack monitoring:** Localised peaks in the distributed strain profile can be used to detect and locate cracks and, under suitable assumptions, to estimate crack widths, thereby linking serviceability and durability assessment in a single measurement system.

These characteristics make DFOS a promising technology for structural health monitoring of existing concrete structures, particularly when dense spatial information on strain and cracking is required and access for installing conventional sensors is limited.

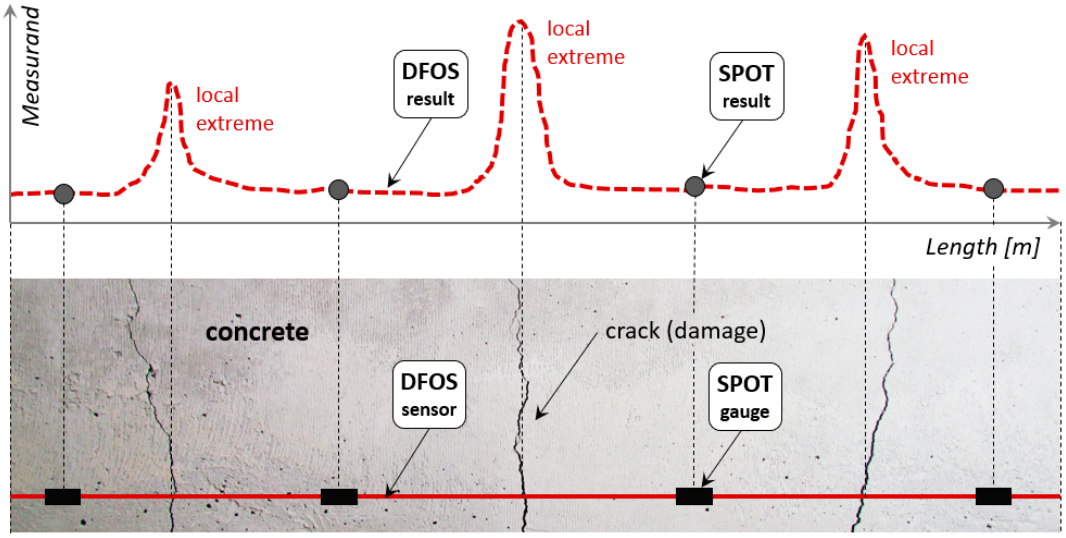

Figure 2.6: Graphical comparison between capabilities of DFOS and spot gauges [4].

2.2.2. Principle of DFOS

As discussed above, Distributed fibre Optic Sensing (DFOS) relies on the analysis of light backscattering along the optical fibre's length. Scattering is at the origin of DFOS and is defined by the interaction between light and the optical medium [19]. The primary scattering mechanisms utilized in DFOS are

Rayleigh scattering (liner) and (non-linear) Brillouin and Raman scattering, each offering different sensitivities and applications depending on the measurement requirements (Figure 2.7).

i) **Rayleigh scattering**

Rayleigh scattering is widely used in distributed fibre optic sensing systems to measure both mechanical and thermal strains with extremely high spatial resolution. This technique enables detection at the millimetre scale, allowing for over 1,000 measurement points per meter of fibre [4], which is especially valuable for identifying and localizing cracks or other small-scale structural discontinuities. Systems based on Optical Frequency Domain Reflectometry (OFDR) achieve this resolution through swept wavelength interferometry, capturing shifts in the Rayleigh backscatter spectrum that serve as a unique fingerprint for each fibre. These spectral shifts, caused by strain or temperature changes, enable detailed distributed sensing along the fibre. Despite its exceptional spatial resolution and capability for dynamic measurements at frequencies up to 250 Hz, the primary limitation of Rayleigh-based systems is the relatively short measurement range, which typically does not exceed 50 to 70 meters [17][5][2][20].

ii) **Brillouin scattering**

Brillouin scattering-based distributed fibre optic sensing systems are widely utilized in SHM, particularly in civil engineering applications that require large-scale coverage [17]. These systems can measure both mechanical and thermal strains along optical fibres over extended distances, typically up to 25 kilometers or more. This makes them well-suited for monitoring long linear infrastructure such as tunnels, pipelines, dams, embankments, and landslide-prone areas [4][5]. Although their spatial resolution is relatively low, generally between 20 centimeters and 1 meter, advancements such as Brillouin Optical Time Domain Analysis (BOTDA) have led to notable improvements. However, the resolution still remains insufficient for detecting localized damage, such as discrete cracks in concrete, as these tend to appear as smeared signals over the measurement length. Despite this limitation, the ability to perform measurements over long distances offers significant advantages for global monitoring in applications where high spatial resolution is not essential [19][21].

iii) **Raman scattering**

Raman scattering is primarily used for distributed temperature sensing (DTS) along optical fibres and is capable of monitoring temperature profiles over long distances [17], often exceeding 25 kilometres. The typical spatial resolution begins at approximately 50 centimetres [4][5]. Due to its strong sensitivity to temperature variations, Raman-based sensing is commonly applied either as an independent diagnostic tool or as a complementary system to compensate for temperature effects in Rayleigh and Brillouin-based strain measurements. In civil engineering, its application has been somewhat limited, with notable use in detecting water leakage in structures such as dams and dikes. Beyond infrastructure monitoring, Raman sensing has found broader use in fields such as art conservation and forensic science, where precise temperature-based diagnostics are valuable [22].

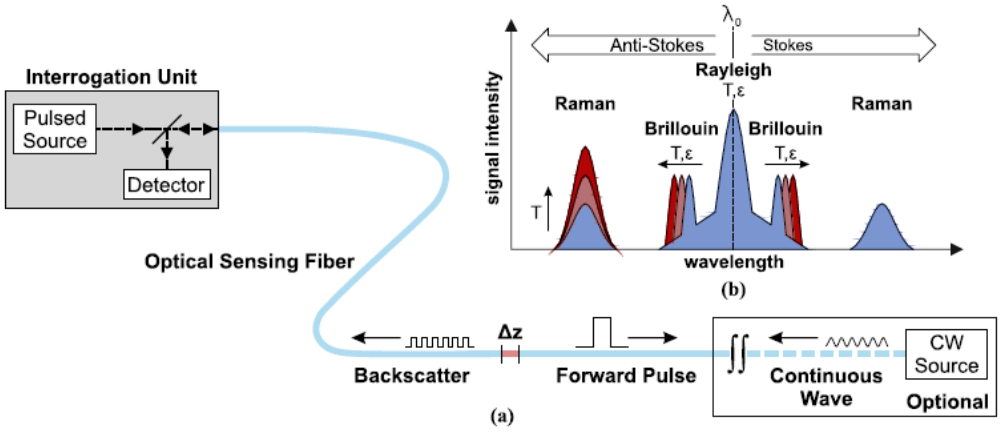

Figure 2.7: Distributed fibre optic sensing techniques: a) basic scheme of sensing setup and b) different scattering components in optical glass fibres [23].

2.2.3. Installation of DFOS on concrete structures

The accuracy and reliability of strain measurements obtained through Distributed Fibre Optic Sensors (DFOS) strongly depend on the chosen installation strategy [12]. Over the years, various installation configurations have been developed for DFOS in concrete, including embedded, near-to-surface, and surface-bonded systems [2]. Each configuration presents distinct advantages and limitations in terms of strain transfer efficiency, fibre protection, and practical feasibility.

The specific method used for integrating optical fibre within concrete highly influences its strain transfer and crack sensing performance [12]. In practice, there are three installation methods typically used:

1. Bonding the fibre to reinforcement before casting.

   In this method, the optical fibre is longitudinally attached to a reinforcing bar using a continuous layer of adhesive before the concrete is cast. The fibre may be positioned directly on the rebar surface or placed within a shallow groove along it. Once embedded, the fibre primarily records the strain response of the reinforcement, so the measured strain peaks at crack locations are smaller and more smeared compared to fibres placed directly within the concrete matrix [12].

2. Direct embedding within the concrete matrix.

   Here, the optical fibre is secured to the internal reinforcement at regular intervals before casting. The subsequent concreting process fully encapsulates and protects the fibre, ensuring excellent mechanical bonding and strain transfer. An additional advantage of this configuration is that measurements can begin from a genuine zero-strain state during construction. However, this approach can only be implemented in newly built elements, since the fibre must be installed before concrete placement and is therefore unsuitable for existing structures [24].

3. Surface or near-surface bonding.

   For existing structures, the most practical approach involves the bonding of the optical fibre directly onto the prepared surface of hardened concrete [25]. The surface must first be cleaned and smoothed to ensure proper adhesion. Although this configuration is widely used in laboratory testing and short-term monitoring, its long-term durability can be affected by environmental exposure, such as ultraviolet radiation and adhesive degradation. A variation of this method involves embedding the fibre into shallow grooves cut into the concrete surface, which are subsequently filled with epoxy or mortar. This near-surface technique improves protection and achieves strain transfer performance comparable to that of fully embedded fibres [24].

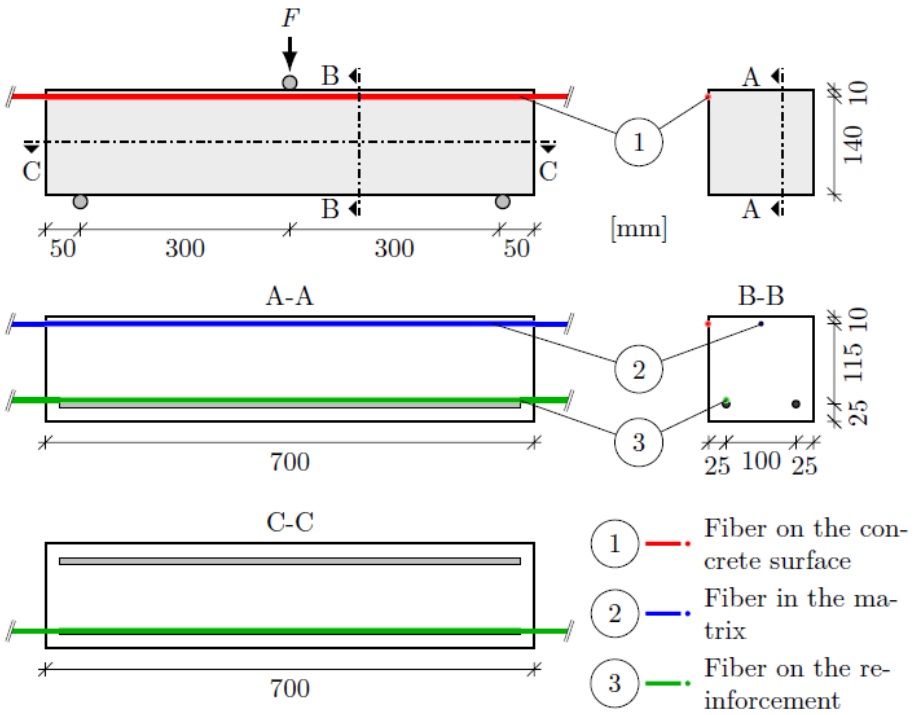

Figure 2.8: Sensor installation methods (adapted from [2])

2.2.3.1. Surface installation of DFOS

In existing concrete structures, where embedding sensors within the material is no longer feasible, the surface-bonded installation method offers a practical and non-invasive alternative for implementing DFOS [26]. For crack detection, directly bonding the optical fibre onto the concrete surface is generally considered the most effective approach, as the high strain concentrations caused by crack formation can be readily captured at the level where cracks are visible and relevant for inspection. However, when uncoated fibres are bonded using rigid adhesives, the strain in the fibre may exceed its measurement capacity after cracking, leading to a potential loss of data. This emphasises the need for proper adhesive selection and application to ensure efficient stress transfer from the concrete to the fibre core [6].

I. **Type of fibre**

   Although all Distributed Fibre Optic Sensors (DFOS) share a similar structural core consisting of a 9 µm glass core and a 125 µm glass cladding, they differ in the types of external coatings and protective layers applied 2.9. These additional layers possess distinct bonding and mechanical properties, which influence how the sensor interacts with the surrounding material and affect the accuracy of the measured strain [8][27].

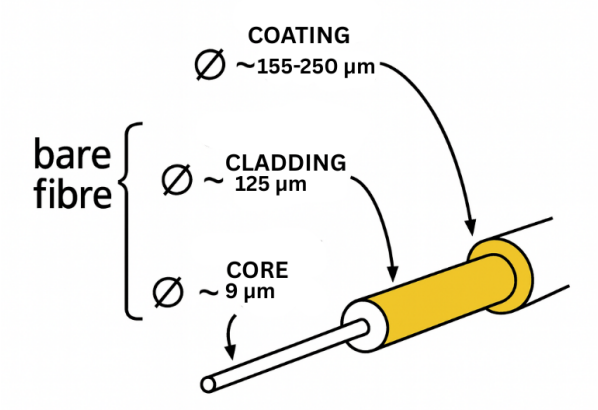

Figure 2.9: Structure of DFOS fibre (adapted from [28]).

Common coating materials include polyimide, acrylate, and nylon, while some cables are further protected by metallic or composite sheaths.

Polyimide coatings are known for providing excellent strain transfer between the glass core and the outer surface of the fibre because they chemically bond to the glass. This strong adhesion minimises slippage, particularly near the ends of the bonded region. However, this same chemical bonding makes polyimide-coated fibres more difficult to handle during splicing and stripping. Polyimide coatings are also relatively stiff and can sustain only limited strain before failure, typically up to around 1%, as specified in technical datasheets [2][29].

For this reason, polyimide-coated fibres are most suitable for applications requiring high strain measurement precision and sensitivity to local strain peaks, particularly when the expected strain levels remain within the elastic range of the material and no large cracks are anticipated. These fibres are therefore ideal for surface-bonded or directly embedded installations aimed at detecting early crack initiation and monitoring crack pattern development in concrete.

Acrylate and nylon-coated fibres offer greater flexibility and can operate effectively across a broader strain range, typically up to about 5%. These coatings make the fibres less prone to breaking at crack locations and suitable for accurately identifying crack positions. However, since strain transfer in these coatings relies purely on adhesion rather than chemical bonding, as in the case of polyimide coatings, some relative slip can occur between the glass core and the coating. This slippage can reduce measurement accuracy near sharp strain peaks or regions with large strain gradients [2].

Therefore, the selection of an appropriate DFOS type depends on the intended application. Softer coatings such as acrylate or nylon are generally preferred in situations where flexibility and mechanical durability are important, particularly when the fibres are surface-bonded or embedded in areas where cracking is expected, or when average strain behaviour, such as in shrinkage monitoring, is of greater interest than precise detection of localised strain peaks.

II. **Type of adhesive for surface-bonded DFOS**

The adhesive plays a crucial role in ensuring reliable strain transfer between the concrete surface and the fibre optic sensor. Its mechanical and chemical characteristics govern both the accuracy of strain measurements and the long-term survivability of the sensor under cracking conditions [19]. Selecting an appropriate adhesive is therefore essential for surface-bonded DFOS installations, particularly in existing structures where embedding within concrete is not possible.

An experimental investigation by Barrias et al. [19] evaluated the performance of different adhesives used for bonding polyimide-coated optical fibres onto concrete beams subjected to three-point bending tests. The beam surface was divided into segments, each bonded with a different adhesive, and tested under both uncracked and cracked conditions to assess performance across different strain regimes. The study also examined the influence of the interrogator's spatial resolution on the quality of the distributed strain data.

In the uncracked stage, all adhesives provided strain readings comparable to those obtained from conventional strain gauges. However, distinct differences emerged once cracking occurred. Adhesives with low stiffness, such as silicone, produced smoother and more uniform strain profiles but tended to spread the strain response over a wider region, thereby reducing accuracy in identifying individual cracks. In contrast, stiffer adhesives, particularly epoxy, exhibited superior strain transfer properties, producing sharper and more localized strain peaks that closely reflected the actual crack position and magnitude.

Epoxy adhesives also demonstrated excellent bonding integrity, minimal signal degradation, and reliable strain transmission even in zones with steep strain gradients [19]. These characteristics make epoxy the preferred adhesive for applications that require accurate detection of crack initiation and quantification of crack width. Its high stiffness ensures effective anchorage of the fibre to the substrate, minimizing slippage and providing a realistic representation of the concrete surface strain. Although epoxy is more brittle than flexible adhesives and demands careful surface preparation and curing control, its precision and stability make it the most suitable option for quantitative strain monitoring in surface-bonded DFOS systems.

In summary, epoxy and cyanoacrylate-based adhesives offer the best balance between strain transfer efficiency, accuracy, and durability. While softer adhesives such as silicone can be advantageous in applications involving large crack openings or requiring high flexibility, epoxy remains the most reliable choice for precise strain sensing in structural health monitoring of concrete.

It is important to note, however, that the study by Barrias et al. [19] focused exclusively on concrete regions under tensile stress conditions. The adhesive–fibre interaction and strain transfer behaviour in compression-dominated zones have not yet been thoroughly investigated. This represents a significant research gap, as understanding the performance of bonded DFOS under compressive stress states is essential for their effective use in monitoring both tension and compression regions of reinforced concrete structures.

III. **Installation practice for surface-bonded DFOS**

The installation procedure for surface-bonded Distributed Fibre Optic Sensors (DFOS) is a critical step that directly affects measurement accuracy, strain transfer efficiency, and long-term sensor performance [30][31]. In existing structures, where embedding fibres within the concrete matrix is not feasible, surface bonding represents the most practical and widely adopted approach. This technique allows the optical fibre to be directly adhered to the structural surface, enabling monitoring of strain, crack formation, and thermal effects along the member length with high spatial resolution.

Regardless of the adhesive type, the quality of bonding is a decisive factor governing strain transfer from the concrete surface to the optical fibre. Poor adhesion or excessive adhesive thickness can introduce shear deformation within the bond line, resulting in strain attenuation and signal distortion. Therefore, consistent bonding procedures and surface preparation standards must be followed to ensure efficient and durable installation [25][2][32][26].

The general procedure for installing surface-bonded DFOS, as outlined in the ODiSI Fibre Optic Sensor Installation Guide by Luna [25], consists of three main stages: surface preparation, sensor placement, and adhesive application.

(a) **Surface preparation.** The purpose of surface preparation is to achieve a clean and suitably roughened substrate to promote optimal adhesion. The concrete surface should be mechanically abraded to remove laitance, dust, and contaminants, followed by cleaning with alcohol or solvent wipes to eliminate any grease or loose particles. Proper surface prepara-

tion enhances the chemical bonding between the epoxy and the concrete substrate, thereby improving strain transfer efficiency and minimising local debonding.

(b) **Sensor placement.** Once the surface is prepared, the fibre is laid along the predefined route determined by the monitoring layout. Kapton tape or non-residual adhesive dots can be used to hold the fibre in place prior to bonding. The fibre must remain straight and in full contact with the substrate to prevent localised slack or uneven strain transmission.

(c) **Adhesive application and curing.** A thin, continuous layer of high-stiffness adhesive (typically epoxy) is applied to the fibre to ensure full encapsulation and intimate contact with the surface. The bond thickness should be minimised to prevent shear lag effects while maintaining adequate coverage for mechanical protection. Figure 2.10 illustrates the recommended adhesive distribution around the fibre. After application, the adhesive is allowed to cure under stable environmental conditions in accordance with manufacturer guidelines. During curing, maintaining light pretension in the fibre ensures stable strain coupling and prevents post-installation slack.

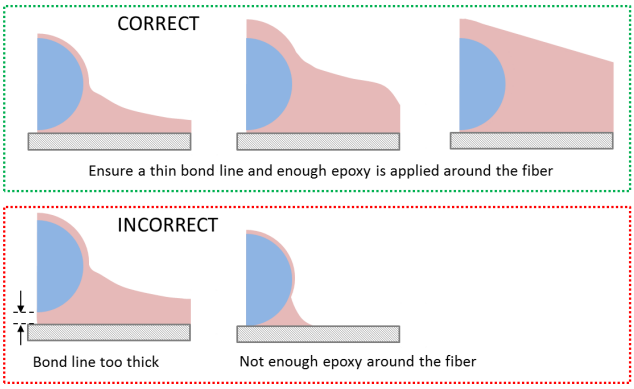

Figure 2.10: Optimal adhesive application around the fibre sensor cross-section [33].

After curing, an initial reference (tare) measurement is recommended to verify continuity and establish the baseline for subsequent strain readings. Protective coatings or overlays may also be applied for field installations to safeguard the bonded fibre from ultraviolet exposure, abrasion, and environmental degradation.

The installation procedure for surface-bonded Distributed fibre Optic Sensors (DFOS) is a critical step that directly affects measurement accuracy, strain transfer efficiency, and long-term sensor performance [30][31]. In existing structures, where embedding fibres within the concrete matrix is not feasible, surface bonding represents the most practical and widely adopted approach. This technique allows the optical fibre to be directly adhered to the structural surface, enabling monitoring of strain, crack formation, and thermal effects along the member length with high spatial resolution.

Prior to installation, the surface must be carefully prepared to ensure proper adhesion between the sensor and the substrate. The concrete surface is typically cleaned, dried, and ground to remove loose particles, laitance, and uneven textures. A smooth substrate minimizes microvoids and enhances the uniformity of the adhesive layer, which is essential for consistent strain transfer. The fibre is then positioned along the predefined measurement line and bonded using a thin, continuous layer of high-stiffness adhesive, such as epoxy. Excessive adhesive thickness should be avoided, as it can introduce shear deformation within the bond line and attenuate strain transfer from the host material to the fibre core.

After application, the adhesive is allowed to cure under controlled environmental conditions according to the manufacturer's specifications. During curing, the fibre should remain tensioned at a low, constant pretension level (typically 0.5–1 N) to prevent slack and ensure stable strain readings once the system is activated. Protective measures, such as covering the bonded fibre with a secondary coating, epoxy overlay, or protective tape, may also be applied to shield it

from mechanical abrasion, ultraviolet exposure, and temperature fluctuations, particularly in field installations.

The quality of the installation can be verified through initial reference measurements under unloaded conditions, which serve as the baseline for subsequent strain analysis. Properly executed surface-bonded installations have been shown to achieve strong strain coupling and long-term measurement stability comparable to embedded systems when suitable adhesives and installation protocols are adopted [4], [19]. Nevertheless, installation on rough or weathered concrete surfaces requires additional attention, as incomplete adhesion or trapped air pockets can lead to local strain loss or signal dropouts.

Overall, surface bonding provides a practical and versatile solution for deploying DFOS on existing bridges and other concrete structures. When combined with proper surface preparation, the use of stiff adhesives such as epoxy, and appropriate fibre protection, the method ensures high-fidelity strain transfer and durable performance under both service and ultimate loading conditions.

The discussion above shows that the performance of surface-bonded DFOS depends on several interacting factors, including the choice of fibre type and coating, the mechanical properties of the adhesive, the bond-line thickness and the quality of the installation procedure. Existing studies provide valuable qualitative and quantitative insights into these aspects, particularly for tension-dominated regions and laboratory conditions. However, a comprehensive installation strategy that links these parameters in a systematic and experimentally supported manner is still lacking, especially for applications on existing concrete structures. In addition, most experimental investigations of surface-bonded DFOS have focused on tension zones, while the behaviour of bonded fibres in compression regions remains less well understood. These observations underline the need for further experimental research on surface-bonded DFOS in reinforced concrete members, with the aim of developing a practical installation strategy and quantifying the associated strain-transfer efficiency, as addressed in Chapters 3 and 4 of this thesis.

2.2.4. Strain transfer from host material to the optical fibre

The continuous monitoring of strain is a fundamental aspect of Structural Health Monitoring (SHM) in civil engineering. Strain measurements are closely related to the stress state within the linear elastic range of structural materials, making them a primary indicator of a structure's mechanical condition and integrity. Since no simple or cost-effective stress-monitoring system exists for in-situ applications, strain is the most frequently monitored parameter in SHM [1]. Owing to the well-established relationship between stress and strain in the elastic regime, strain monitoring is widely regarded as the closest practical approach to direct stress assessment [1][34].

A significant challenge in the application of FOS, particularly DFOS, is understanding and accurately predicting the strain transfer effect [30][35]. This phenomenon refers to the discrepancy between the actual strain in the host structure (the material being monitored) and the strain measured by the optical fibre's glass core. The core of the optical fibre is inherently fragile, necessitating the use of protective coatings and, for surface-mounted applications, adhesive layers to ensure its integrity. These intermediate layers, having significantly lower Young's moduli than the fibre core, undergo shear deformation. This shear deformation means that only a portion of the structural strain is transferred to the fibre core, resulting in a "strain loss" that can lead to measurement inaccuracies if not properly accounted for [30]. Based on this information, the ideal situation will be the absence of protective coating and adhesive layer, and a perfect bond between the host and the fibre core. It is however, impractical to work with bare optical fibres, since they are extremely fragile. Glass fibres are brittle and readily fractured even when subjected to stresses generated from slight bends and curls along their lengths. The coating protects the glass core against this brittle fracture by providing a cushioning effect that absorbs a portion of the mechanical energy imparted to the fibre. A variety of coating materials are used as the protective layer for optical fibres. The most commonly employed coatings include a number of polymeric, silicon, and acrylic materials [36].

In most of the publications showing practical applications of DFOS monitoring, this problem is neglected,

and the structural strains are assumed to be equal to the fibre strains, which is not always true. However, in the past, researchers have extensively focused on understanding the strain transfer effect, which describes the discrepancy in the host structure and the strain measured by an optical fibre's glass core. The strain transfer mechanism differs between surface-bonded [8], [30], [31], [35], [37], [38], [39], [40] and embedded optical fibres [8], [26], [36], [39], [41], [42], [43], primarily because the surrounding medium governs how strains are transmitted from the host material to the sensor. As a result, different strain transfer theories have been devised in the past for both types of application. This thesis focuses on surface-bonded optical fibres, as the objective is to monitor existing structures where embedding sensors within the material is not feasible.

It should be clarified that the equations presented in this thesis refer to strain changes and not absolute strains, since DFOS measurements are always taken relative to an initial zero reading. A more precise notation would therefore be $\Delta\varepsilon$ instead of ε. Nevertheless, because this distinction is often omitted in the literature and to maintain clarity and simplicity, the term *strain change* will hereafter be used to denote *strain* by default.

2.2.5. Analytical Models for Strain Transfer in Surface-Bonded Optical Fibres

When an optical fibre is bonded to the surface of a deforming concrete member, the strain measured in the fibre is not necessarily equal to the strain at the concrete surface. The interposed adhesive layer and the fibre coatings deform in shear and govern how the deformation of the substrate is transmitted to the fibre core. This mechanism is generally referred to as *strain transfer*.

Her and Huang (2011) [30] developed a four-layer model for surface-bonded optical fibres consisting of the host material, adhesive, protective coating, and fibre core, as shown in Figure 2.11. A small interfacial gap between the substrate and the coating was included to replicate practical installation conditions.

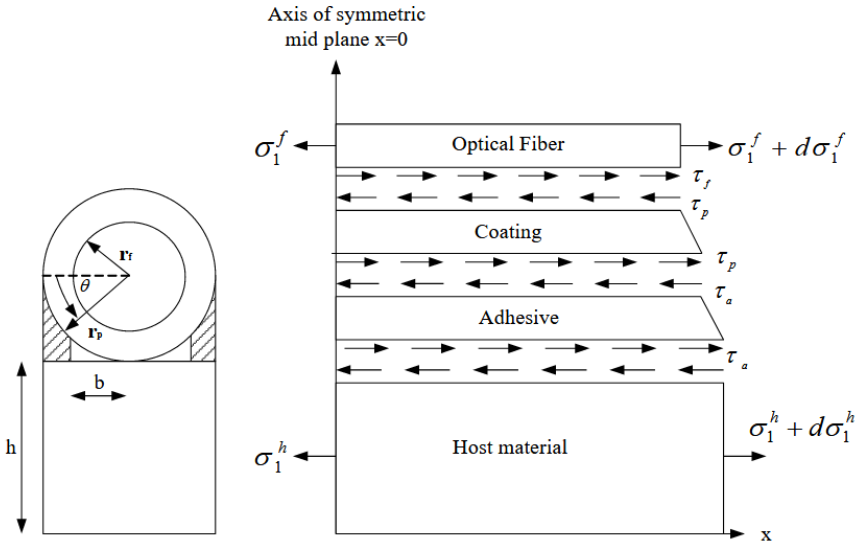

Figure 2.11: Analytical model of a surface-bonded optical fibre [30].

The model assumes linear elastic and isotropic materials, perfect interfacial bonding, and shear deformation limited to the adhesive and coating layers. The strain transfer is governed by a shear-lag parameter λ_1, which defines the exponential attenuation of strain between the host and the fibre. The analytical solution for fibre strain is expressed as:

$$\varepsilon_f(x) = \frac{\varepsilon_0}{E_f\left(\frac{\pi r_f^2}{2hr_pE_h} + \frac{1}{E_f}\right)}\left[1 - \frac{\cosh(\lambda_1 x)}{\cosh(\lambda_1 L_f)}\right] \tag{2.2}$$

where ε_0 is the host strain, E_f and E_h are the Young's moduli of the fibre and host, and r_f, r_p, and h are the geometric parameters of the fibre, coating, and adhesive layers. The shear-lag term λ_1 is the dominant term in Equation 2.2 which is directly dependent on the bonded length. Hence, the model effectively describes strain transfer over short bonding lengths, as in FBG applications, but becomes less representative for long, continuously bonded fibres where the strain distribution is more uniform and the effect of transfer length becomes negligible.

Wan et al. [40] investigated strain transfer in surface-attached optical fibre sensors through both analytical and numerical methods. Their study highlighted that classical shear-lag formulations yield accurate results only when the adhesive layer is relatively soft, corresponding to a low shear-lag parameter. For stiffer adhesives or bare fibres, analytical models tend to overpredict strain transfer efficiency. To overcome these limitations, the authors developed a three-dimensional finite element model (3D-FEM) that captured stress concentrations and complex interfacial behaviour. Furthermore, an experimental investigation was carried out for verifying the results.

The numerical study showed that the strain transfer coefficient is mainly influenced by the bond length and the bottom thickness of the adhesive layer, whereas the side width and top thickness have negligible effects. It was recommended that the bond length be maximised and the adhesive bottom thickness minimized to reduce measurement error. Coated fibres with soft primary coatings were also found to be less sensitive to geometric variations, improving measurement stability. However, in this study, the bond length used was relatively small (10-60 mm), which is not the case for a typical DFOS application.

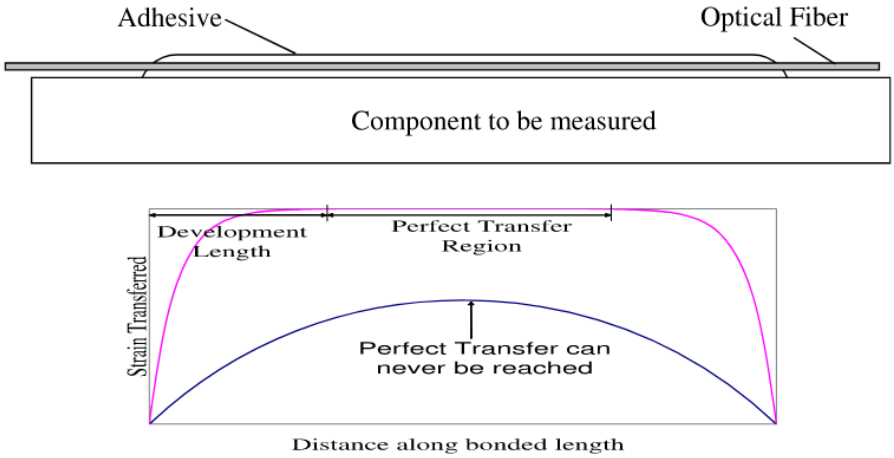

Figure 2.12: Installation of strain sensor with shear lag under uniform strain field (as conducted by Wan et al [40]).

For surface-bonded optical fibre sensors, several other studies have investigated how efficiently strain is transmitted from the host structure to the fibre core. Betz et al. [44] used finite element analysis and experiments on patch-bonded FBG sensors, where the fibre is first attached to a backing layer and this patch is then glued to the structural surface. They showed that, for a substrate strain of about 0.3% parallel to the fibre, the strain in the fibre core ranged only between approximately 0.26–0.28%, indicating incomplete strain transfer due to the presence of the backing; the degree of loss depended on the backing thickness and Young's modulus. Lin et al. [45] compared different packaging methods and reported that strain transmission decreases as the thickness of the surrounding steel tube increases, while the thickness and stiffness of the adhesive itself had relatively little influence in their tests. Li et al. [46] and Zhou et al. [47] further observed that strain transmission losses remain small when the substrate is thick and stiff relative to the bonding layer and the sensor, but become significant when the substrate is thin and made of low-modulus materials. In addition, Jahani and Nobari [48] showed that, under dynamic loading, both the Young's modulus and shear modulus of common adhesives are

frequency-dependent due to their viscoelastic behaviour, implying that strain-transfer characteristics may vary with loading rate.

Comparative limitations of existing Strain Transfer Models

Across the analytical and numerical studies reviewed above, most models focus on identifying how parameters such as adhesive thickness, bond length, coating stiffness and interfacial shear properties influence strain transmission. They are valuable for understanding the mechanics of strain transfer and for improving bonding conditions, but are generally formulated for short, locally bonded sensors (e.g. FBGs or patch-mounted gauges) and mainly describe the relative efficiency of strain transmission under idealised conditions.

Even when nearly ideal bonding is assumed, the strain recorded by a surface-bonded optical fibre remains lower than the true surface strain of the concrete. Existing formulations do not explicitly quantify this residual difference for long, continuously bonded DFOS installations. Analytical strain-transfer models should therefore be regarded primarily as conceptual tools rather than direct predictors of DFOS measurements in practice. This underlines the need for an experimental calibration of strain transfer for surface-bonded DFOS on reinforced concrete members, motivating the determination of an effective strain-transfer efficiency factor in the four-point bending tests presented in this thesis.

2.3. Crack width analysis using DFOS

A significant portion of damage observed in concrete bridge superstructures originates from cracking [49]. These cracks often lead to secondary deterioration mechanisms such as spalling and the exposure of reinforcing steel. In current inspection practices, the assessment of crack patterns is typically carried out visually, with crack widths either estimated from experience or measured manually using a crack width gauge. Such methods are inherently labor-intensive and prone to human error [20].

Distributed fibre Optic Sensors (DFOS) offer an advanced alternative by providing high-resolution strain profiles along the surface or within the cross-section of a structure. This allows the detection of localized strain concentrations associated with crack formation. Unlike conventional point sensors, DFOS captures the entire strain distribution, enabling both the precise localization and quantification of crack openings with micrometer-scale precision (Figure 2.6).

2.3.1. Methodology for DFOS-based crack width estimation

The reliable conversion of distributed strain data into physical crack widths requires a robust analytical model. Among the existing approaches, the methodology proposed by Richter et. al. [50] offers a systematic means to interpret DFOS strain peaks and has been widely referenced in recent studies for crack width estimation.

Figure 2.13 presents the general workflow used for crack width determination from DFOS measurements, summarizing the sequence of data processing and analytical steps.

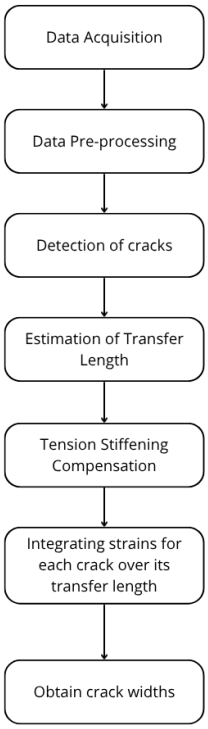

Figure 2.13: Workflow for determining crack width [50].

i) **Data acquisition**

The data is acquired using Luna Inc. optical distributed sensor interrogator (ODiSI) 6100 series. The exported file includes metadata describing the ODiSI system and the connected DFOS, as well as measurement parameters such as gage pitch and sampling rate. It also provides the gage positions and strain measurements with their corresponding timestamps, where each entry consists of a timestamp, data type, and an array of strain values.

ii) **Data Pre-processing**

In this step, the data is prepared for further analysis which entails further analysis. DFOS data typically contains three types of disturbances that must be addressed: noise, Strain Reading Anomalies (SRAs), and dropouts [50]. Noise is inherent to the measuring technology, stemming from finite equipment accuracy and the random nature of photon scattering. Noise reduction is often achieved by taking the mean of several measurements (ensemble average) and subsequently applying smoothing, such as the symmetrical sliding mean along the DFOS length, which is advantageous because it does not alter the strain integral. SRAs are artifacts resulting from incorrect cross-correlation findings, appearing as unpredictable, extreme strain readings in single gages. SRAs should be identified and cancelled before smoothing, often by applying criteria like the Geometric Threshold Method (GTM) or a threshold on the associated Spectral Shift Quality (SSQ), and setting the readings to ”not a number” (NaN). Dropouts also manifest as NaNs and occur when cross-correlation fails, particularly accumulating in high strain areas like cracks. Dropouts require special treatment, which can involve eliminating the gages with NaN entries (which equates to implicit interpolation for singular entries) or repairing the data by replacing NaNs with virtual, reconstructed values derived from surrounding intact data. The effectiveness of the subsequent peak detection step is highly dependent on the quality of this initial data pre-processing.

iii) **Detection of cracks**

Cracks in a concrete structure manifest as sharp peaks in the measured strain profiles obtained from the fibre. The corresponding crack locations, denoted as $x_{\mathrm{cr},i}$, are identified using peak-detection algorithms specifically developed for this purpose.

The key parameter governing peak identification is the prominence, which quantifies how much a particular peak stands out relative to the surrounding strain signal. To distinguish true crack-induced peaks from those caused by random noise or measurement artefacts, a minimum prominence threshold, $P_{\min}$, must be defined. If $P_{\min}$ is set too low, minor fluctuations in the strain signal may be falsely classified as cracks, leading to an overestimation of the total number of cracks. Conversely, if the threshold is set too high, smaller yet legitimate cracks may remain undetected, which can result in overestimation of the widths of the remaining identified cracks.

A second necessary criterion for crack identification is the absolute peak height (h_{min}). A strain peak is generally classified as a crack only if its magnitude exceeds the concrete's ultimate tensile strain, $\varepsilon_{\mathrm{ctu}}$, which typically lies around $100\ \mu\varepsilon$ for normal-strength concrete.

The reliability of the crack detection process is highly dependent on the quality of the pre-processed DFOS data. Smoothing or filtering operations, although effective for noise reduction, can attenuate peak prominence and thereby influence the required threshold value. Consequently, the degree of smoothing and the chosen prominence threshold are interdependent and must be carefully calibrated according to the specific DFOS type, coating, and installation configuration.

In this study, we have heavily relied on the absolute peak height (h_{min}). This threshold was set to the ultimate tensile strain of concrete, considering the effect of the Strain transfer efficiency considered in this study. This gives us a good approximation of beyond what values can the strain peaks be considered as cracks in concrete.

iv) **Transfer length of a crack**

Strains are detected within the optical fibre's core, and these are transmitted from the surrounding material to the fibre through the bonding layer, which inevitably introduces a strain lag. Consequently, the theoretically infinite strain peak that would occur at a crack location becomes distributed along both sides of the DFOS. The stiffness of the bond depends on the material properties, layer thicknesses, and interfacial behaviour of all layers between the host material and the fibre core. A stiffer bond minimizes strain lag, reduces the transfer length, and leads to sharper, higher strain peaks.

Two approaches for estimating transfer length have been discussed in the literature:

- **The minimum approach:** The minimum approach, which cuts each side of a peak at the local minima between neighbouring peaks.

  Let $x_{\mathrm{cr},i}$ denote the i-th crack location (strain peak in the DFOS profile), and let $x_{\min,l}$ and $x_{\min,r}$ be the positions of the local minima in between the i-th peak and its left/right neighbouring peaks at $x_{\mathrm{cr},i-1}$ and $x_{\mathrm{cr},i+1}$, respectively. The transfer length ℓ_t delimits the integration window used to convert strain to crack width.

$$\ell_{t,\min}^{-} = x_{\mathrm{cr},i} - x_{\min,l}, \tag{2.3}$$

$$\ell_{t,\min}^{+} = x_{\min,r} - x_{\mathrm{cr},i}. \tag{2.4}$$

  This approach is mechanically accurate for reinforced concrete under constant bending moments or pure tension, and is an acceptable initial estimate.

- **The midpoint approach:** Another approach is setting the transfer length to half of the distance to the neighboring crack.

$$\ell^{-}_{t,\mathrm{mid},i} = x_{\mathrm{cr},i} - \tfrac{1}{2}(x_{\mathrm{cr},i-1} + x_{\mathrm{cr},i})\,, \tag{2.5}$$

$$\ell^{+}_{t,\mathrm{mid},i} = \tfrac{1}{2}(x_{\mathrm{cr},i} + x_{\mathrm{cr},i+1}) - x_{\mathrm{cr},i}. \tag{2.6}$$

This approach is less prone to noise-induced minima. Hence is more stable on a strain data with an erratic signal.

Figure 2.14 shows a visual comparison between both approaches.

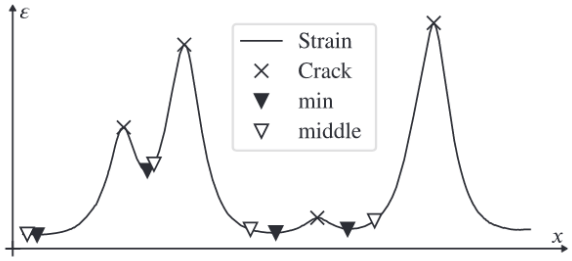

Figure 2.14: Visual comparison of transfer length approaches [50].

v) **Tension Stiffening compensation**

The load-bearing contribution of concrete between cracks, known as tension stiffening (TS), significantly influences the strains measured by DFOS [51]. When concrete cracks, the reinforcement continues to carry tension, while the adjacent concrete between cracks still resists part of the load through bond interactions with the reinforcement. As a result, the DFOS strain signal reflects not only the crack opening displacement but also elastic deformation in the concrete between cracks. This elastic portion must be compensated for to correctly estimate the crack width [50].

For DFOS bonded to the concrete surface, the total measured strain $\varepsilon_{\mathrm{DFOS}}$ in the cracked region is composed of two components: (i) the crack-induced strain, related to the actual opening of the crack, and (ii) the tension stiffening strain, $\varepsilon_{\mathrm{c}}^{\mathrm{TS}}(x)$, representing the reintroduction of strain into the concrete away from the crack. The latter is typically idealized as a linearly decaying function from the crack face:

$$\varepsilon_{\mathrm{c}}^{\mathrm{TS}}(x) = \min\left(\delta_i(x) \cdot \varepsilon_{\mathrm{m}}(x), \varepsilon_{\mathrm{cu}}\right) \tag{2.7}$$

where $\varepsilon_{\mathrm{cu}}$ is the ultimate tensile strain of concrete, and $\delta_i(x)$ is a normalized distance factor from the crack position x_{cr}, expressed as:

$$\delta_i(x) = \begin{cases} \dfrac{x_{\mathrm{cr}} - x}{\ell_t^{-}} & \text{if } x \le x_{\mathrm{cr}} \\ \dfrac{x - x_{\mathrm{cr}}}{\ell_t^{+}} & \text{if } x > x_{\mathrm{cr}} \end{cases} \tag{2.8}$$

The limit strain $\varepsilon_{\mathrm{lim}}(x)$ defines the transition between the cracked zone and the uncracked concrete and is determined as:

$$\varepsilon_{\mathrm{lim}}(x) = \begin{cases} \min\left(\varepsilon_{\mathrm{c}}^{\mathrm{TS}}(x_{\mathrm{cr}} - \ell_t^{-}), \varepsilon_{\mathrm{cu}}\right), & \text{if } x \le x_{\mathrm{cr}} \\ \min\left(\varepsilon_{\mathrm{c}}^{\mathrm{TS}}(x_{\mathrm{cr}} + \ell_t^{+}), \varepsilon_{\mathrm{cu}}\right), & \text{if } x > x_{\mathrm{cr}} \end{cases} \tag{2.9}$$

The concrete's ultimate tensile strain, $\varepsilon_{\mathrm{cu}}$, can be estimated from its material strength as:

$$\varepsilon_{\mathrm{cu}} = \frac{f_{\mathrm{ctm}}}{E_{\mathrm{cm}}} \tag{2.10}$$

where f_{ctm} is the mean tensile strength and E_{cm} is the modulus of elasticity of concrete. Typically, $\varepsilon_{\mathrm{cu}}$ is about $100\ \mu\varepsilon$ for normal-strength concrete.

To account for the TS effect when determining crack widths, the strain corresponding to the TS region must be subtracted from the total DFOS strain before numerical integration. This correction ensures that only the strain directly contributing to crack opening is included, thereby improving the accuracy of the calculated crack width [50].

vi) **Integration to obtain crack widths**

Once the strain peaks corresponding to cracks are identified and the tension stiffening (TS) component is compensated, the crack width can be determined by integrating the strain distribution along the optical fibre over the transfer length associated with each crack. Figure 2.15 illustrates the principle of this calculation.

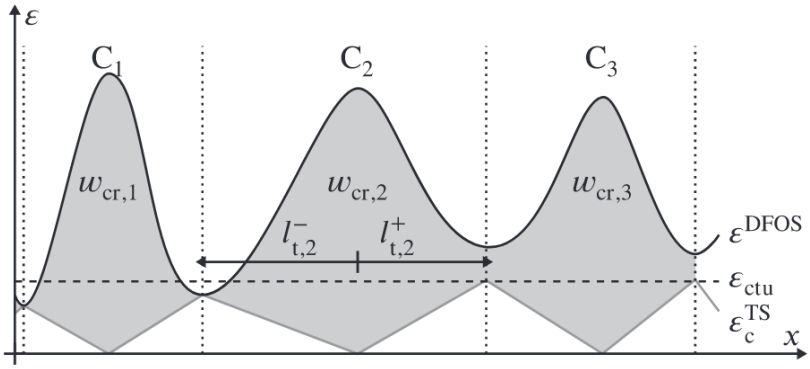

Figure 2.15: Crack width calculation for concrete DFOS (according to [50]).

For each crack i, the crack width $w_{\mathrm{cr},i}$ is computed as the integral of the differential strain between the measured DFOS strain $\varepsilon_{\mathrm{DFOS}}(x)$ and the compensated strain $\varepsilon_{\mathrm{c}}^{\mathrm{TS}}(x)$ over the transfer lengths on both sides of the crack:

$$w_{\mathrm{cr},i} = \int_{x_{\mathrm{cr},i}-\ell_t^-}^{x_{\mathrm{cr},i}+\ell_t^+} \left(\varepsilon_{\mathrm{DFOS}}(x) - \varepsilon_{\mathrm{c}}^{\mathrm{TS}}(x)\right) dx \tag{2.11}$$

This approach ensures that only the deformation directly attributable to crack opening is integrated, while the elastic strain reintroduced through tension stiffening is excluded. The integration boundaries, defined by the transfer lengths ℓ_t^- and ℓ_t^+, correspond to the local minima surrounding each strain peak, as illustrated in Figure 2.14. In practice, the integral in Equation (2.11) is computed numerically using the discrete DFOS strain measurements.

By combining precise peak localization, tension stiffening compensation, and numerical integration, this method enables accurate estimation of individual crack widths and their evolution under increasing load, providing a continuous and quantitative alternative to traditional visual crack assessment.

Limitation of crack-width estimation using DFOS

Existing studies have shown that DFOS can be used to detect cracks and, using methods such as the Richter et. al. [50] procedure, to estimate crack widths from distributed strain profiles. These approaches provide a clear workflow for peak detection, tension-stiffening compensation and integration, and have yielded promising results in laboratory conditions.

However, the reliability of DFOS-derived crack widths for reinforced concrete members is still not fully established. In particular, the influence of strain-transfer effects, missing or degraded data (e.g. gaps in the strain profile) and processing choices on the accuracy of the estimated crack widths has not been quantified in a systematic way. As a result, it is unclear under which practical conditions DFOS-based crack widths can be considered trustworthy for structural assessment. This motivates the experimental investigation in this thesis into the accuracy and robustness of crack-width estimates obtained from DFOS.

2.4. Application of Distributed Fibre Optic Sensing

The previous sections outlined the theoretical foundations of Distributed Fibre Optic Sensing (DFOS). Having established these principles, it is essential to examine how DFOS has been implemented in practical structural health monitoring (SHM) applications. Most formulations used to evaluate and control crack width have traditionally been developed for tensile and flexural cracking [49].

In recent years, Distributed Fibre Optic Sensing (DFOS) has been widely applied to study flexural behaviour and crack development in reinforced and prestressed concrete members, owing to its high spatial resolution and sensitivity to strain localization. Beyond flexural applications, several studies have demonstrated the capability of DFOS to identify shear cracking mechanisms and to monitor the long-term performance of bridge structures under service conditions. The following subsections summarize representative laboratory and field investigations that demonstrate these applications.

2.4.1. Shear crack identification using DFOS (Laboratory)

Rodríguez et al. (2016) [49] conducted one of the earliest experimental studies demonstrating the potential of Distributed Fibre Optic Sensors to monitor the evolution of shear cracks in concrete elements. Their work focused on partially prestressed concrete (PPC) beams tested under shear-dominated loading conditions. A single optical fibre, bonded along the web of each beam, was connected to an Optical Backscatter Reflectometer (OBR) system operating on the Rayleigh scattering principle (see Figure 2.16). This setup enabled the acquisition of distributed strain profiles with a high spatial resolution, allowing for the visualization of the strain field throughout the loading process.

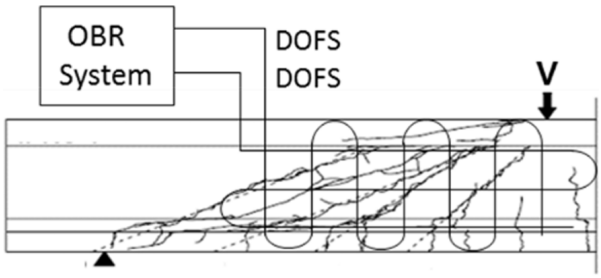

Figure 2.16: Rectangular 2D mesh formed by the DFOS for characterization of shear cracking [52].

The study revealed that DFOS measurements could capture both the initiation and propagation of shear cracks, even before they became visible on the concrete surface as shown in figure 2.17. The localised strain peaks recorded by the fibre corresponded closely to the positions and orientations of visually identified cracks. Furthermore, the strain evolution at specific points along the fibre provided insight into the progressive development of shear mechanisms in the web region. This confirmed that distributed sensing is capable of detecting inclined crack formation and its growth with load increments.

Although the results showed good agreement with conventional strain measurements, the authors highlighted several limitations. In particular, the presence of high strain gradients near cracks occasionally caused partial signal losses due to fibre slippage or local debonding. Moreover, because only one fibre was installed along the web, the system could not reconstruct the two-dimensional strain field or quantify crack widths directly. Nevertheless, this pioneering study established that DFOS can serve as a reliable tool for detecting and tracking the formation of shear cracks in prestressed concrete members, providing a foundation for future research on two-dimensional distributed sensing configurations.

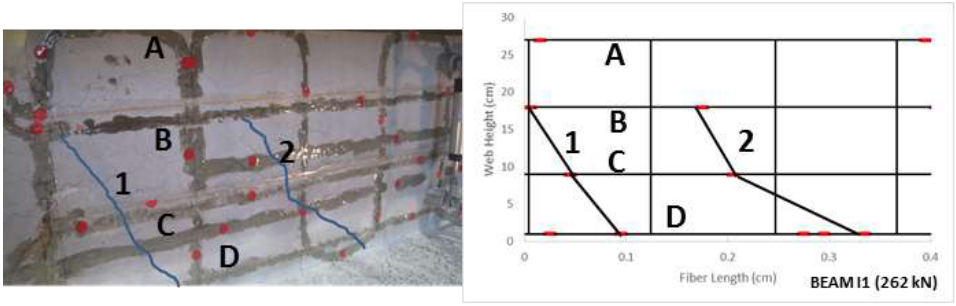

Figure 2.17: Correlation between shear crack pattern through visual inspection and peak detection by OBR system [49].

Later, Rodríguez et al. (2019) [52] expanded their research by proposing a two-dimensional (2D) Distributed Optical Fibre Sensing configuration for the comprehensive assessment of shear cracking in reinforced concrete (RC) elements. The study aimed to determine not only the presence and location of shear cracks but also their width and inclination, allowing for a more complete characterization of the crack pattern.

The experimental campaign involved large-scale reinforced concrete beams tested under four-point bending conditions dominated by shear. The optical fibre was placed in a grid pattern with one series of fibre aligned longitudinally and the other placed vertically, creating a two-dimensional sensing grid (See Figure 2.18 and Figure 2.19). This configuration made it possible to reconstruct the strain field across the web area and to identify the orientation of inclined cracks. Measurements were performed using an OBR based on Rayleigh scattering, which provided a spatial resolution of approximately 2.6 mm.

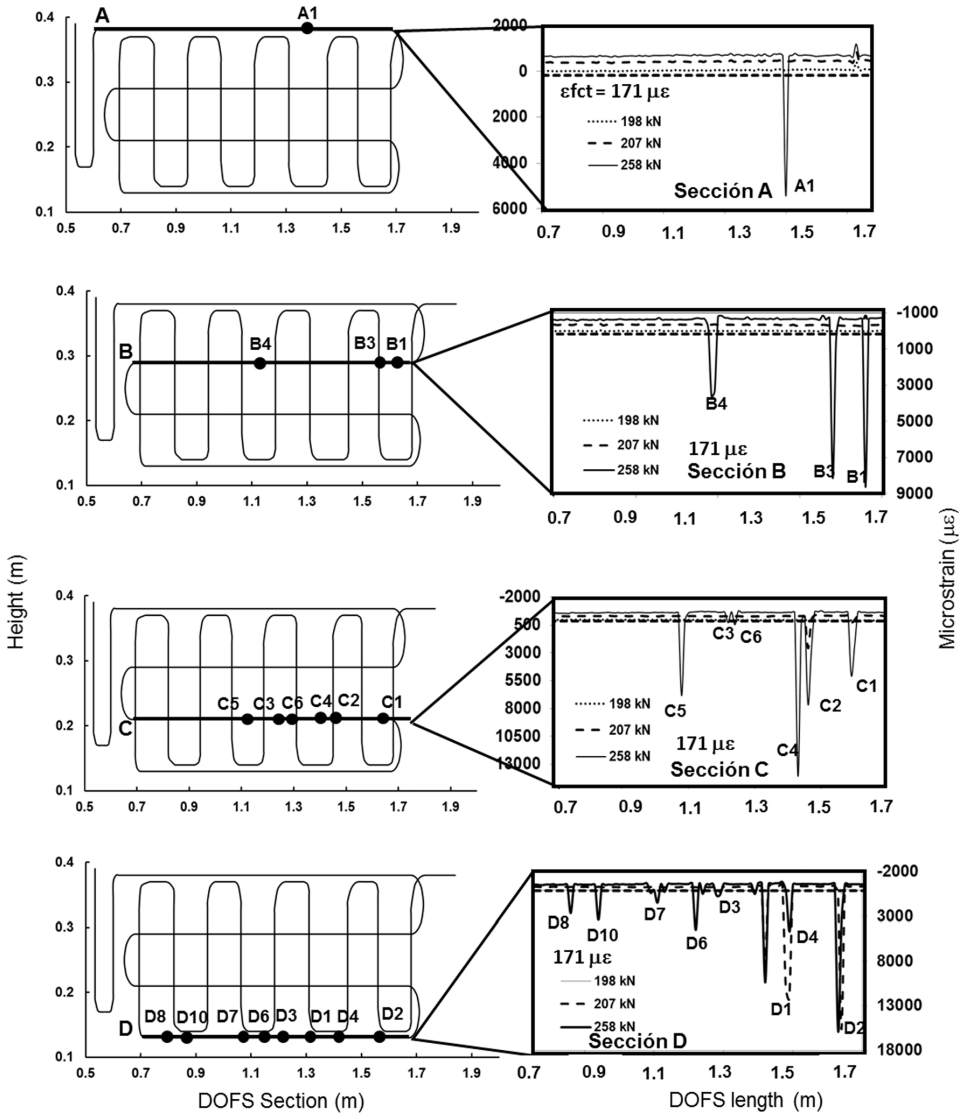

Figure 2.18: Strain distribution and crack location in horizontal sections at different load levels [52].

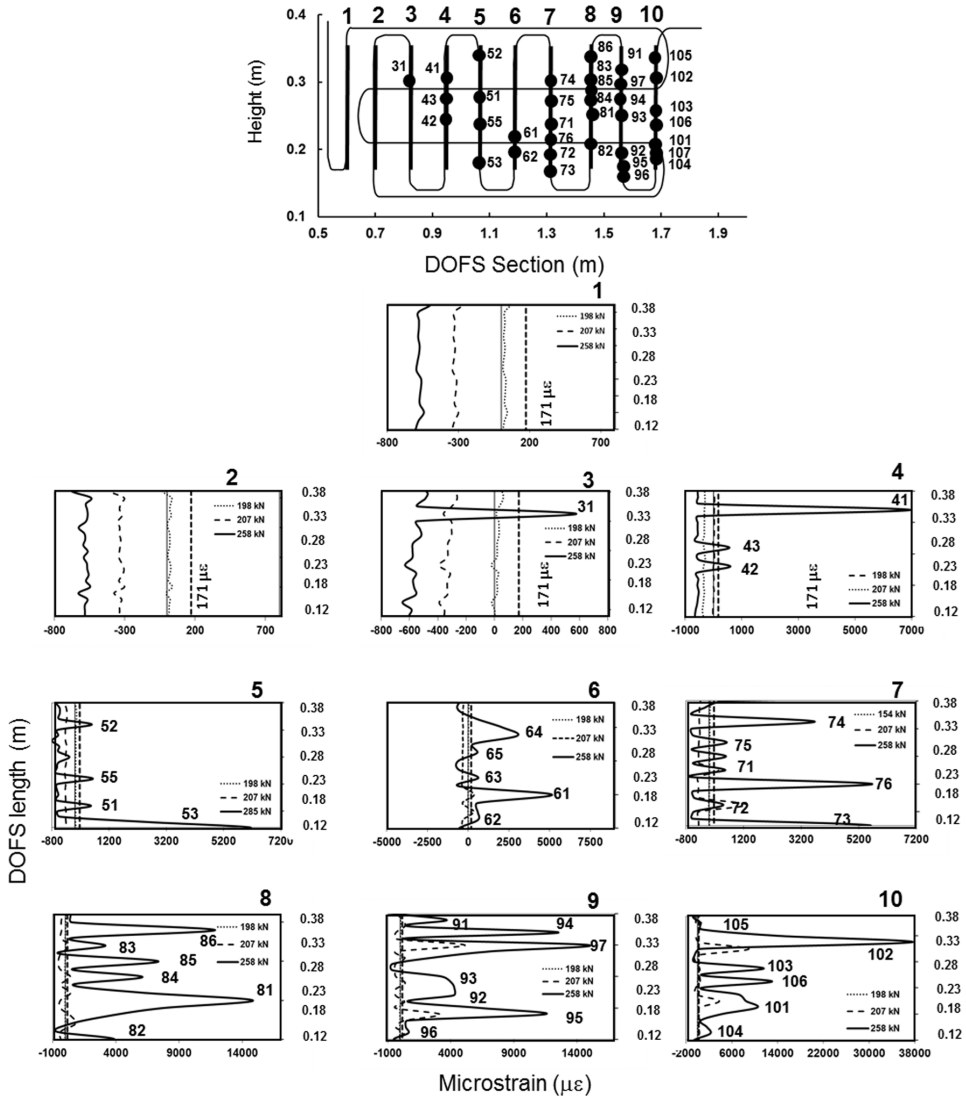

Figure 2.19: Strain distribution in vertical sections at different load levels [52].

The results showed that the DFOS system successfully captured the formation and evolution of inclined shear cracks. By integrating the strain peaks obtained along the diagonal fibres, the researchers were able to estimate local crack widths and orientations with high spatial precision. Furthermore, combining the strain readings from the longitudinal and vertical fibres allowed for the reconstruction of the entire shear crack network within the web region. The DFOS-derived results were validated against digital image correlation (DIC) and conventional visual inspection, both of which confirmed the accuracy of the distributed measurements.

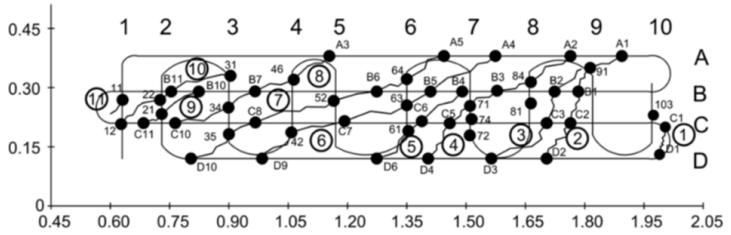

Figure 2.20: Shear cracking pattern of beam at 258 kN [52].

Despite the promising outcomes, the authors identified certain practical challenges, including localised signal loss in high-strain zones and sensitivity to installation quality, particularly at fibre intersections. Nevertheless, the study demonstrated that a properly designed 2D DFOS layout can provide both quantitative and qualitative information on the shear cracking behaviour of reinforced concrete members, marking a significant step forward from previous one-dimensional DFOS applications.

Rodríguez et al. (2019) demonstrated that DFOS can also be used to determine the angle of the shear cracks. The crack angle, θ_{cr}, was calculated from the strain peaks obtained at the specific coordinates along the horizontal and vertical fibres.

In this sense, the trace of the shear cracking pattern also allows the calculation of the shear crack angles. These angles can be obtained in detail with respect to the horizontal beam axis using the point coordinates that define the beginning and end of each crack. Table 2.2 presents the measured shear crack angles at several points for a beam at a load level of 258 kN, together with the mean angle for each crack.

Table 2.2: Shear crack angles of the beam at 258 kN [52].

Crack	Point	X (m)	Y (m)	Angle (°)
1	D1	1.32	0.13	80.5
	73	1.31	0.19	8.7
	C2	1.44	0.21	44.6
	81	1.45	0.24	26.7
	B3	1.54	0.29	35.7
	97	1.56	0.21	31.2
	105	1.68	0.20	Mean = 33.4
2	D2	1.57	0.13	81.9
	92	1.56	0.20	26.6
	C1	1.58	0.21	58.0
	B1	1.63	0.29	11.3
	102	1.68	0.30	Mean = 44.4
3	D3	1.21	0.13	45.0

2.4.2. Application of DFOS on existing bridges

With the rapid advancement of distributed fibre optic sensing (DFOS), several bridge monitoring projects worldwide have demonstrated its capability for assessing both global structural behavior and localized damage phenomena. These applications have ranged from short-term load testing of reinforced concrete bridges to long-term monitoring of prestressed and cable-stayed systems. Each case study contributes to understanding how DFOS can be integrated into real infrastructure and how sensor placement, bonding method, and fibre type influence the quality of strain data obtained in field conditions. Some representative field applications of DFOS on full-scale bridges are summarized below, highlighting their measurement objectives, sensor layouts, and key findings for bridge assessment.

1. **Black River Bridge, Ontario**

   Regier and Hoult [53] conducted one of the earliest field applications of a Rayleigh backscatter-based DFOS system on a reinforced concrete bridge, the Black River Bridge in Ontario, Canada. The bridge consisted of two simply supported spans with four girders, where surface-bonded nylon-coated optical fibres were installed along the sides of the beams at the tension zone and near the support regions (see Figure 2.21). The Luna OBR 4600 interrogator was used with a long gauge length to record strain during static load tests using a five-axle truck. The DFOS results were validated against electrical strain gauges and displacement transducers, showing close agreement in both global strain trends and deflection profiles. Moreover, the distributed strain data enabled identification of local cracking behavior, curvature profiles, and partial fixity at the supports—features not captured by conventional sensors. This study demonstrated the potential of DFOS to simultaneously capture both localized damage and overall structural response

in reinforced concrete bridges under service loads.

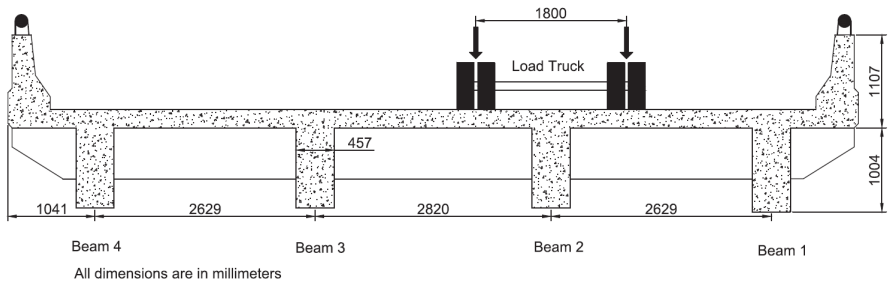

Figure 2.21: Section view of Black River Bridge [53].

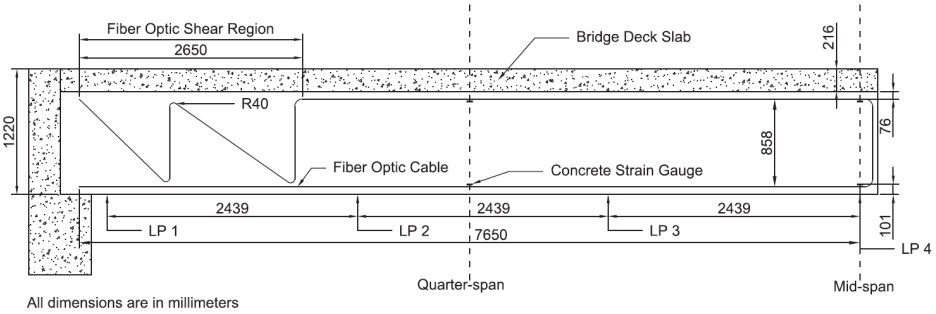

Figure 2.22: Instrumentation on Beam 2 of the bridge [53].

2. **Rędziński Bridge, Wrocław**

The Rędziński Bridge in Wrocław, Poland, is the largest concrete cable-stayed bridge in the country (See Figure 2.23). It is a four-span bridge with a total length of 50 m + 2×256 m + 50 m and an H-shaped pylon rising 122 m above the Odra River [5]. After ten years of service, multiple cracks were observed in the prestressed lower crossbeam connecting the inclined pylon legs. To monitor crack development and assess the long-term performance, the structure was equipped in 2020 with monolithic distributed fibre optic sensors (DFOS) developed by SHM System [5].

(a) **(b)**

Figure 2.23: (a) Rędziński Bridge in Wrocław, Poland: general view; (b) close-up of the lower crossbeam connecting two inclined legs of the pylon [5].

Four DFOS sensors were installed in near-to-surface grooves along the full length of the lower crossbeam, one in each corner, as shown in Figure 2.24. This configuration provided optimal bonding, mechanical protection, and thermal stability while maintaining aesthetic integrity. The system captured distributed strain data from over 7400 points per measurement, enabling precise detection of crack locations, monitoring of crack width variations, and evaluation of flexural behavior under both static and dynamic traffic loads.

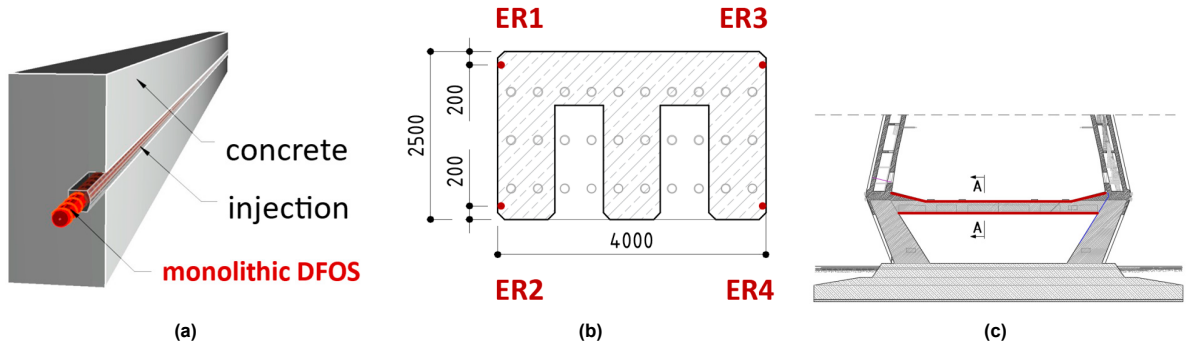

Figure 2.24: (a) Installation in near-to-surface grooves; (b) cross-section of the beam with locations of the sensors; (c) side view of the crossbeam with sensors marked over its length [5].

The DFOS data also provided insights into axial shortening, deflection, and local deformation of the pylon beam, demonstrating the potential of monolithic DFOS for permanent bridge health monitoring and quantitative crack width analysis under service conditions.

3. **Sarajevo Bridge, Barcelona**

Barrias et al. [17] presented one of the first full-scale bridge applications of DFOS in Spain, implemented on the Sarajevo Bridge in Barcelona. The monitoring aimed to assess the structural response during the widening of the bridge deck, as part of an infrastructure expansion project. The DFOS system employed the Optical Backscatter Reflectometry (OBR) technique based on Rayleigh scattering, providing a spatial resolution of 1 cm over a total sensing length of approximately 38 m.

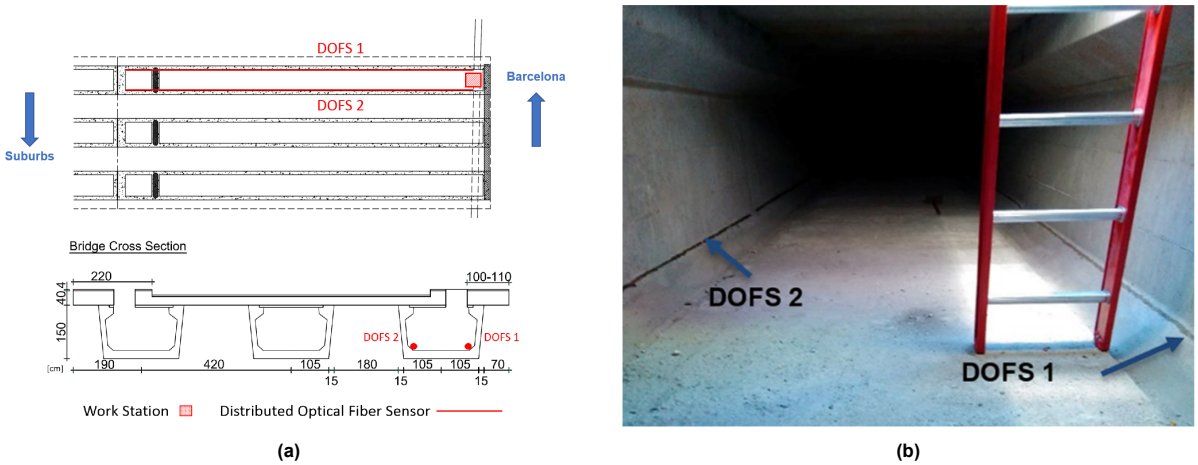

Figure 2.25: (a) General DFOS layout of DFOS in Sarajevo Bridge; (b)Photograph inside the box girder [17].

A polyimide-coated single-mode silica fibre was surface-bonded along the longitudinal direction of the concrete deck using a thin layer of bicomponent epoxy adhesive. The installation required careful preparation of the concrete surface to minimize roughness and ensure optimal bonding. Figure 2.25 illustrates the sensor deployment and installation stages.

Continuous measurements were collected during the deck replacement and widening phases to monitor strain redistribution and detect any local damage initiation. The DFOS system proved capable of tracking the evolution of strain fields during construction, showing that the strain increments remained below 100 $\mu\varepsilon$, consistent with service limit state behaviour. The distributed data confirmed uniform strain development across the monitored spans and no evidence of cracking or abnormal deformation.

These case studies demonstrate that DFOS can be effectively integrated into both laboratory-scale and field-scale applications, providing continuous strain data for detecting cracking, assessing structural performance, and validating analytical models. The success of these applications also highlights the importance of proper installation procedures, surface preparation, and system calibration to ensure reliable strain transfer and long-term monitoring performance.

3

Experimental Investigation of DFOS strain response

3.1. Overview and objectives

The previous chapter has shown that the performance of surface-bonded Distributed Fibre Optic Sensing (DFOS) depends strongly on the installation strategy and on the efficiency of strain transfer between the concrete surface and the fibre core. Existing guidelines for DFOS installation, such as manufacturer recommendations and published case studies provide useful qualitative advice, but they do not offer an experimentally validated strategy tailored to reinforced concrete members. Moreover,analytical strain-transfer models mainly describe idealised configurations and do not directly quantify how DFOS-measured strains relate to the true concrete surface strains under realistic installation conditions.

To address these issues, this chapter presents an experimental investigation of the strain response of surface-bonded DFOS on reinforced concrete members. The work is organised in two phases. In the first phase, existing installation guidelines were applied to a large inverted T-girder tested in three-point bending under shear-dominated loading. This test served as a pilot application in which practical difficulties such as data loss, noisy measurements and local debonding were encountered. The experience gained from this test was used to identify shortcomings in the existing installation recommendations and to formulate a set of improvements to the installation strategy.

In the second phase, the refined installation strategy was implemented in a series of four-point bending tests on reinforced concrete beams. In these tests, DFOS was combined with conventional strain gauges and Digital Image Correlation (DIC), enabling a quantitative comparison between distributed fibre strains and reference measurements in both tension and compression zones. Based on these comparisons, an effective strain-transfer efficiency factor is derived, which provides a practical relationship between DFOS-measured strain and the concrete surface strain for the specific surface-bonded configuration studied in this thesis.

The same tests are later used in Chapter 4 to investigate the ability of DFOS to detect cracks and to provide reliable crack-width estimates for reinforced concrete members.

3.2. Distributed Fibre Optic Sensing system

Distributed strain data were recorded using a Luna ODiSI 6100 Optical Distributed Sensor Interrogator [54], which operates based on the principle of Optical Frequency Domain Reflectometry (OFDR). The system provides fully distributed strain measurements along the optical fibre with high spatial and temporal resolution. For this experiment, a gage pitch (spatial resolution) of 1.3 mm was adopted, which means that strain readings were obtained every 1.3 mm along the length of the fibre. Although the system is capable of a minimum gage pitch of 0.65 mm, the coarser setting was chosen to reduce the large data volume associated with continuous high-resolution acquisition.

Before each test, a reference (tare) scan was recorded with the structure unloaded, following the procedure recommended in the ODiSI installation guide [25]. Subsequent strain profiles were then computed relative to this baseline, so that the reported strains correspond to changes from the tare state. For quasi-static loading, DFOS scans were acquired at selected load levels, typically by averaging multiple rapid acquisitions at each level to reduce random measurement noise.

The DFOS data were exported in `.tsv` format and subsequently processed in MATLAB for alignment and strain visualization. Peak detection was performed to identify localized strain concentrations corresponding to crack initiation and propagation. These strain peaks were then mapped along the beam length to generate a distributed crack profile.

For validation, DFOS measurements were compared with Digital Image Correlation (DIC) results obtained simultaneously on the beam. The DIC system provided full-field strain maps and visual crack patterns at each load step. Although the DFOS and DIC systems were installed on opposite faces of the beam, the comparison allowed a qualitative verification of crack initiation and propagation trends. Minor discrepancies between the two datasets were attributed to the asymmetric nature of crack development through the thickness of the beam.

Figure 3.1: LUNA ODiSI series 6 Interrogator

3.3. Phase 1 – Inverted T-girder with existing installation guidelines

3.3.1. Specimen and test configuration

The experiment was carried out on a large-scale precast inverted T-girder, representative of a typical bridge web element. The beam was designed to fail in shear under three-point bending, producing a dominant shear field within the web region and flexural behaviour near the bottom flange. The overall dimensions of the specimen and loading configuration are shown schematically in Figure 3.2. The test was conducted as part of a broader structural testing campaign on concrete bridge components [55], [56].

The primary purpose of this DFOS installation was not to contribute to the mechanical assessment of the beam, but rather to evaluate the sensor's response under exisiting installation practices to observe the qualitative strain development associated with cracking. The beam was incrementally loaded until failure using a 5000 kN capacity hydraulic jack, with measurements recorded at multiple load steps. The loading setup is shown in Figure 3.2.

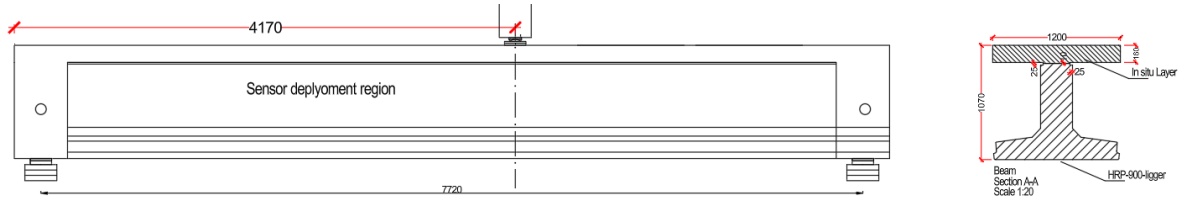

Figure 3.2: Test setup for the simulated simply supported three-point bending test (all dimensions in mm).

The girder was instrumented with a combination of DFOS, Digital Image Correlation (DIC) and a limited number of conventional sensors (e.g. LVDTs and lasers at selected locations). DIC was used to obtain full-field surface deformation and crack patterns, providing an independent reference for the interpretation of the DFOS data. The DFOS layout consisted of fibres routed along the web and flange surfaces of the girder, with the aim of capturing both global deformation and localised strain concentrations associated with shear cracking.

3.3.2. DFOS installation based on existing guidelines

For the inverted T-girder, the DFOS installation was carried out strictly following existing installation practices and manufacturer recommendations, without additional refinements. In particular, the procedure was based on the ODiSI Fibre Optic Sensor Installation Guide by Luna Inc. [25] and on practical examples reported in the literature for surface-bonded DFOS on concrete.

The optical fibre was installed on the web of the beam to monitor cracking, and on the side face using a surface-bonded configuration. As shown in Figure 3.3, the fibre was arranged in four horizontal laps along the web to capture the development of shear cracks and one lap along the bottom flange to observe flexural behaviour with each lap following a continuous path, returning at the beam end. However, the fibre in the topmost lap broke before the start of the test, and no readings could be obtained from that level. A new termination was therefore made on the second lap from the top. Each lap followed a continuous path, returning at the beam end.

The general procedure comprised three main steps:

- **Surface preparation:** the concrete surface was mechanically cleaned and lightly abraded using a sand paper in the regions where the fibre was to be bonded, followed by removal of dust and loose particles using compressed air and alcohol wipes.
- **Sensor placement:** the optical fibre was laid along the predefined route on the web and flange surfaces and temporarily fixed in place using small pieces of kapton tape at regular intervals, in accordance with the recommended spacing in the installation guide.
- **Adhesive application:** a two-component epoxy adhesive was applied over the fibre to form a continuous bond line between the fibre and the concrete surface. The adhesive was spread manually using a foam swab, aiming for a thin, uniform layer, and allowed to cure under ambient laboratory conditions before testing.

This procedure was considered representative of a typical implementation of surface-bonded DFOS in laboratory conditions when only generic installation recommendations are available, and no prior experience with the specific test configuration exists.

An ORMOCER-coated optical fibre [57] was used due to its good strain transfer capability and adequate robustness for handling in large-scale laboratory environments. The fibre was bonded to the concrete surface using a two-component epoxy adhesive (Driebond 8142) [58]. This adhesive was selected because it has previously shown reliable performance in similar applications [26]. Although the adhesive layer thickness was not strictly controlled, the bond quality was sufficient to capture the relative strain variations required for qualitative crack identification. The installation procedure followed the guidelines provided in the ODiSI Fiber Optic Sensor Installation Manual [25], as described in Section 2.2.3.1.

Figure 3.3: DFOS layout with four laps in the web (shear) and one in the flange (flexure).

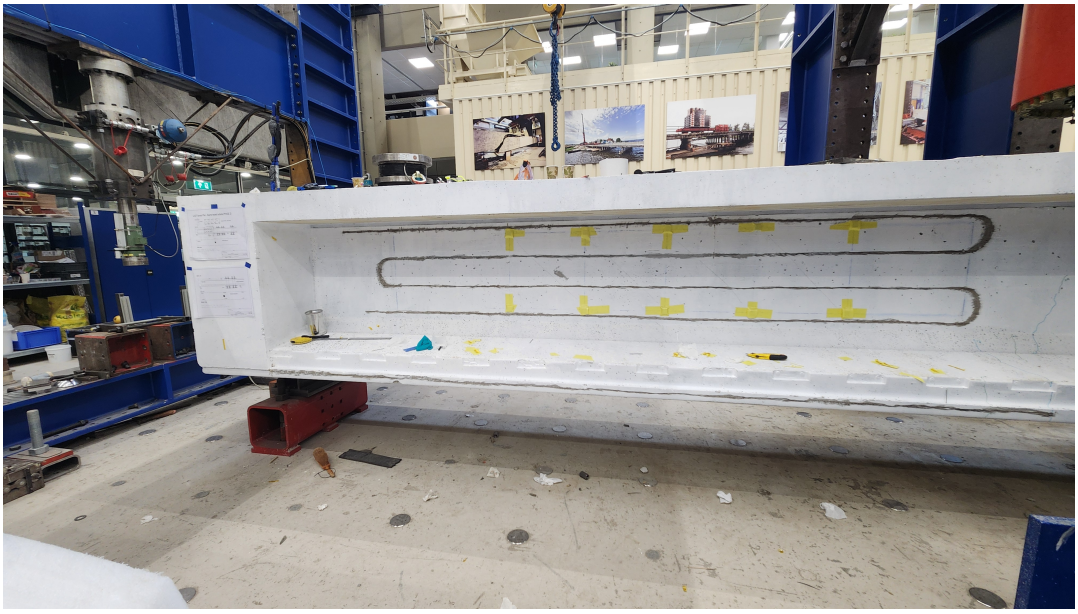

Figure 3.4: Installed surface-bonded DFOS on the specimen.

3.3.3. Observed issues and lessons learned

From the inverted T-girder test, the DFOS data quality revealed several shortcomings of an installation approach based solely on generic guidelines. In particular, the following issues were observed:

- The bonding between the fibre and the concrete surface through the epoxy layer was not uniform and consistent. At some locations, excessive adhesive was present between the fibre and the concrete, while in other locations the fibre was in direct contact with the surface with only a thin surrounding adhesive layer. This non-uniform bondline thickness is expected to cause spatially variable strain-transfer efficiency.
- During adhesive application, the fibre was not always kept under uniform pretension and straightness. Local slack or waviness of the fibre was observed before curing, which can lead to apparent strain offsets and measurement artefacts once the structure is loaded.
- At small surface voids or imperfections, the fibre exhibited visible signs of local debonding or imperfect contact, which were later reflected in the strain profiles as noisy or unreliable readings.

Although the DFOS measurements on the T-girder were still useful for qualitative crack detection and for visualising the overall shear crack pattern (results presented later in Chapter **??**), the test clearly showed that an installation strategy based only on generic recommendations does not provide the level of robustness and quantitative reliability required for strain-transfer analysis.

These observations underline that existing installation guidelines, while useful as a starting point, do not constitute a fully defined and experimentally validated installation strategy for surface-bonded DFOS on concrete. In the second phase of the experimental programme, involving four-point bending beams, these lessons were translated into a refined and more explicit installation procedure. This refined strategy and its impact on strain-transfer behaviour are described in Section **??** and form the basis for the quantitative strain-transfer analysis presented later in this chapter.

3.4. Phase 2 - Four-point bending beam tests with refined DFOS installation

Following the pilot application on the inverted T-girder, a second experimental series was carried out on reinforced concrete beams tested in four-point bending. In this phase, the practical lessons from the T-girder were translated into a refined installation strategy for surface-bonded DFOS, and the resulting strain measurements were used for quantitative strain-transfer analysis. A total of four reinforced concrete beams of size 1900x150x200 mm^3 were cast. Each specimen was equipped with a different reinforcement specification. This was decided to obtain different crack patterns for the crack width analysis of the concrete using DFOS.

3.4.1. Specimen details

3.4.1.1. Concrete

The concrete used in this experiment is based on the concrete type C34/45, which is commonly used in construction practice. The concrete mixture is shown in Table 3.1

Component	**Specification**	**Weight [kg/m^3]**
Cement	CEM III/B 42.5 N	357
Sand	River sand 0/4 mm	816
Gravel	River gravel 4/16 mm	1065
Water		160
Admixtures	Superplasticiser con. 20%	1.428
	Total	**2399**

Table 3.1: Proportion of concrete mix

Figure 3.5 shows the timber moulds used for casting the concrete beam specimens with internal dimensions 1900x150x200 mm^3 (Lxbxh). Additionally, concrete cubes with dimensions of 150x150x150 mm^3 were cast to follow the concrete strength development for 28 days. The specimens were cured inside a curing chamber with 20°C temperature and 95% relative humidity. As can be seen from Table 3.2, the mean concrete cube compressive strength $(f_{cm,\text{cube}})$ at the end of of curing period of 28 days was found to be 56.9 MPa.

Figure 3.5: Mould for casting concrete beam specimens

Concrete cube	Compressive strength after 28 days [MPa]	Mean strength [MPa]
1	55.64	56.91
2	55.48	
3	59.60	

Table 3.2: Concrete compressive strength after 28 days

3.4.1.2. Reinforcement

The longitudinal reinforcement bars used consist of ribbed steel bars with nominal diameters ϕ8, ϕ10, and ϕ 12 mm, grade B500 (ductility class B/C), in accordance with EN 1992-1-1 and the relevant product standard. The characteristic yield strength is f_{yk}=500 MPa. The Young's modulus of elasticity is taken as E_s = 200 GPa.

For each specimen, different combinations of longitudinal reinforcement diameters were used to achieve

Table 3.3: Mechanical properties of reinforcing steel used in this study

Bar diameter (mm)	Grade	f_{yk} [MPa]	E_s [GPa]
∅8, ∅10, ∅12	B500 (B/C)	500	200

varying reinforcement ratios. The variation in reinforcement was intentionally selected to produce distinct cracking behaviours across the specimens, allowing the evaluation of how effectively DFOS can identify closely spaced cracks and large crack widths. Consequently, by altering the reinforcement ratio, differences in both crack spacing and crack widths were observed among the four beams. The details of the longitudinal reinforcement detailing is shown in Figure 3.4

In terms of shear reinforcement, only the regions between the support and the nearest loading point (a distance of 300 mm) were provided with stirrups. This configuration was adopted to prevent the shear reinforcement from influencing the crack formation in the constant moment region while ensuring adequate shear capacity to avoid premature shear failure. Although the calculated shear capacity of concrete $(V_{\mathrm{Rd},c})$ was sufficient for the applied loading, it was included as a precautionary measure to suppress unintended shear cracking and to ensure that flexural cracking remained the dominant failure mechanism in the test specimens. The shear stirrups were secured to the longitudinal bars using metal arc welding. The detailing and spacing of shear reinforcement can be seen in Figure 3.6. The assembled reinforcement cage with 12mm diameter bars can be seen in Figure 3.7.The dimensions and reinforcement configuration of the beam is shown in Figure 3.8 and Figure 3.9.

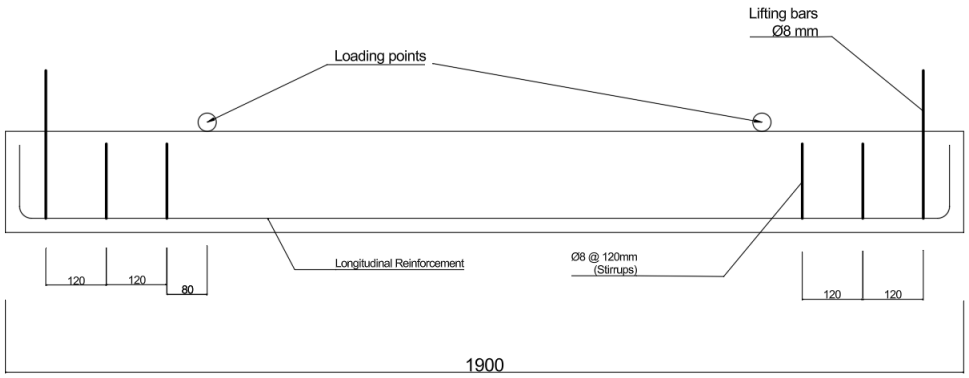

Figure 3.6: Reinforcement detailing (all dimensions in mm)

Figure 3.7: Assembled reinforcement cage

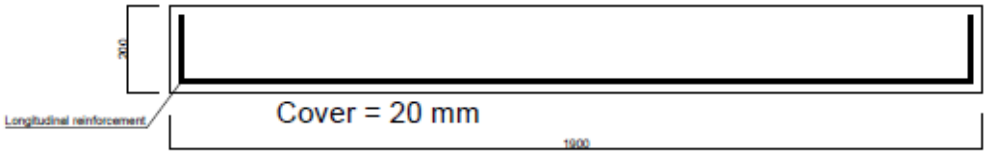

Figure 3.8: Longitudinal section of the specimens (all measurements in mm

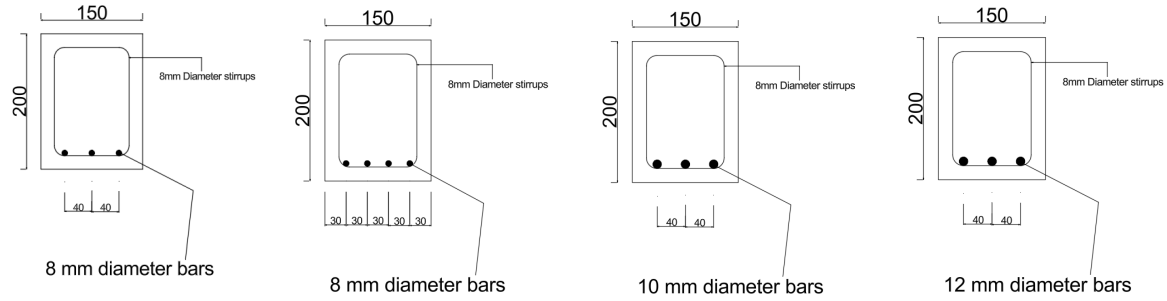

(a) Specimen 1: R3D8-AR47 **(b)** Specimen 2: R4D8-DB **(c)** Speciemen 3: R3D10-CN **(d)** Specimen 4: R3D12-AR14

Figure 3.9: Cross-section of specimens (all dimensions in mm)

3.4.2. Nomenclature of the specimen

Each beam has been assigned a specific code name in order to get all the details regarding the specimen preparation without elaborating in detail every time. The formulation of the code name is explain in Figure 3.10. For instance, a specimen with three longitudinal reinforcement bars of 8 mm diameter using Araldite2047 adhesive to bond the fibre in the compression zone is coded as R3D8-AR47. The beams were also referred to using the same name during the test in the laboratory. This was one of

the first attempts in the world to identify the efficiency of strain transfer using different adhesives in the compression zone.

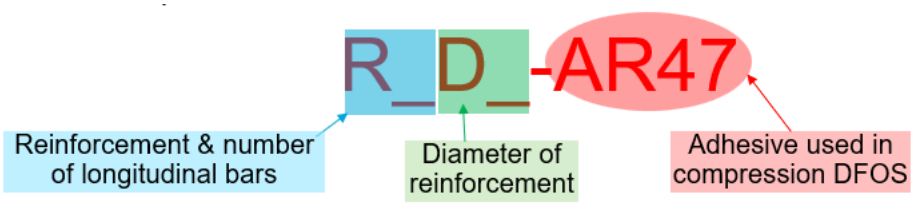

Figure 3.10: Nomenclature of the specimens

In Table 3.4, the specimens are arranged in order of increasing reinforcement ratios, which were deliberately selected to induce distinct crack patterns during the flexural tests. The specimen with the lowest reinforcement ratio exhibited relatively wide cracks with greater spacing, while the specimen with the highest ratio demonstrated the most closely spaced cracks among all four. To investigate the influence of adhesive stiffness under compression, each specimen was equipped with a different adhesive in the compression zone. In contrast, a single adhesive (DreiBond 8142) was consistently applied in the tension zone to facilitate accurate assessment of crack spacing and crack width. The use of a uniform adhesive in tension was essential to avoid confounding effects that could arise from varying adhesive properties, thereby ensuring clarity in interpreting crack behaviour.

No.	Specimen	Longitudinal reinforcement	Reinforcement ratio	Adhesive used (Compression zone)	Adhesive stiffness (E-modulus)
1	R3D8-AR47	3×Ø8 mm	0.598%	Araldite 2047-1 (Methacrylate)	830 MPa
2	R3D8-DB	4×Ø8 mm	0.797%	DreiBond 8142 (2C epoxy resin)	1130 MPa
3	R3D10-CN	3×Ø10 mm	0.94%	CN-E (Cyanoacrylate)	2400 MPa
4	R3D12-AR14	3×Ø12 mm	1.36%	Araldite 2014-1 (2C epoxy paste)	3100 MPa

Table 3.4: Specimen specifications

3.5. Installation of DFOS

Based on the shortcomings observed in the inverted T-girder test, a refined installation strategy was developed for the four-point bending beams. The objective was to obtain a more uniform and well-controlled bond between the fibre and the concrete surface, to minimise slack and handling-induced artefacts, and to enable a reliable quantitative assessment of strain transfer.

3.5.1. Fibre selection

For this experiment we used a polyimide–coated single-mode fibre from Thorlabs [29]. We chose it because the thin, stiff polyimide coating transfers strain well and can handle a wide temperature range (from $-65^{\circ}\mathrm{C}$ to $250^{\circ}\mathrm{C}$). Furthermore, past studies have shown that this type of fibre can give promising results for identifying crack peaks in concrete. The fibre has a standard $9/125\,\mu\mathrm{m}$ core/cladding and a $145 \pm 5\,\mu\mathrm{m}$ polyimide coating with good core–cladding concentricity.

3.5.2. Adhesive selection

The adhesive layer controls how strain is transferred from the concrete to the fibre. For surface-bonded DFOS, we therefore require a thin and durable bondline that provides consistent strain transfer and resists debonding under both tension and compression. Most published fibre–adhesive studies focus on tension; the ability of DFOS to capture compressive strains is comparatively under-reported. Because

the tension and compression sides experience different crack and contact mechanics, we evaluated four adhesives for the compression side and used a single adhesive for the tension side. The adhesives adopted in compression zone are listed in Table 3.4 for all specimens, the tension zone was bonded with Dreibond 8142 (two-component epoxy).

3.5.3. Refined DFOS Installation strategy

The main elements of the refined strategy were:

i) **Surface preparation:** The concrete surface in the constant moment region was carefully ground and cleaned along the entire fibre route. Laitance, loose particles and surface irregularities were removed, and particular attention was paid to filling or bypassing small voids to reduce the likelihood of local debonding. The surface was then degreased with solvent wipes immediately prior to bonding.

ii) **Fibre type and routing:** A polyimide-coated single-mode fibre was used for the beam tests, chosen for its stiff coating and good strain-transfer characteristics. The fibre was routed in two horizontal laps in the tension zone and two laps in the compression zone along the constant moment region, providing redundant measurements in each zone. Sharp bends and abrupt changes in direction were avoided to reduce local stress concentrations and potential debonding. The optical fibre was laid along the prepared path and temporarily secured at one end with Kapton tape. The fibre was then aligned by hand to remove visible slack while avoiding any sharp bends.

iii) **Fibre pre-tensioning:** In the tension region, the fibre was aligned and the free end of the fibre was gently tightened by hand to remove slack and taped down with Kapton tape. In the compression region, the free end of the fibre was connected to a 36 g dead weight routed over a small pulley, as shown in Figure 3.11. This provided a slight, constant pretension during bonding so that, under compressive loading, the fibre remains engaged instead of forming local buckles or debonding. The weight to be suspended has to be chosen carefully (through trial and error), so as to not damage the fragile glass core structure before the test.

Figure 3.11: Pretension applied to the fibre in the compression zone

iv) **Adhesive bondline control:** To obtain a thin and uniform adhesive layer, two 0.5 mm stainless steel plates were used as applicators. The adhesive was applied by touching one plate to the

concrete surface and sliding the second plate, pre-wetted with adhesive, along the fibre path (See Figure 3.12. This produced an approximately uniform bondline thickness of 0.5 mm.

Figure 3.12: Application of adhesive using sliding plate method

To minimise strain losses through the adhesive layer, the fibre was kept in direct contact with the concrete surface along its length. Adhesive was applied to form small fillets alongside and over the fibre, while avoiding trapping adhesive directly beneath the fibre. This ensured intimate fibre–concrete contact and consistent strain transfer. The bonded length was left undisturbed and allowed to cure in accordance with the manufacturer's technical data sheet for the adhesive used (ambient temperature and minimum cure time).

This refined installation strategy, together with the controlled four-point bending configuration, forms the basis for the strain-transfer analysis presented in the following sections. By comparing DFOS strains with strain gauge measurements in both tension and compression zones, an effective strain-transfer efficiency factor is derived for the surface-bonded DFOS configuration used in these beams.

3.6. Instrumentation and Measurement Setup

In the experimental campaign, a combination of measurement techniques were employed to capture different structural responses and to ensure reliable data for the validation of the DFOS performance. Each technique was selected based on its ability to measure a specific parameter of interest, such as strain, crack width, or deflection, under controlled loading conditions. The sensors used in the test were initially calibrated before starting the test. This section describes the complete measurement system, including the distributed fibre optic sensors, strain gauges, digital image correlation (DIC), and laser displacement sensors, together with their positioning, configuration, and data acquisition approach.

(a) Distributed Fibre Optic Sensors

DFOS served as the main sensing technique for this study. The primary objective of using DFOS in this study was to obtain a continuous strain profile along the beam and to monitor localized cracking and deformation patterns that cannot be captured by discrete sensors. As explained before, DFOS system operates based on optical frequency domain reflectometry (OFDR), which measures backscattered light along the fibre to derive local strain and temperature with millimetre-scale spatial resolution. Because duration of the test was short, we treated ambient temperature as effectively constant and did not consider temperature-induced strain peaks in the DFOS data.

A polyimide-coated single-mode fibre (Figure 3.13) was used. The key specifications are listed in Table 3.5. This fibre was selected because previous studies show that, when surface-bonded to concrete, the polyimide-coated fibre exhibits negligible interlayer slip and a short strain-transfer (mobilization) length, allowing precise strain measurement with DFOS [4], [59], [60]. A brief overview of coating properties and is provided in [29].

Figure 3.13: Polyimide-coated fibre structure [29]

Parameter	**Specification**
Coating Material	Polyimide
fibre Type	Single Mode (SM1550P)
Coating Diameter	145 $\pm$ 5 μm
Cladding Diameter	125 μm
Core Diameter	9 μm
Operating Wavelength	1310-1550 nm
Attenuation	≤ 0.7 dB/km
Color	Yellow
Manufacturer	Thorlabs

Table 3.5: Coating materials and fibre specifications.

The distributed fibre optic sensor (DFOS) was installed along both the compression and tension zones of the beam in two continuous loops, as shown in Figure 3.14. The primary objective was to measure the strain distribution over a 120 mm region at midspan, aligned parallel to the strain gauge (SG) mounted at the beam's center.

For each loading step, the average strain was computed over the 120 mm gauge length on both the top and bottom laps of the fibre in the respective compression and tension zones. The two readings from each zone (top and bottom laps) were then averaged to obtain a representative strain value for the compression and tension regions. These averaged DFOS strains were subsequently compared with the corresponding strain gauge measurements (refer equation 3.1).

After cracking, the concrete strain at the crack location theoretically approaches infinity, rendering direct DFOS strain measurements meaningless in the post-cracking stage. Consequently, the focus of post-cracking analysis shifted to evaluating flexural crack widths in the tension zone, which were determined from DFOS data and compared against results obtained from the Digital Image Correlation (DIC) method.

$$\varepsilon_{\text{DFOS, region}} = \frac{1}{2}\left(\bar{\varepsilon}_{\text{top lap}} + \bar{\varepsilon}_{\text{bottom lap}}\right) \tag{3.1}$$

where $\bar{\varepsilon}_{\text{top lap}}$ and $\bar{\varepsilon}_{\text{bottom lap}}$ are the mean DFOS strains measured over the 120 mm gauge length in the top and bottom laps, respectively

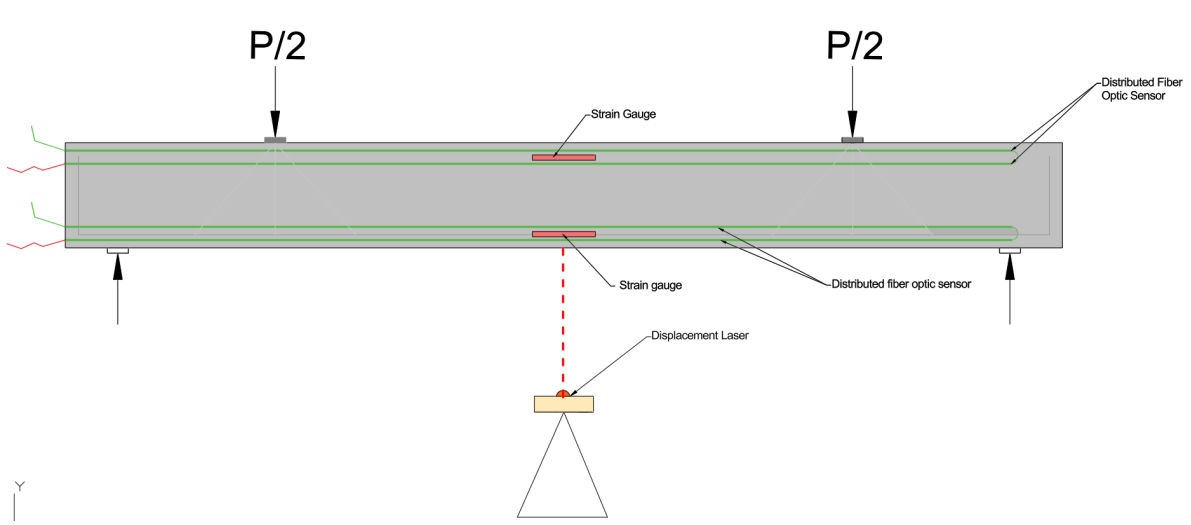

Figure 3.14: Position of sensors

(b) Electric resistance Strain Gauges

Conventional electrical-resistance wire strain gauges were used to measure surface strains on concrete. The PL-120-11 belongs to the P-series of polyester-backed wire strain gauges, which are specifically designed for use in concrete. The gauge has a nominal gauge length of 120 mm and a resistance of 120 Ω. The backing material is polyester resin, allowing good adhesion and compatibility with cementitious surfaces. The strain gauge exhibits a gauge factor of approximately 2.1 and can operate within a temperature range of $-20°\mathrm{C}$ to $+80°\mathrm{C}$. For this study, a three-wire quarter-bridge configuration was adopted to minimize the influence of temperature-dependent resistance variations in the lead wires [61].

A Compatible adhesive CN-E was used to bond the strain gauges on concrete surface. CN-E is a cyanoacrylate-based adhesive which is suitable for porous material like concrete.

The working principle of an electrical resistance strain gauge is based on the change in electrical resistance of a metallic conductor when it is subjected to mechanical strain. When the substrate deforms, the strain gauge undergoes a corresponding change in length and cross-sectional area, resulting in a measurable change in resistance. This relationship can be expressed as:

$$\frac{\Delta R}{R} = k\,\varepsilon \tag{3.2}$$

where R is the initial resistance, ΔR is the change in resistance due to strain, ε is the mechanical strain, and k is the gauge factor of the strain gauge. The strain is then determined by measuring the corresponding change in voltage through a Wheatstone bridge circuit.

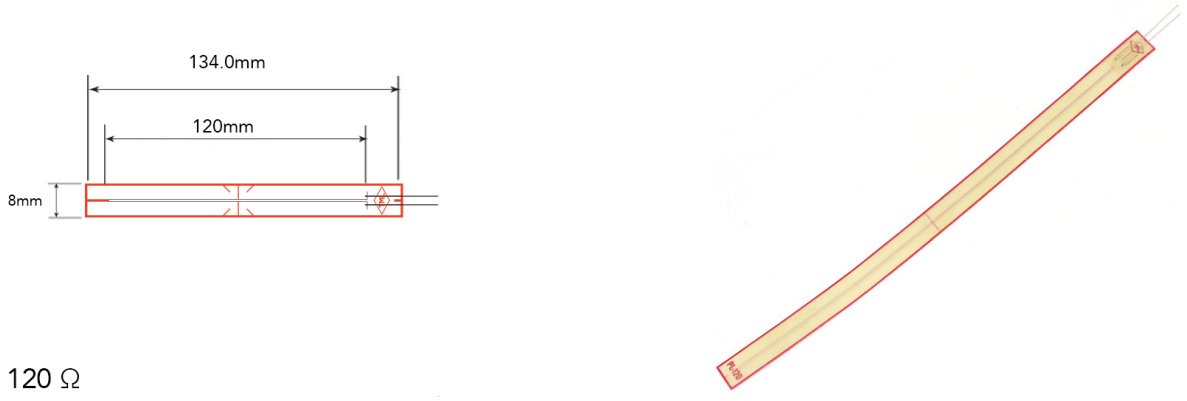

Figure 3.15: Strain gauge (PL-120-11)
[61]

(c) Digital Image Correlation (DIC)

Digital Image Correlation (DIC) was used to obtain full-field surface kinematics on the instrumented face of the concrete specimens. DIC tracks the motion of a random speckle pattern between a reference image and subsequent deformed images by correlating small image subsets.

Surface preparation: The specimen face was cleaned and coated with a matte white base layer. A black speckle pattern was then applied by spray to achieve an approximately uniform distribution (visually balanced black/white coverage), avoiding clusters and large blank areas.

Imaging setup: A stereo camera pair fitted with 35 mm lenses was used, with a strobe/flash light to stabilise exposure and reduce motion blur. The cameras were mounted on a rigid bar, focused on the region of interest, and aligned so that the image axes were parallel to the specimen axes.

Pre-test checks: Before loading, camera alignment and pattern quality were verified. A short “rigid-body” check was performed by acquiring two nominally identical images separated by 5-second interval. The correlation error between these images was inspected to confirm a low noise floor and stable illumination. The correlation error was bound out to be 0.02 mm. Hence, measurements below this error cannot be considered reliable.

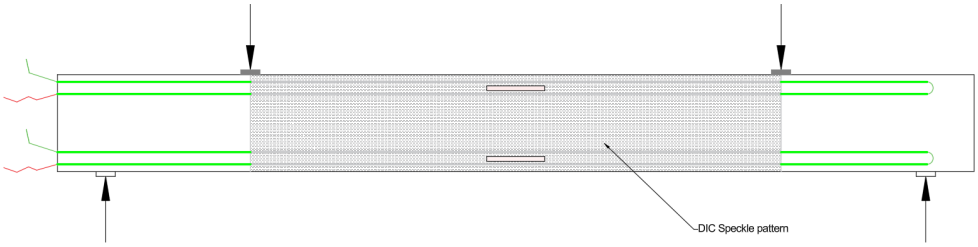

Figure 3.16: Representation of area painted with DIC Speckle pattern

(d) Displacement Laser Sensors

Laser triangulation displacement sensors were installed below the midspan of the beam to monitor vertical deflection throughout the test (Figure 3.14). The measurements were performed using an :FDRF603 Series Laser Triangulation Sensor” by Althen Sensors and Controls (Figure 3.17). These non-contact sensors operate on the principle of optical triangulation, allowing precise displacement measurements without any physical interaction with the specimen surface. The measurement range

of the sensor extends from 2 mm to 1250 mm, enabling accurate tracking of deflection over the entire loading history. The non-contact nature of the device eliminates mechanical wear and ensures that no additional force is applied to the structure during measurement [62].

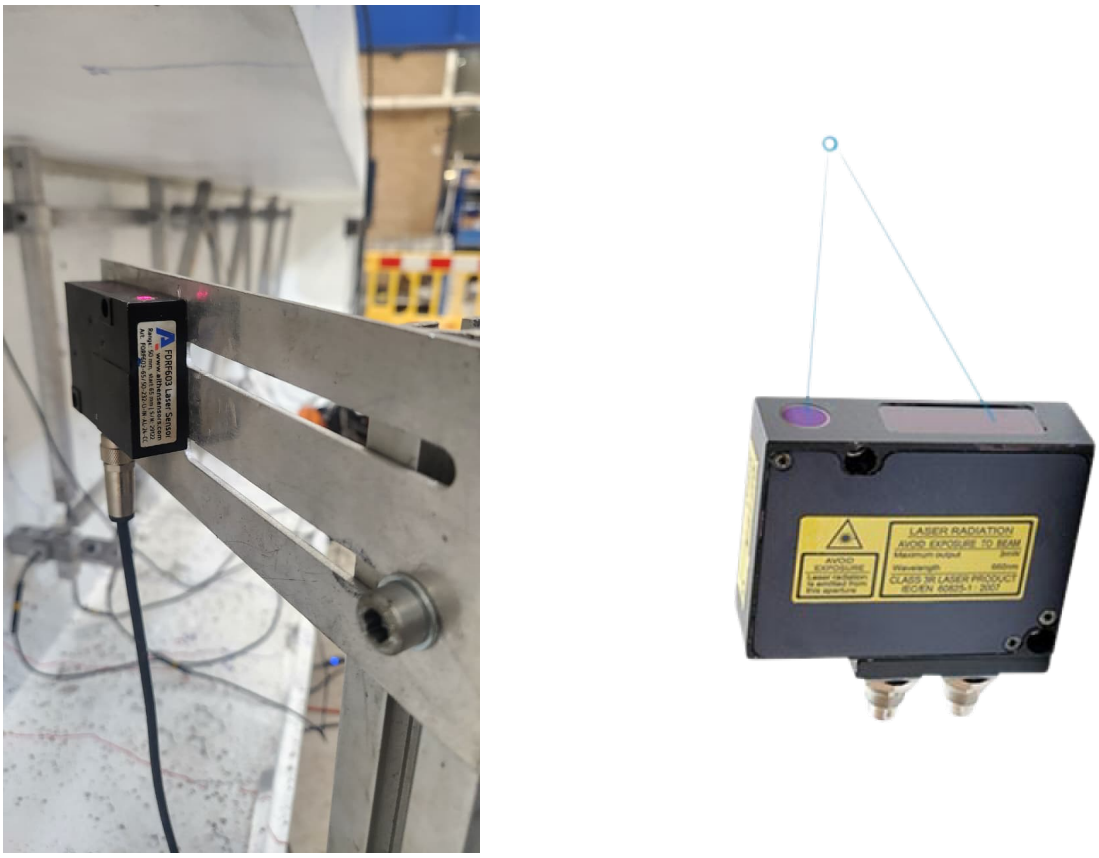

Figure 3.17: Laser triangulation sensor

3.7. Loading setup

In order to take account of the case of uniform strains and mulltiple well-spaced cracks in the Constant Moment Region (CMR), four-point bending test was carried out on the beams. The experimental setup consisted of a servo-controlled hydraulic jack with a loading capacity of 400 kN and a rigid steel loading frame that provided the necessary reaction support (Figure 3.18). The applied load from the jack was transmitted to the concrete beam through a steel spreader beam, which divided the load into two equal forces spaced 1100 mm apart, thereby generating a four-point bending configuration. This arrangement ensured a sufficient CMR in the central portion of the beam and shear spans on either side. The supports were placed 100 mm from each end of the beam, respectively. The beam was simply supported at its ends: one support was hinged to restrain vertical and horizontal movements, while the other incorporated roller bearings to permit longitudinal translation and prevent restraint-induced axial forces. During loading, the roller bearings allowed minor outward movement of the supports, enabling a smooth transfer of load and preventing unintended restraint stresses. The loading system was carefully aligned to ensure uniform load distribution and to minimize any eccentricities.

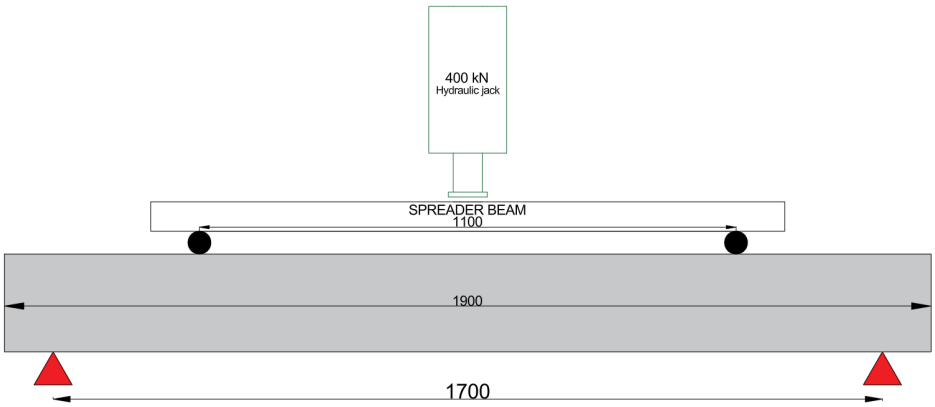

Figure 3.18: Sketch of loading setup (all measurements in mm)

3.7.1. Loading procedure

The beam specimens were tested under displacement-controlled loading using a servo-hydraulic jack operating at a constant rate of 0.1 mm/s. The applied load increased proportionally with the imposed vertical displacement of the actuator. During each test, the loading was paused at regular intervals to acquire synchronized measurements from all instrumentation systems. For most specimens, data were recorded at every 5 kN load increment. For specimen R3D12-AR14, data were acquired at every 10 kN increment because of its higher load-carrying capacity and to limit the total dataset size without compromising measurement resolution.

During each load hold, the DFOS interrogator (Luna ODiSI 6100) and the DIC system were triggered simultaneously to ensure temporal alignment between distributed strain data and surface image capture. This synchronization enabled direct correlation between DFOS strain peaks and crack openings identified in the DIC images at identical load steps. The load–displacement response was continuously monitored by the actuator's internal transducer and cross-checked with readings from the external load cell.

The test was terminated when visible surface cracks with widths exceeding 0.3 mm were observed using a crack width ruler (Figure 3.19), or when the DFOS system no longer provided usable data due to signal loss or fibre breakage caused by excessive deformation.

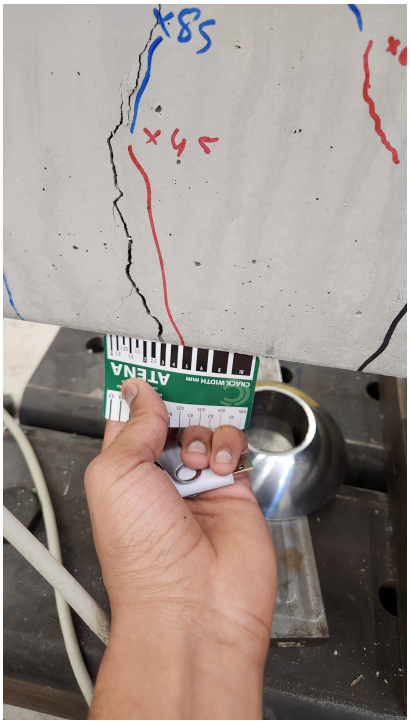

Figure 3.19: Measurement of crack widths using a crack width ruler

3.8. Data acquisition

Data from the measurement systems were continuously recorded throughout the test using the operational system called ”MP3”, and the data from DFOS was recorded using LUNA OdiSI series 6 interrogator. The MP3 system collected synchronized signals from the hydraulic actuator, strain gauges, and laser sensors, while the LUNA data logger was used to record distributed strain data from the optical fibres. The two systems were operated in parallel, with manual syncronization at each load step to ensure temporal alignment between the distributed strain data and the reference measurements.

3.8.1. MP3 Data Acquisition System

The MP3 data acquisition system was responsible for capturing signals from the conventional sensors used in the experiment, including the hydraulic jack load cell, strain gauges, and laser displacement sensors. The system provided real-time monitoring of load, strain, and displacement during each test. Prior to testing, all channels were individually calibrated to ensure accurate signal acquisition and consistency across measurements.

The parameters recorded through the MP3 system included:

- **Applied load (kN):** obtained from the actuator load cell integrated into the hydraulic jack,
- **Surface strain (με):** measured by foil strain gauges mounted in both the tension and compression zones, and
- **Midspan deflection (mm):** recorded using laser triangulation sensors positioned below the beam.

All readings were stored in a time-stamped format, allowing synchronization with the optical and image-based data obtained from the DFOS and DIC systems during post-processing.

3.9. Strain transfer analysis

Distributed Fibre Optic Sensors (DFOS) bonded to the surface of concrete do not measure the concrete strain directly. The optical signal is recorded in the glass core of the fibre, while the deformation of the concrete must be transmitted through intermediate layers such as adhesive, coating and cladding. Any

shear compliance, imperfect bonding, thickness variation or local slip within these layers attenuates the strain that reaches the fibre. As a result, the raw DFOS strain generally underestimates the true surface strain of the concrete. For surface-bonded fibres, this effect is more pronounced than for embedded fibres, because only part of the fibre perimeter is in direct contact with the substrate, while the rest is surrounded by adhesive and coatings.

The purpose of this section is to evaluate how effectively strain from the concrete surface is transmitted through the adhesive and coating to the fibre core of the distributed fibre optic sensor (DFOS). To quantify this effect in the present configuration, a *strain-transfer efficiency* (STE) is introduced. The STE provides a practical measure of how effectively strain in the concrete surface is transmitted to the fibre core for a given installation. It is defined as the ratio between the strain measured by the DFOS and the strain measured by a reference sensor bonded directly to the concrete surface, under conditions where the strain field can be considered uniform:

$$\mathrm{STE} = \frac{\varepsilon_{\mathrm{DFOS}}}{\varepsilon_{\mathrm{ref}}} * 100\%, \tag{3.3}$$

where $\varepsilon_{\mathrm{DFOS}}$ is the average DFOS strain over a short segment in the constant moment region and $\varepsilon_{\mathrm{ref}}$ is the corresponding strain measured by an electrical strain gauge at the same location. An STE of 100% would indicate perfect strain transfer, whereas values less than 100% reflect strain losses across the adhesive and coating layers.

3.9.1. Experimental setup for strain-transfer evaluation

For each beam specimen, electrical strain gauges were bonded directly to the concrete surface at selected positions along the constant moment region. The DFOS line was installed parallel to the strain gauges on the same face of the beam, ensuring minimal height difference between the two sensors. The comparison was limited to the uncracked stage of loading so that the strain field remained uniform along the constant moment region. DFOS measurements were acquired using the Luna ODiSI 6100 interrogator with a gauge pitch of 1.3 mm and a spatial resolution of approximately 10 mm. Strain-gauge data were synchronised with the DFOS readings through the data acquisition system.

To investigate the influence of adhesive stiffness and bondline properties, different adhesives were used in the compression zone of the four beams (e.g. Araldite 2047, Dreibond 8142, cyanoacrylate and Araldite 2014), while a stiff epoxy was consistently used in the tension zone. This allowed the effect of adhesive type on strain-transfer efficiency to be assessed separately in compression and tension.

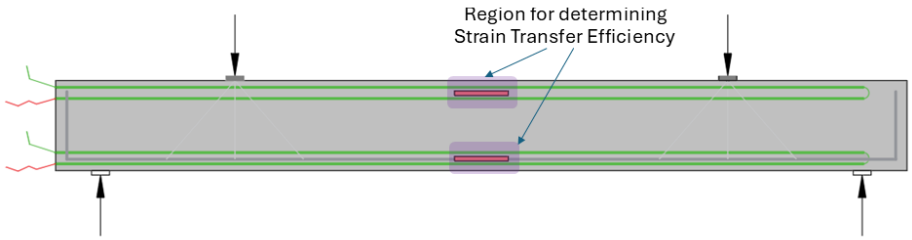

Figure 3.20: Region for identifying strain transfer between DFOS and strain gauges

3.9.2. Results: Strain transfer in compression

The strain-transfer behaviour in the compression zone was evaluated for all four beam specimens to assess the influence of adhesive stiffness on strain transmission from concrete to the DFOS. Each specimen was tested under identical four-point bending conditions, and the strain-gauge and DFOS readings near the top surface were compared and are presented below.

1. Strain transfer in Compression: Specimen 1 (R3D8-AR47)

Table 3.6: Compression-side DFOS vs strain-gauge strains and strain-transfer efficiency (STE) for specimen R3D8-AR47.

Load (kN)	DFOS strain (με)	Strain gauge (με)	STE (%)	Mean STE (%)
5	−11.4143	−26.6895	42.76	**43.67**
10	−25.1108	−55.8643	44.94	
15	−40.2979	−88.8984	45.33	
20	−56.6800	−125.9940	44.98	
25	−73.5900	−161.0080	45.70	
30	−93.1721	−210.5100	44.26	
35	−119.6418	−271.0690	44.13	
40	−147.0341	−337.6620	43.54	
45	−182.9905	−427.5700	42.79	
50	−218.0131	−505.4460	43.13	
55	−233.8279	−545.0000	42.90	
60	−246.4283	−580.5800	42.44	
65	−261.7823	−618.7190	42.31	
70	−275.3404	−653.4310	42.13	

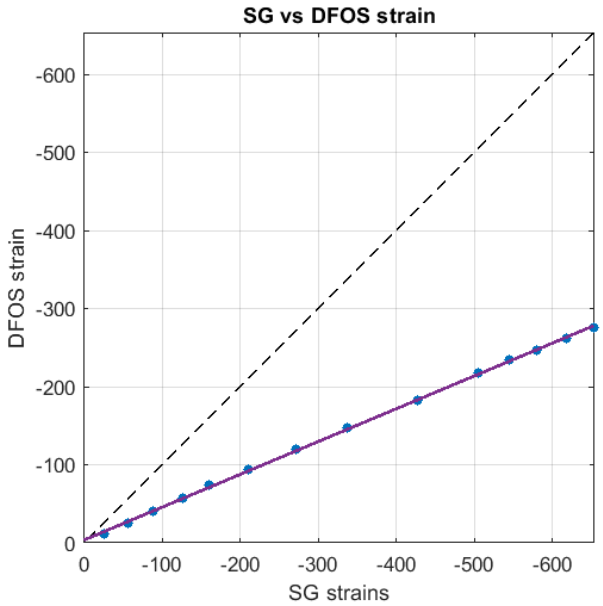

Figure 3.21: R3D8-AR47 Compressive strains (SG vs DFOS)

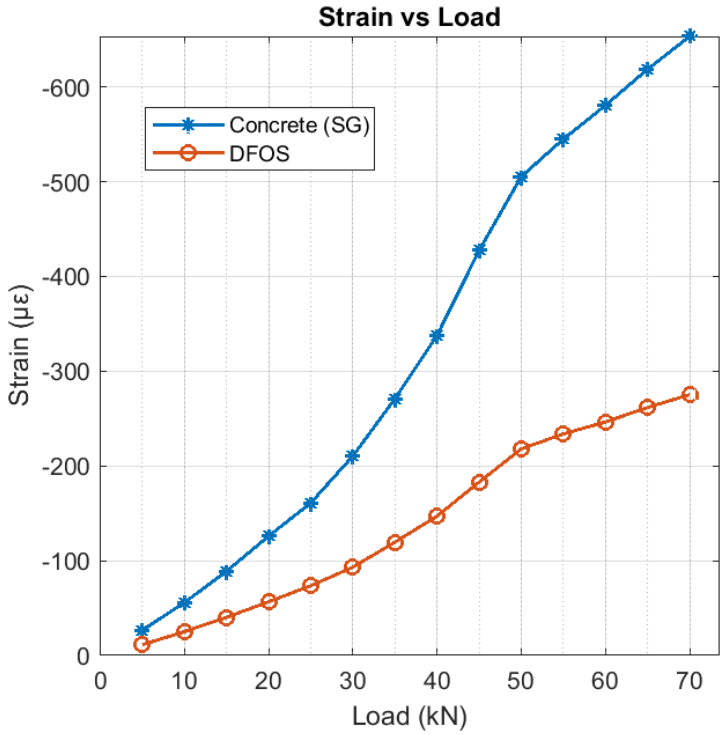

Figure 3.22: Strain vs Load plot for SG and DFOS (R3D8-AR47)

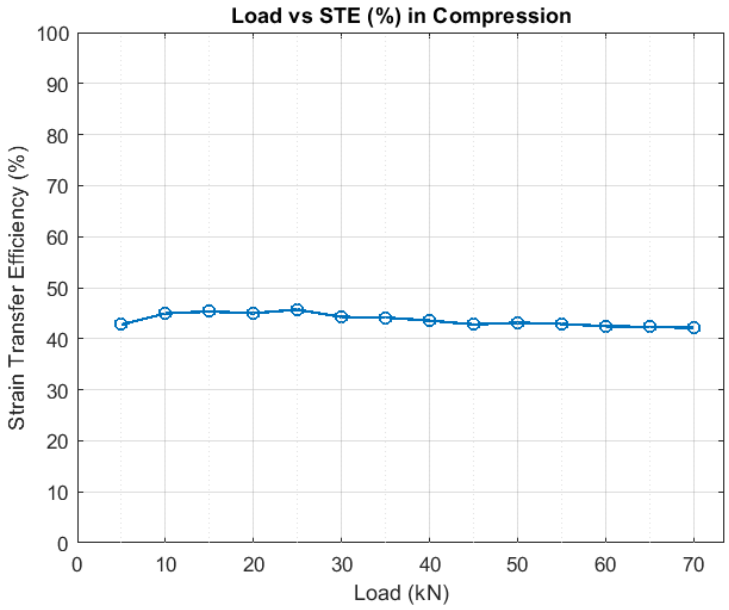

Figure 3.23: Strain transfer efficiency for all load steps (R3D8-AR47)

From the above plots, it can be seen that with gradual increase in load, the difference between the ε_{SG} and ε_{DFOS} increases. However, the strain transfer efficiency remains constant with the mean STE being = 43.67 %.

2. Strain transfer in Compression: Specimen 2 (R4D8-DB)

Table 3.7: Compression-side DFOS vs strain-gauge strains and strain-transfer efficiency (STE) for specimen R4D8-DB

Load (kN)	DFOS strain (με)	Strain gauge (με)	STE (%)	Mean STE (%)
5	−13.44	−31.129	43.18	**45.05**
10	−27.88	−64.038	43.53	
15	−43.24	−97.3108	44.43	
20	−54.75	−134.036	40.85	
25	−74.84	−166.38	44.98	
30	−94.16	−208.73	45.11	
35	−115.97	−250.91	46.22	
40	−146.28	−309.59	47.24	
45	−185.71	−401.62	46.24	
50	−228.63	−500.67	45.66	
55	−256.21	−559	45.83	
60	−283.52	−616.49	45.98	
65	−303.13	−661.15	45.84	
70	−318.64	−698.58	45.61	

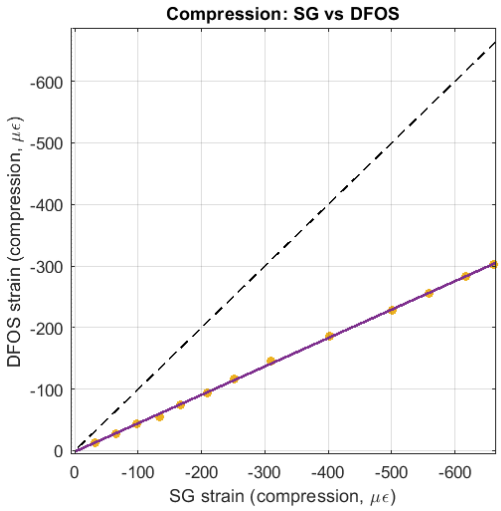

Figure 3.24: R4D8-DB Compressive strains (SG vs DFOS)

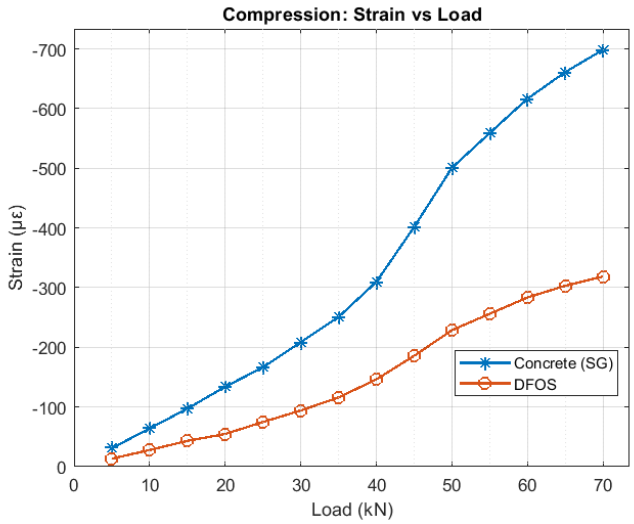

Figure 3.25: Strain vs Load plot for SG and DFOS (R4D8-DB)

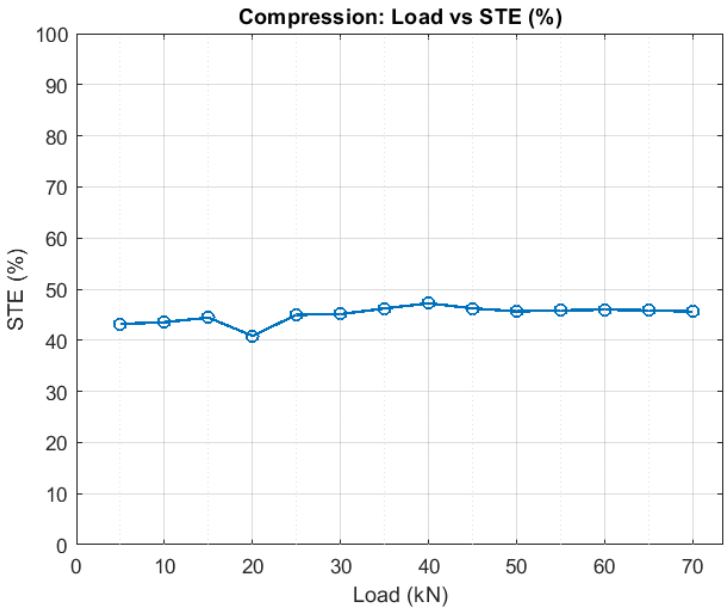

Figure 3.26: Strain transfer efficiency for all load steps (R4D8-DB)

A replicating trend from the previous specimen can be seen. With gradual increase in load, the difference between the $\varepsilon_{\mathrm{SG}}$ and $\varepsilon_{\mathrm{DFOS}}$ increases. However, the strain transfer efficiency remains constant with the mean STE being = 45.05 %.

3. Strain transfer in Compression: Specimen 3 (R3D10-CN)
   In this specimen, the data quality was insufficient to support reliable strain transfer analysis (see Figure 3.27). Consequently, the results obtained from this specimen have been excluded from further evaluation.

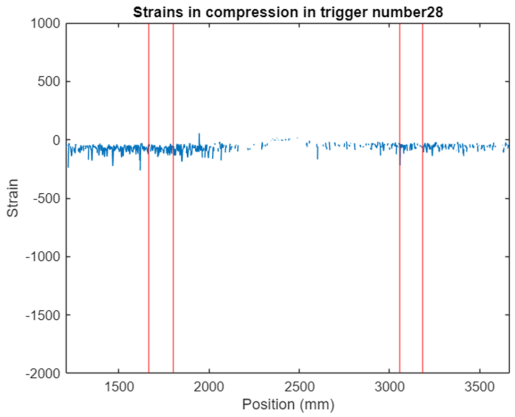

Figure 3.27: Strain profile for Specimen 3 (R3D10-CN)

4. Strain transfer in Compression: Specimen 4 (R3D12-AR14)

Table 3.8: Compression-side DFOS vs strain-gauge strains and strain-transfer efficiency (STE) for specimen R3D12-AR14.

Load (kN)	DFOS strain (με)	Strain gauge (με)	STE (%)	Mean STE (%)
5	−10.36	−19.9451	51.942	
10	−22.003	−41.651	52.828	
20	−46.317	−88.094	52.576	**53.740**
30	−71.809	−137.244	52.322	
40	−101.544	−191.752	52.956	
50	−121.653	−222.41	54.697	
60	−133.287	−226.455	58.858	

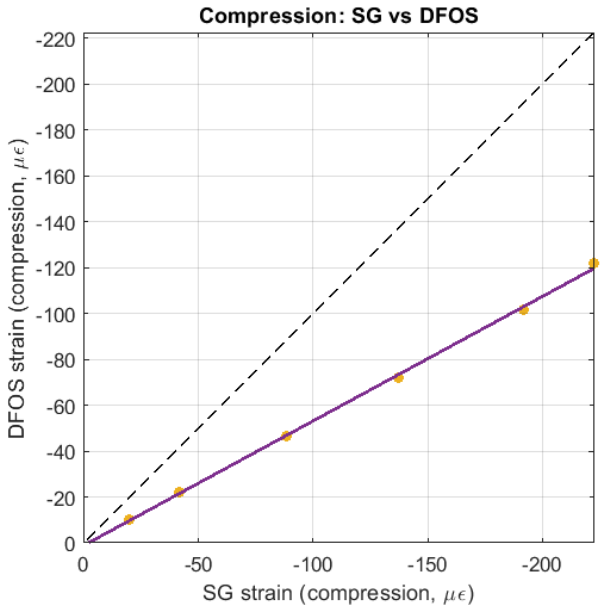

Figure 3.28: R3D12-AR14 Compressive strains(SG vs DFOS)

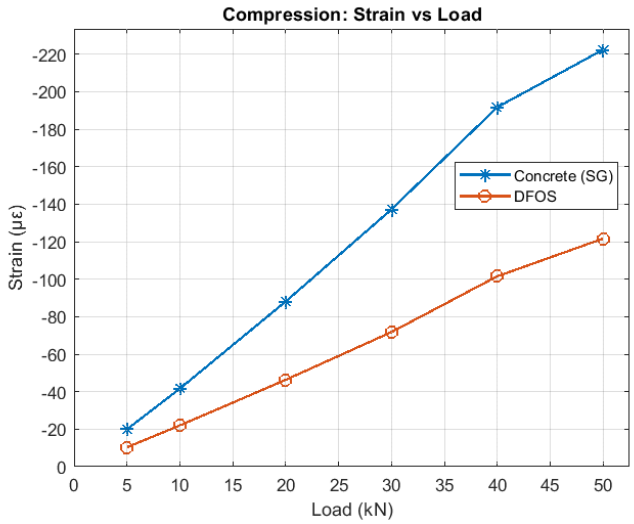

Figure 3.29: Strain vs Load plot for SG and DFOS (R3D12-AR14)

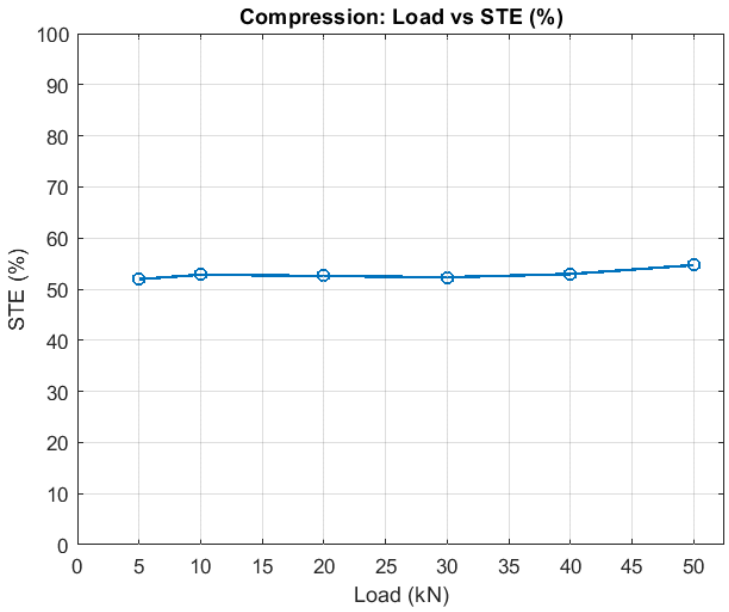

Figure 3.30: Strain transfer efficiency for all load steps (R3D12-AR14)

Since the load stages for this specimen were spaced at 10 kN each, the number of points under consideration for Strain transfer analysis are comparatively low. From the above plots, it can be seen that with gradual increase in load, the difference between the $\varepsilon_{\mathrm{SG}}$ and $\varepsilon_{\mathrm{DFOS}}$ increases. However, the strain transfer efficiency remains constant with the mean STE being = 53.74 %.

3.9.2.1. Summary of findings: Strain transfer in Compression

The strain-transfer behaviour in the compression zone was evaluated for all four beam specimens by comparing DFOS and strain-gauge readings at the top surface of the constant moment region. For each specimen, the DFOS strain showed an almost linear relationship with the strain-gauge measurements over the considered load range. However, the magnitude of the DFOS strain was consistently lower than the strain-gauge strain, resulting in STE values of approximately 0.40–0.50 depending on the adhesive used (see Tables 3.6–3.8).

Specimens bonded with stiffer epoxy adhesives generally exhibited slightly higher STE, reflecting more

efficient strain transfer, whereas more compliant or thicker bondlines led to marginally lower STE values. However, fibre bonded using cyanoacrylate adhesive resulted in poor measurements and showed no plausible data in compression. Although cyanoacrylate adhesives are frequently used to bond optic fibre in tension zone, a detailed study is required to assess its performance in compression critical zone.

Nevertheless, the variation between adhesives was relatively modest compared to the overall loss of strain, indicating that the presence of the pre-tension adhesive and coating layers itself has a dominant influence on strain transfer in compression. Overall, the results suggest that, for the surface-bonded DFOS configuration used in the compression zone, only about 40–50% of the concrete surface strain is transmitted to the fibre core in the uncracked range. This implies that DFOS compression strains must be corrected using an appropriate strain-transfer factor if they are to be interpreted as concrete surface strains.

3.9.3. Result: Strain transfer in Tension

1. Strain transfer in Tension (Specimen 1)

Table 3.9: Tension-side DFOS vs strain-gauge strains and strain-transfer efficiency (STE) for specimen R3D8-AR47.

Load (kN)	DFOS strain (με)	Strain gauge (με)	STE (%)	Mean STE (%)
5	10.293	23.954	42.97	
10	22.8735	50.944	44.89	
15	36.76	82.513	44.55	
20	50.5018	114.49	44.10	**43.89**
25	60.434	144.429	41.84	
30	51.992	122.48	42.44	
35	46.4835	100.126	46.42	

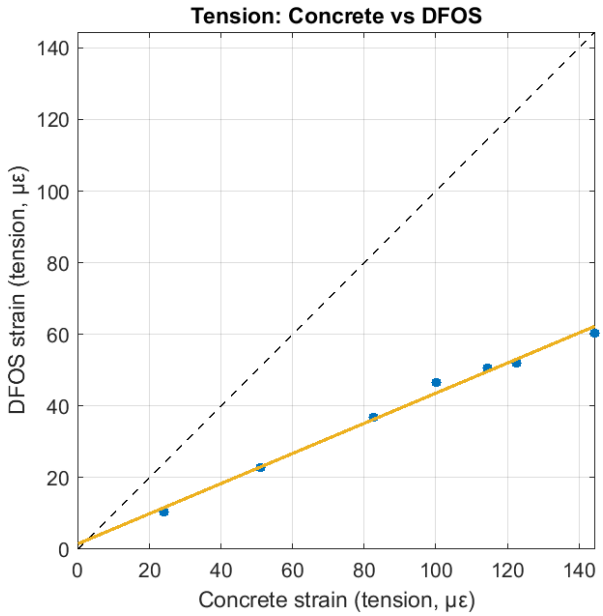

Figure 3.31: Strain transfer efficiency for all load steps (R3D8-AR47)

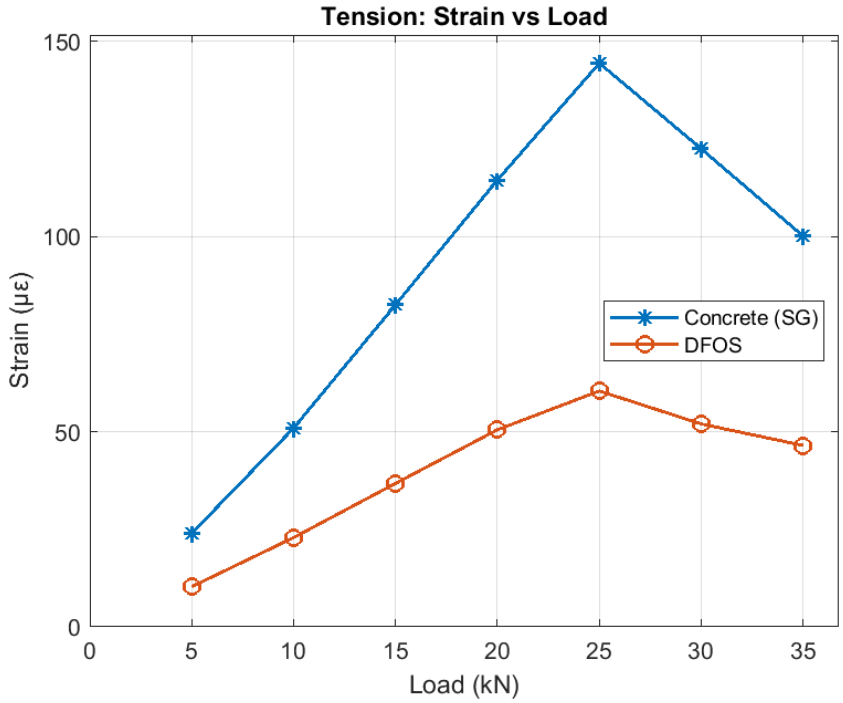

Figure 3.32: Strain transfer efficiency for all load steps (R3D8-AR47)

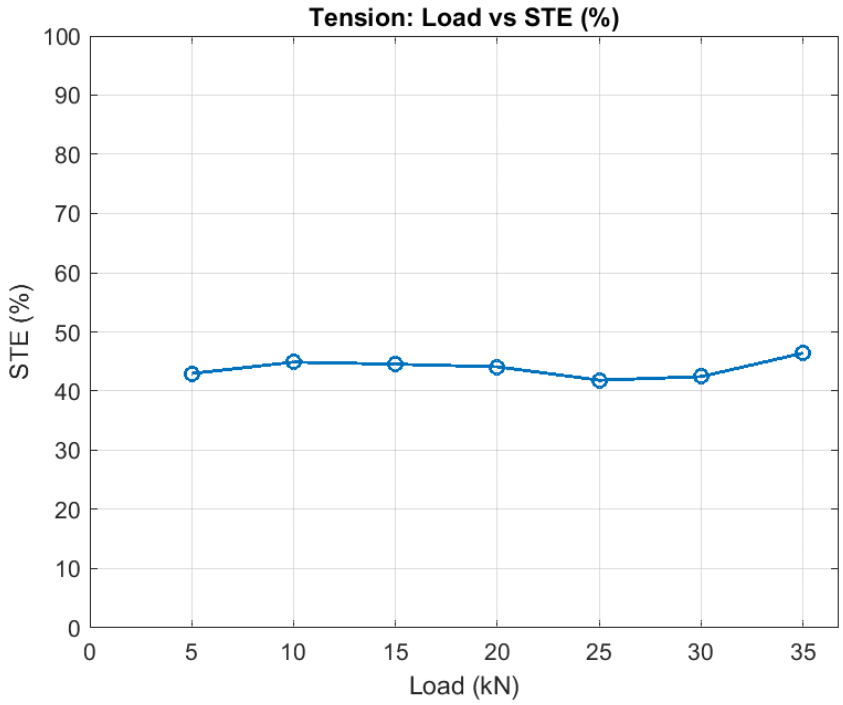

Figure 3.33: Strain transfer efficiency for all load steps (R3D8-AR47)

2. Strain transfer in Tension (Specimen 2)

Table 3.10: Tension-side DFOS vs strain-gauge strains and strain-transfer efficiency (STE) for specimen R4D8-DB.

Load (kN)	DFOS strain (με)	Strain gauge (με)	STE (%)	Mean STE (%)
5	14.398	22.784	63.15	**51.194**
10	28.733	53.245	53.963	
215	44.25	82.82	53.42	
20	56.98	105.74	53.88	
25	72.651	143.77	50.53	
30	87.256	190.85	45.719	
35	121.751	265.357	45.88	
40	156.906	364.98	42.99	

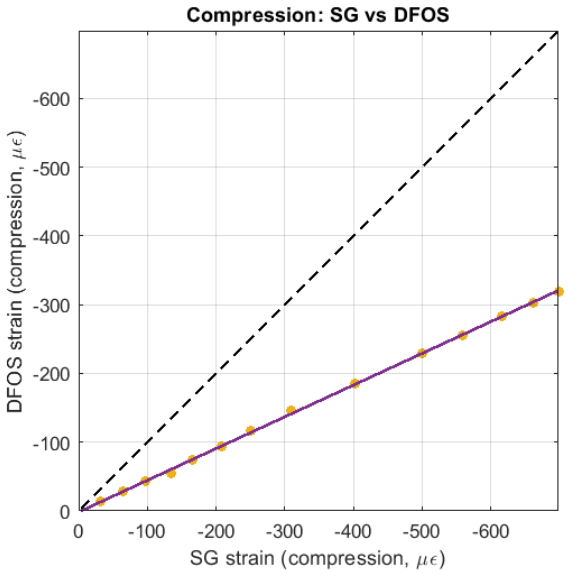

Figure 3.34: R4D8-DB Compressive strains(SG vs DFOS)

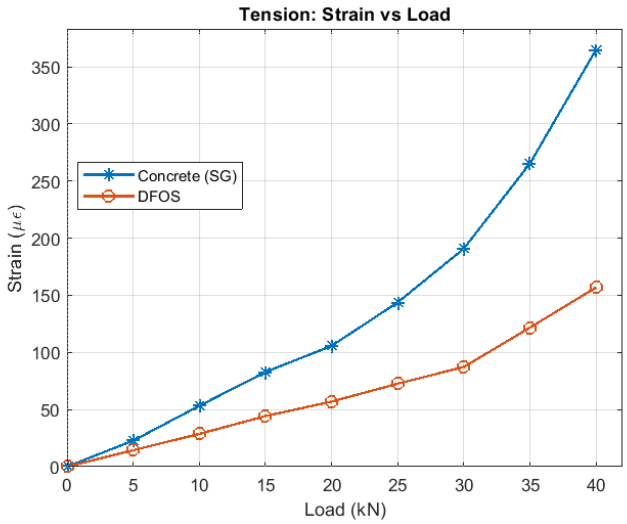

Figure 3.35: Strain vs Load plot for SG and DFOS (R4D8-DB)

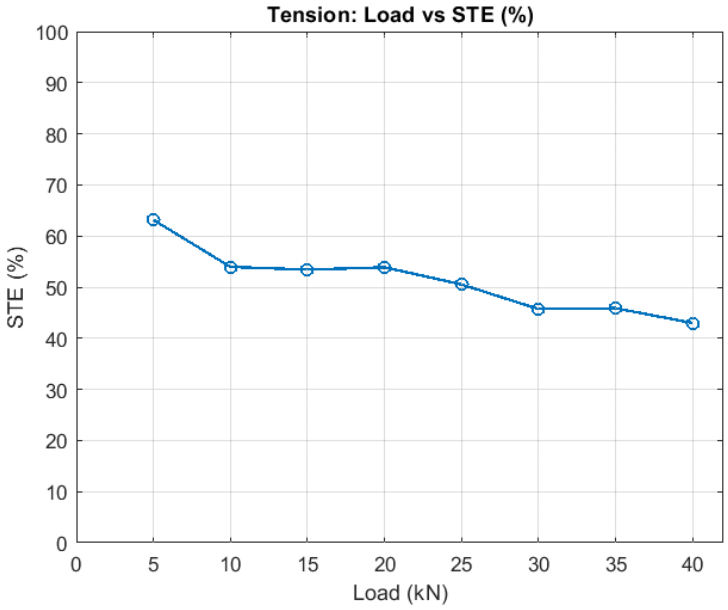

Figure 3.36: Strain transfer efficiency for all load steps (R4D8-DB)

3. Strain transfer in Tension (Specimen 3)
   From the two laps located in the tension zone, one was inadvertently damaged prior to testing. As a result, strain transfer measurements in tension could not be acquired for this specimen.

4. Strain transfer in Tension (Specimen 4)

Table 3.11: Tension-side DFOS vs strain-gauge strains and strain-transfer efficiency (STE) for specimen R3D12-AR14.

Load (kN)	DFOS strain (με)	Strain gauge (με)	STE (%)	Mean STE (%)
5	11.137	23.809	46.77	**43.223**
10	23.855	53.093	44.93	
20	50.36	114.05	44.16	
30	82.785	215.368	38.439	
40	175.19	419.08	41.804	

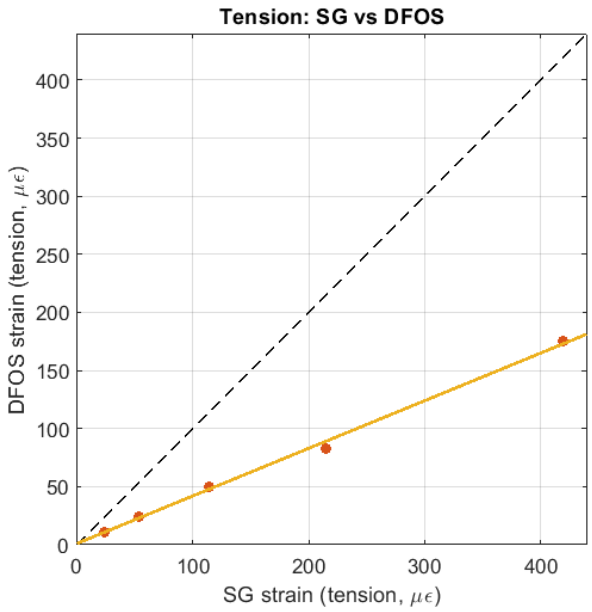

Figure 3.37: R4D8-DB Compressive strains(SG vs DFOS)

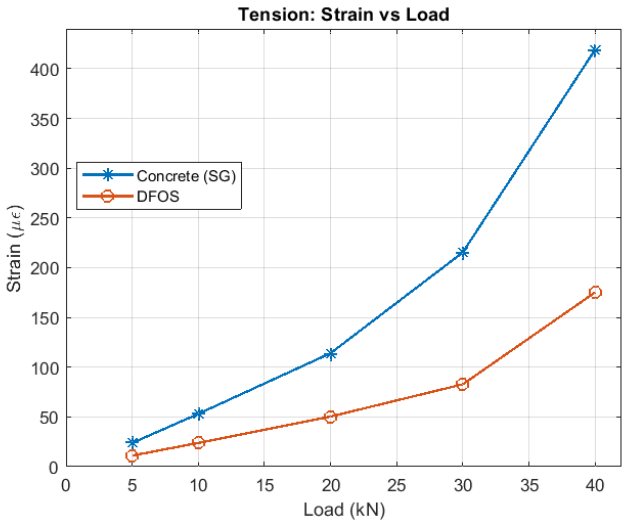

Figure 3.38: Strain vs Load plot for SG and DFOS (R4D8-DB)

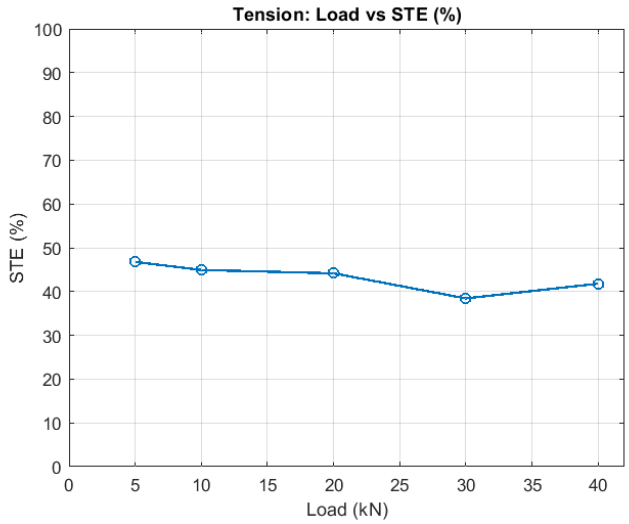

Figure 3.39: Strain transfer efficiency for all load steps (R3D12-AR14)

3.9.3.1. Summary of findings: Strain transfer in tension

The strain-transfer efficiency in the tension zone was evaluated in a similar manner using the DFOS and strain-gauge measurements at the bottom surface of the beams. Due to accidental damage to one of the tension-side fibre laps, reliable STE values could only be obtained for a subset of the specimens. For the beams with intact DFOS in tension, the relationship between DFOS strain and strain-gauge strain was again approximately linear in the uncracked loading range.

As in compression, the DFOS strains in tension were systematically lower than the strain-gauge values. The resulting STE values were of the same order as in compression, typically around 0.40–0.45 (see Table 3.9-3.11). Within the accuracy of the measurements and the scatter between load steps, no strong systematic difference was observed between STE in tension and STE in compression for the present configuration.

These findings indicate that, for the tested beams and installation strategy, a single effective strain-transfer efficiency factor can be used as a first approximation to relate DFOS strains to concrete surface strains in both tension and compression zones in the uncracked range.

3.9.4. Discussion and implications for subsequent analysis

The experimental work in this chapter has shown that the performance of surface-bonded DFOS on reinforced concrete members depends not only on the sensing technology itself, but critically on the installation strategy and strain-transfer behaviour.

The inverted T-girder test, installed using generic manufacturer guidelines and literature examples, demonstrated that such recommendations are not sufficient to guarantee a uniform and reliable bond. Non-uniform adhesive thickness, local fibre slack and debonding at surface imperfections led to noisy or attenuated strain readings and limited the suitability of the data for quantitative analysis. This pilot application highlighted the need for a more explicit and experimentally informed installation strategy for surface-bonded DFOS on concrete, rather than reliance on general qualitative guidance.

In response, a refined installation strategy was developed and implemented in the four-point bending beams. Key elements of this strategy included rigorous and continuous surface preparation along the fibre route, careful control of bondline thickness, avoidance of sharp bends in the fibre routing, and standardised fibre pretension and anchorage. Initial DFOS scans and visual inspection confirmed that this approach produced a more consistent bond and fewer regions with noisy or missing data than in the T-girder test, providing a more robust basis for quantitative assessment.

Despite these improvements, the strain-transfer analysis in the four-point bending beams showed that surface-bonded DFOS still underestimates the true concrete surface strain. For the configuration stud-

ied in this thesis, the strain-transfer efficiency was found to be of the order of 40–50% in both compression and tension, with only a modest dependence on adhesive type within the tested range. This implies that DFOS strains cannot be interpreted directly as concrete surface strains, even under carefully controlled installation, and that an experimentally calibrated correction factor is required.

The relatively low strain-transfer efficiency observed in the experiments can be explained by the fundamental difference between the strain-transfer mechanisms of conventional strain gauges and surface-bonded fibre optic sensors. A strain gauge measures deformation through a metallic grid that is uniformly bonded to the concrete surface using a very thin adhesive layer. The entire active length of the sensitive wire deforms together with the substrate, which results in an almost direct representation of the surface strain. In contrast, a surface-bonded DFOS consists of a circular glass core surrounded by protective coatings and bonded to the surface only along a narrow line of contact. The strain is transmitted through a sequence of relatively compliant layers, namely, concrete, adhesive, coating, and the glass core, by shear deformation at each interface. Because only one side of the fibre is in contact with the concrete and the intermediate layers can deform independently, a portion of the surface strain is dissipated within the adhesive and coating before reaching the fibre core. This results in a measured DFOS strain that is smaller than the true surface strain, leading to a lower strain-transfer efficiency for surface-bonded configurations. Embedded fibres, which are fully surrounded by concrete and transfer strain uniformly around their circumference, generally exhibit much higher efficiencies assumed as STE $\approx$ 90–100% by some optic fibre manufacturers [63]. The lower STE measured in this study is therefore consistent with the expected behaviour of surface-mounted DFOS systems.

In the context of the research questions, these findings address Sub-question 1 by demonstrating that generic installation guidelines must be complemented with clearly defined procedures for surface preparation, adhesive application, fibre routing and pretension to achieve reliable strain transfer. They also address Sub-question 2 by providing an experimentally derived strain-transfer efficiency factor that relates DFOS-measured strains to concrete surface strains for the specific surface-bonded configuration used in this study.

In the subsequent chapters, this factor and the refined installation strategy are used when interpreting DFOS strain profiles. In particular, they form the basis for:

- converting DFOS strains into estimates of concrete strain when assessing global flexural behaviour; and
- evaluating the accuracy and reliability of DFOS-based crack detection and crack-width estimation in reinforced concrete members, which is the focus of Chapter 4.

4

Assessment of DFOS-derived crack widths

4.1. Introduction and objectives

In the previous chapters, the potential and limitations of Distributed Fibre Optic Sensing (DFOS) for strain monitoring in concrete structures were examined. Chapter 2 summarised existing approaches for DFOS-based crack-width estimation and highlighted that, although several procedures have been proposed, their reliability has not yet been systematically validated for surface-bonded sensors on reinforced concrete members. Chapter 3 then described an experimental programme in which surface-bonded DFOS were installed on an inverted T-girder and on four-point bending beams. From these tests, a refined installation strategy and a calibrated strain-transfer efficiency were obtained, providing the basis for quantitative interpretation of DFOS strain measurements.

Building on this foundation, the present chapter evaluates how reliably DFOS can be used to detect and quantify crack widths in reinforced concrete members. The assessment is carried out in two steps. First, a qualitative analysis on the inverted T-girder investigates the capability of DFOS to detect and localise cracks by comparing distributed strain peaks with crack maps obtained from Digital Image Correlation (DIC). Second, a quantitative study on four-point bending beams evaluates DFOS-derived crack widths against DIC measurements at matched load stages, using the calibrated strain-transfer relationship from Chapter 3. In addition, the influence of missing data around crack-induced strain peaks is quantified through an Le/L analysis, in which the accuracy of DFOS-based crack widths is related to the fraction of the peak that is not captured by the sensor.

The objective of this chapter is therefore to answer Sub-question 3:

> *How reliable are crack widths obtained from Distributed Fibre Optic Sensing for reinforced concrete members?*

By combining qualitative crack detection, quantitative crack-width comparison, and a systematic investigation of missing-data effects, this chapter provides a practical basis for judging when DFOS can be relied upon for crack-width assessment in existing concrete structures and under which conditions its use becomes critical.

4.2. Qualitative crack detection using DFOS

Before assessing the accuracy of DFOS-derived crack widths, it is first necessary to verify whether surface-bonded DFOS can reliably detect and localise cracks along a reinforced concrete member. For this purpose, the inverted T-girder test described in Chapter 3 is revisited here with a focus on qualitative crack detection. The DFOS strain profiles obtained on the web of the girder are compared with crack patterns from Digital Image Correlation (DIC), which serves as a full-field reference.

The following figures illustrate the progression of crack formation in the tested specimen under increas-

ing load levels, as captured by Distributed Fibre Optic Sensing (DFOS) and Digital Image Correlation (DIC). At locations with steep strain gradients (for example, cracks), DFOS measurements often suffer data loss and the strain peaks appear as missing values. To reconstruct short gaps in these profiles, we first flagged obvious spike artefacts as missing so they would not bias the reconstruction. We then filled only short gaps, leaving longer outages untouched, using a shape-preserving cubic interpolation along the fibre axis that follows the local trend and peak heights. This avoids the overshoot typical of smooth spline fits, so crack-induced strain peaks retain their amplitude and position. Missing values at the very start or end of the profile were left unfilled as a conservative boundary choice.

1. Crack initiation at 450 kN load
   At 450 kN load, the first visible diagonal cracks through DIC were observed near the mid-shear span. Corresponding DFOS strain peaks emerged, confirming the onset of shear cracking. Figure 4.1a shows the overall crack distribution across the specimen, while subfigures 4.1b-4.1e highlight the strain peaks observed locally at respective laps of the fibre bonded to the specimen.

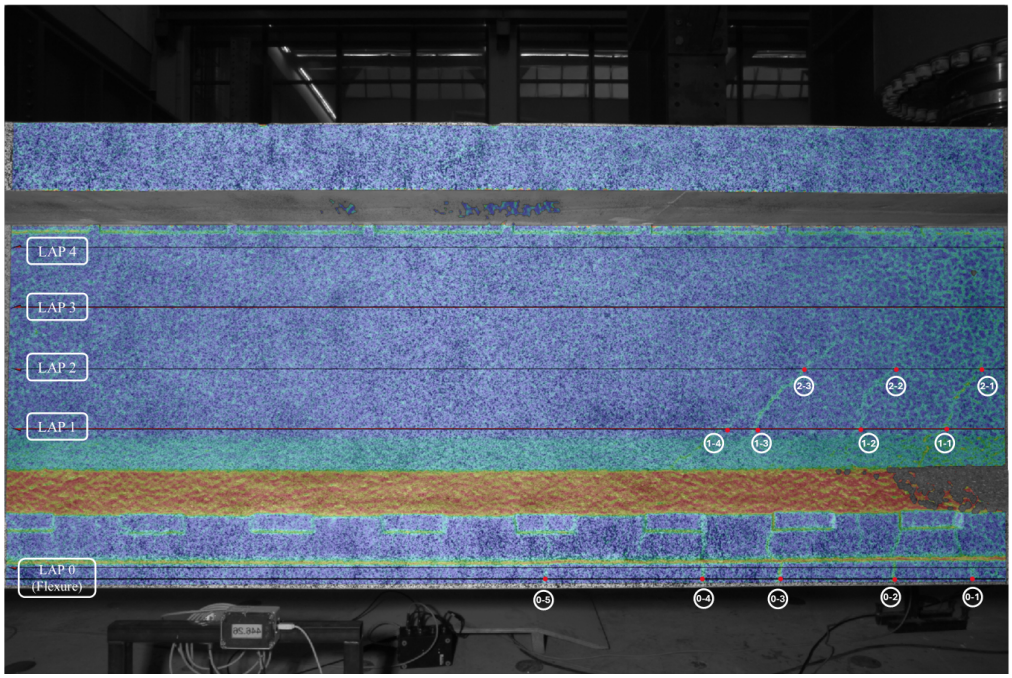

(a) Overall crack pattern at 450 kN.

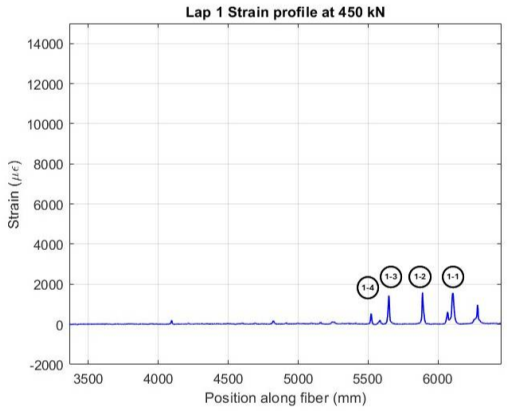

(b) Strain profile at Lap 1 .

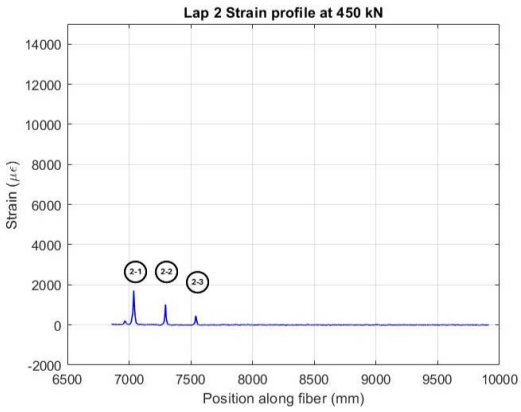

(c) Strain profile at Lap 2.

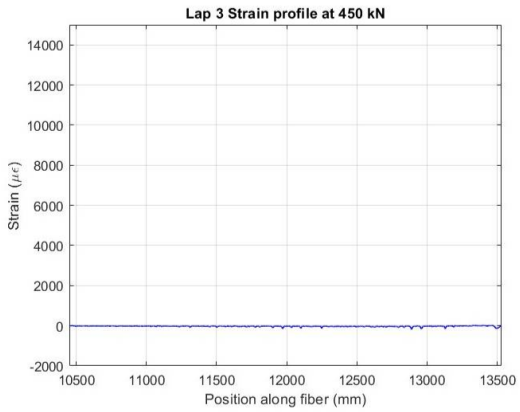

(d) Strain profile at Lap 3.

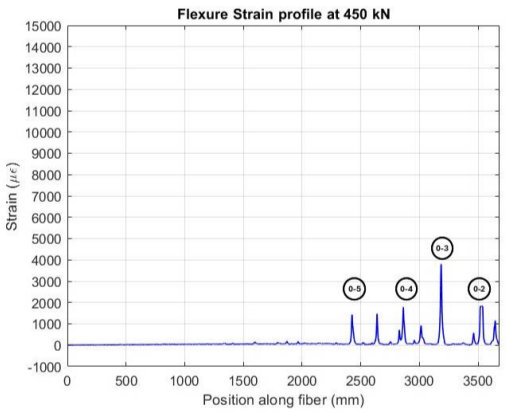

(e) Strain profile at Lap 0: Flexure.

Figure 4.1: Crack development at 450 kN load: (a) overall crack pattern and (b–e) DFOS strain profile at different laps.

2. Crack development at 600 kN Load

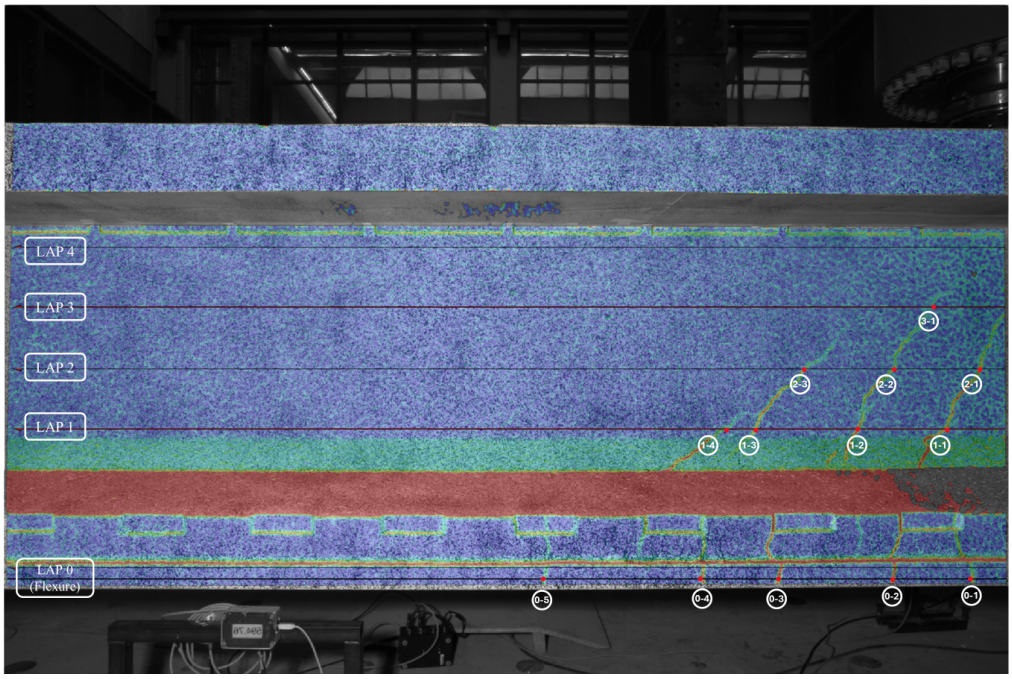

(a) Overall crack pattern at 600 kN.

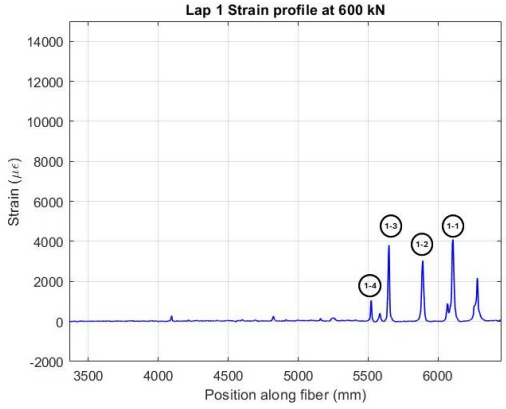

(b) Strain profile at Lap 1.

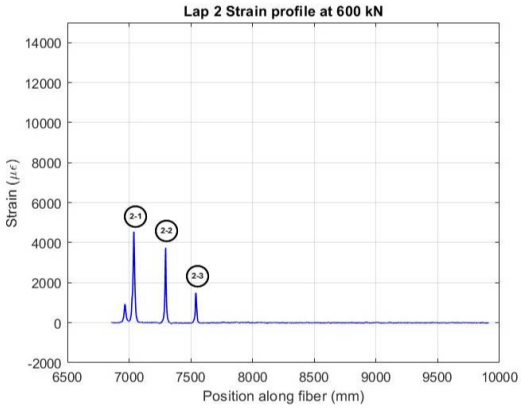

(c) Strain profile at Lap 2.

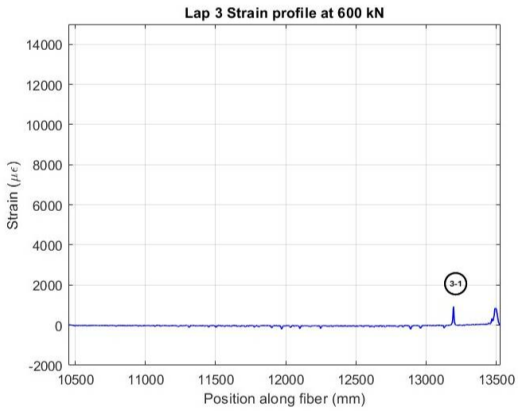

(d) Strain profile at Lap 3.

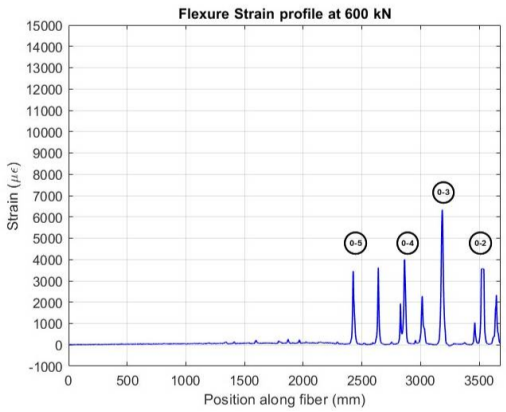

(e) Strain profile at Lap 0: Flexure.

Figure 4.2: Crack development at 600 kN load: (a) overall crack pattern and (b–e) DFOS strain profile at different laps.

3. Crack development at 800 kN Load

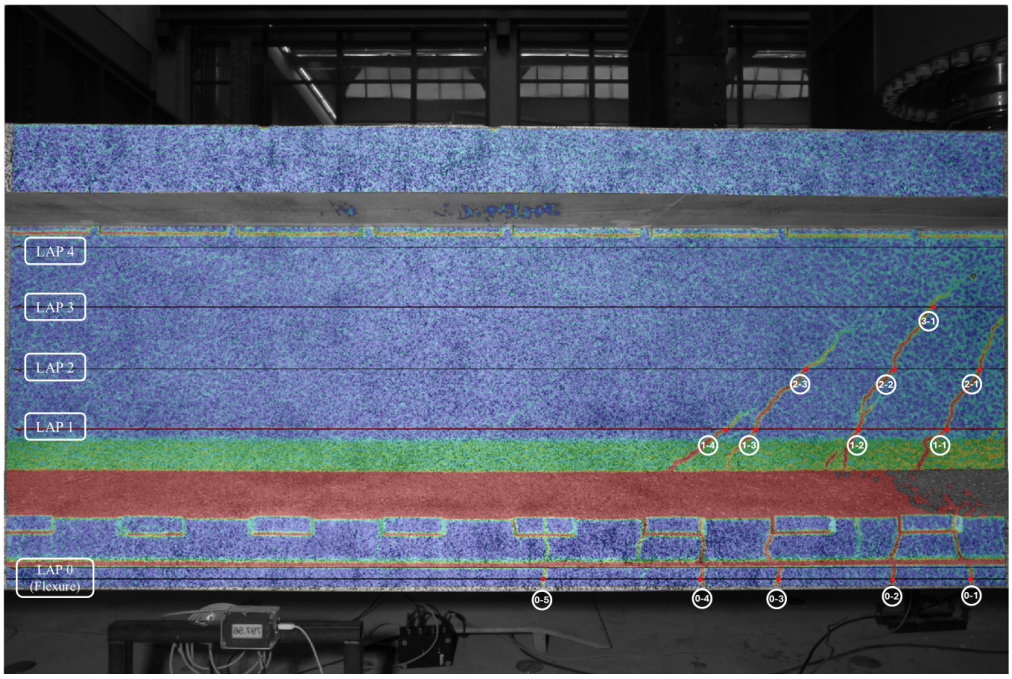

(a) Overall crack pattern at 800 kN.

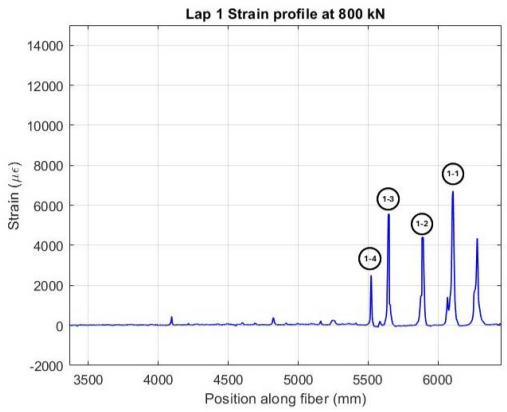

(b) Strain profile at Lap 1.

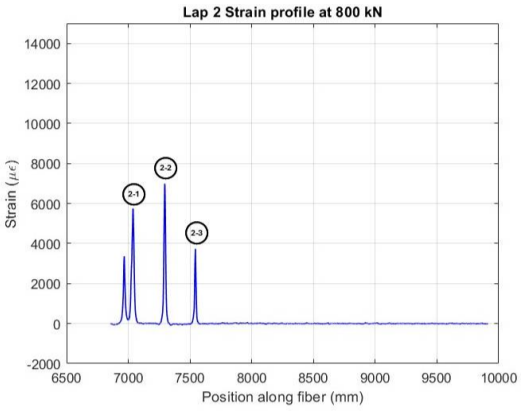

(c) Strain profile at Lap 2.

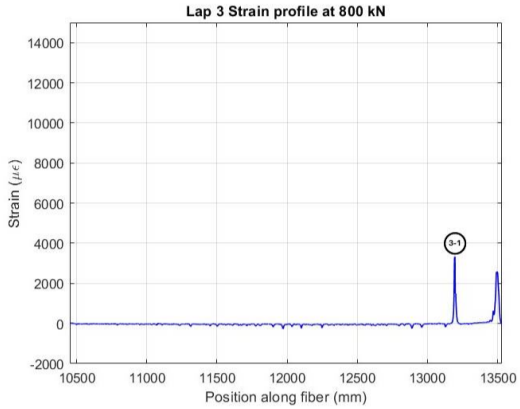

(d) Strain profile at Lap 3.

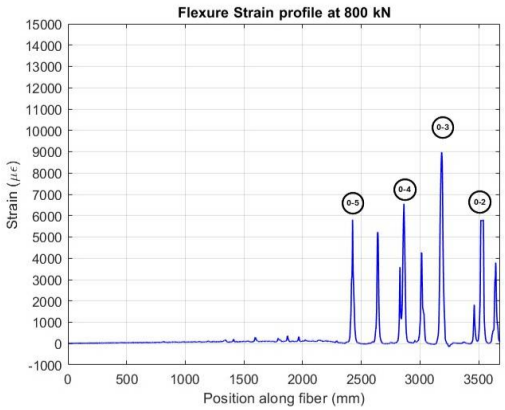

(e) Strain profile at Lap 0: Flexure.

Figure 4.3: Crack development at 800 kN load: (a) overall crack pattern and (b–e) DFOS strain profile at different laps.

4. Crack development at 900 kN Load

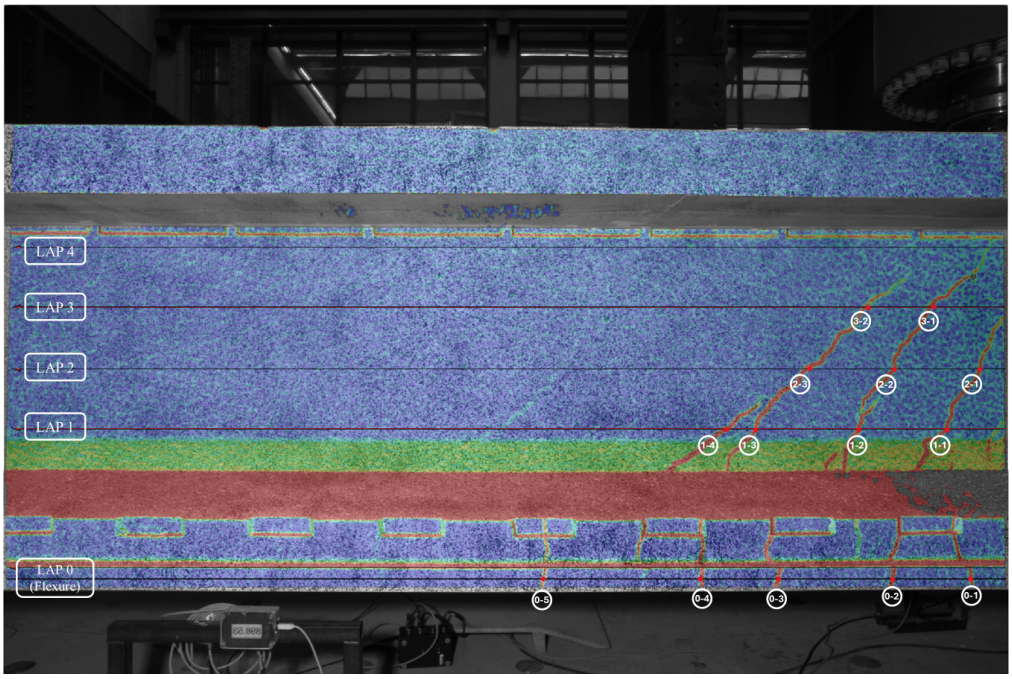

(a) Overall crack pattern at 900 kN.

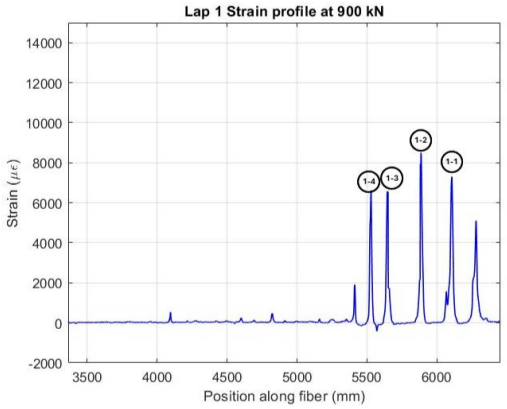

(b) Strain profile at Lap 1.

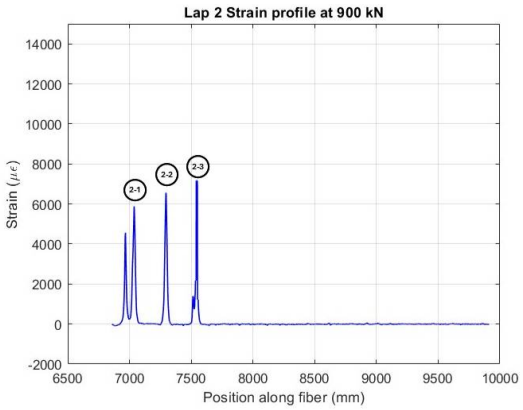

(c) Strain profile at Lap 2.

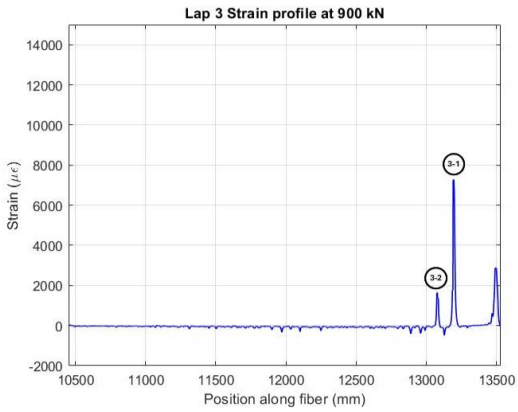

(d) Strain profile at Lap 3.

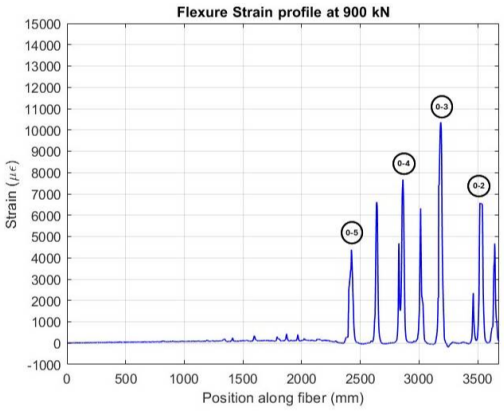

(e) Strain profile at Lap 0: Flexure.

Figure 4.4: Crack development at 900 kN load: (a) overall crack pattern and (b–e) DFOS strain profile at different laps.

5. Crack development at 950 kN Load

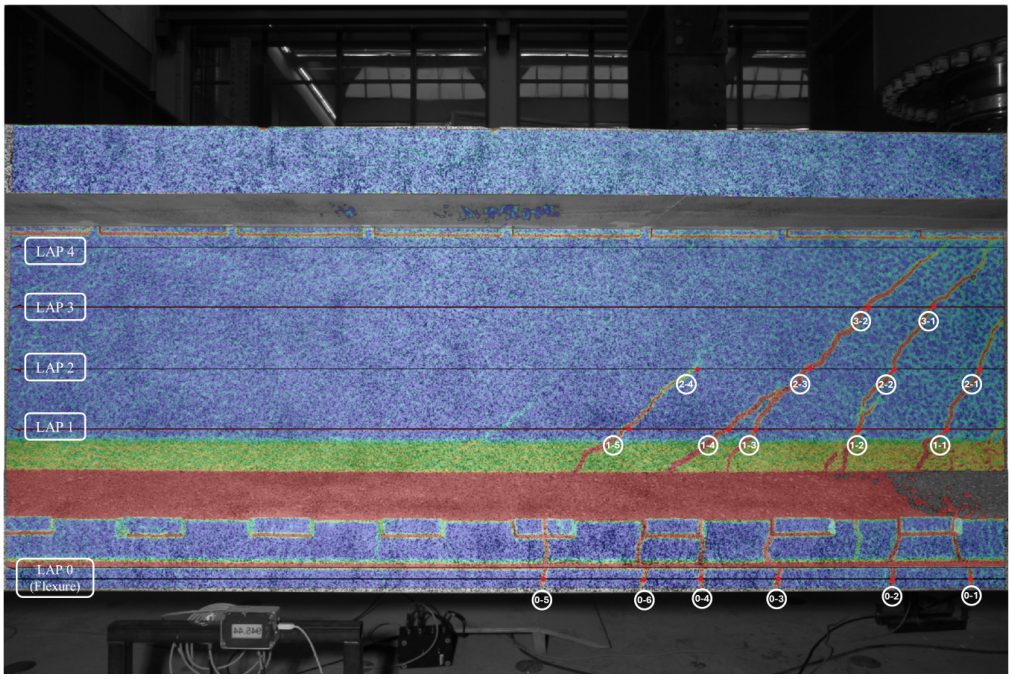

(a) Overall crack pattern at 950 kN.

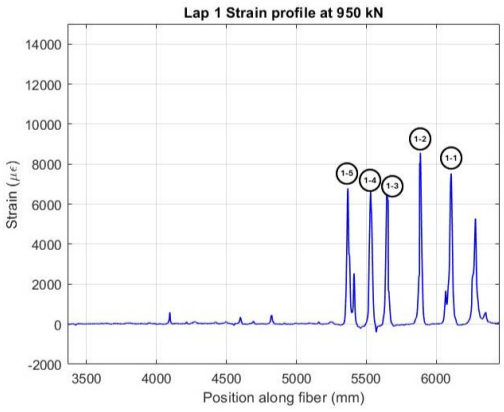

(b) Strain profile at Lap 1.

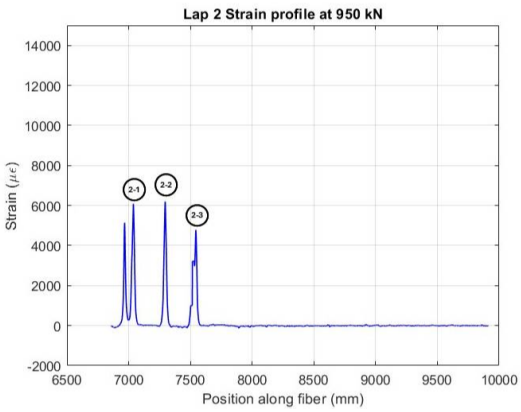

(c) Strain profile at Lap 2.

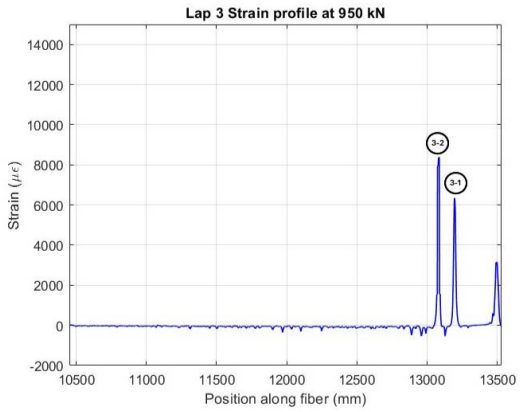

(d) Strain profile at Lap 3.

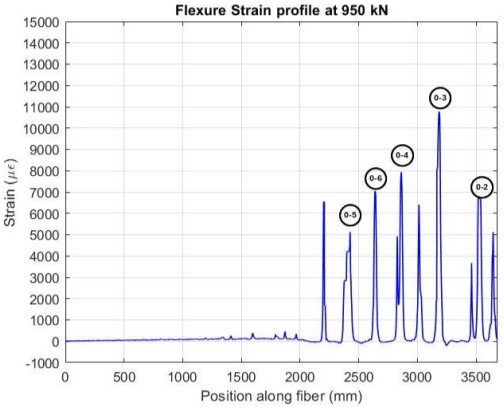

(e) Strain profile at Lap 0: Flexure.

Figure 4.5: Crack development at 950 kN load: (a) overall crack pattern and (b–e) DFOS strain profile at different laps.

6. Crack development at 1000 kN Load

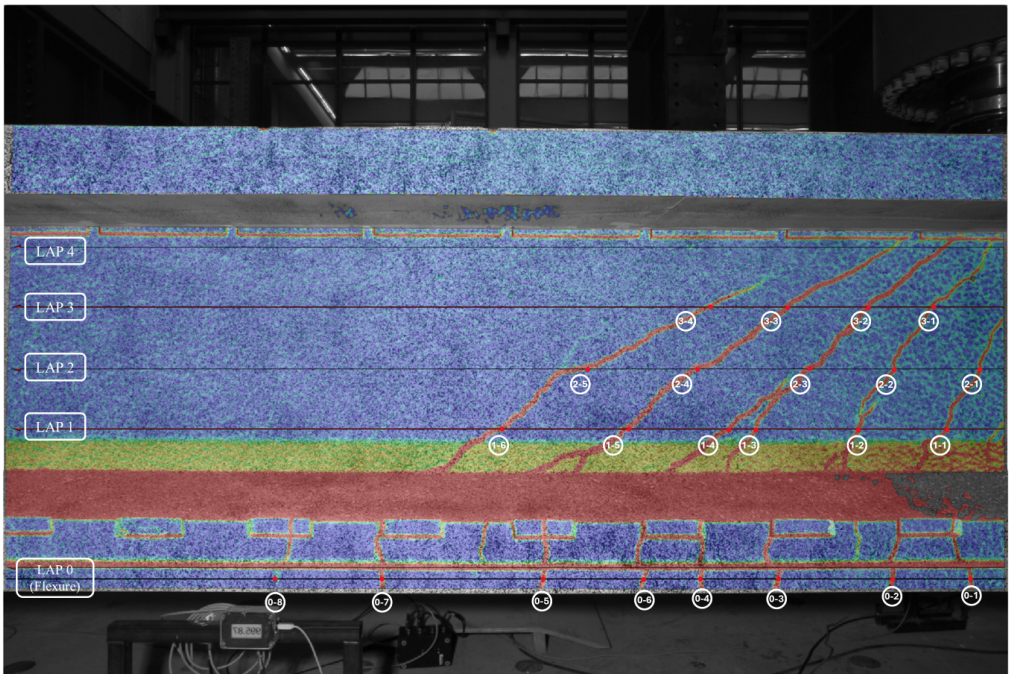

(a) Overall crack pattern at 1000 kN.

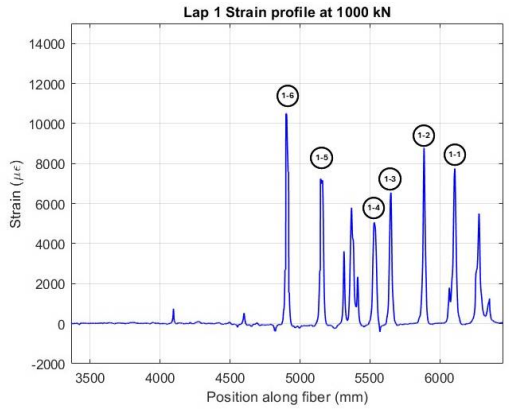

(b) Strain profile at Lap 1.

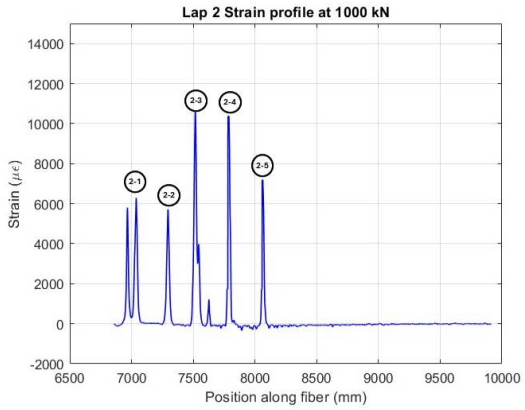

(c) Strain profile at Lap 2.

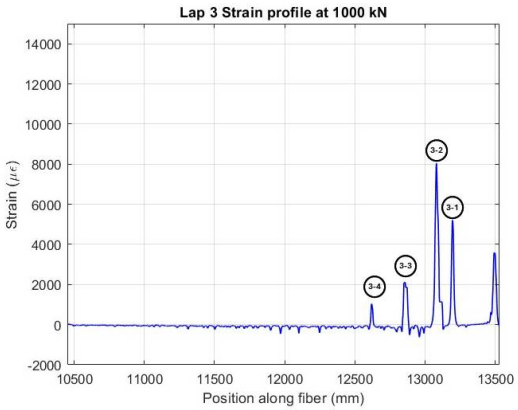

(d) Strain profile at Lap 3.

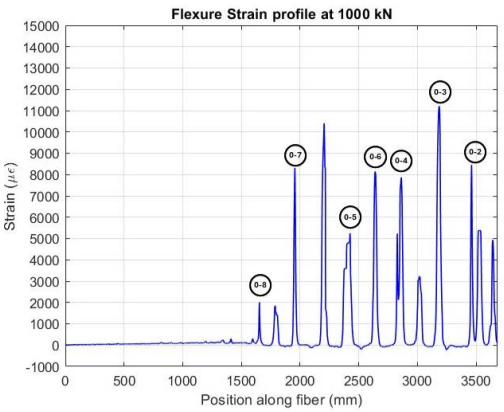

(e) Strain profile at Lap 0: Flexure.

Figure 4.6: Crack development at 1000 kN load: (a) overall crack pattern and (b–e) DFOS strain profile at different laps.

7. Crack development at 1050 kN Load

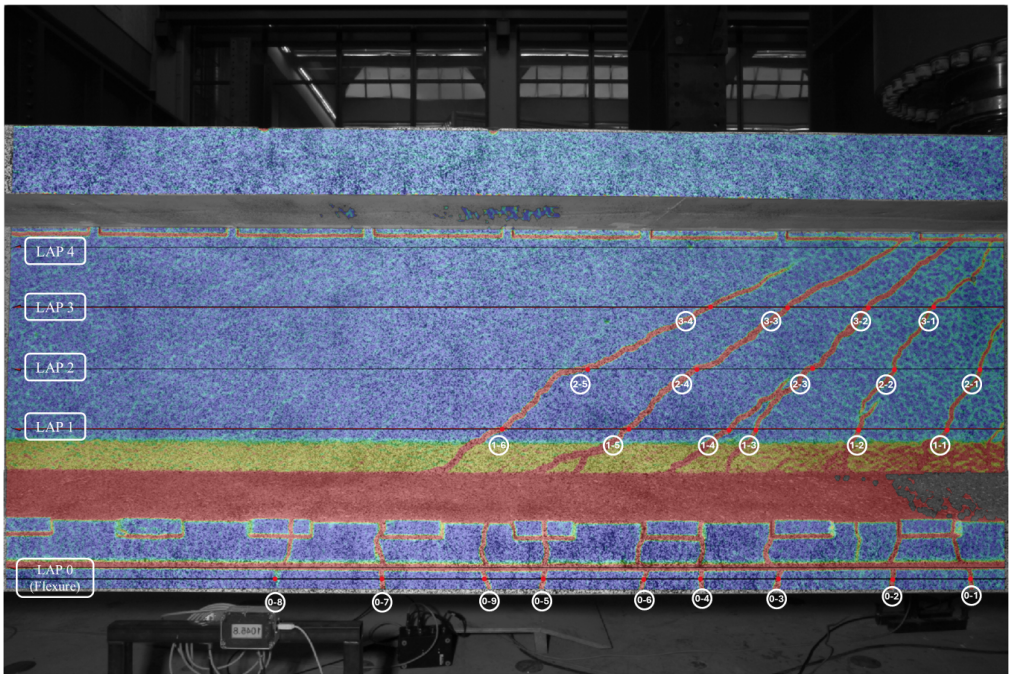

(a) Overall crack pattern at 1050 kN.

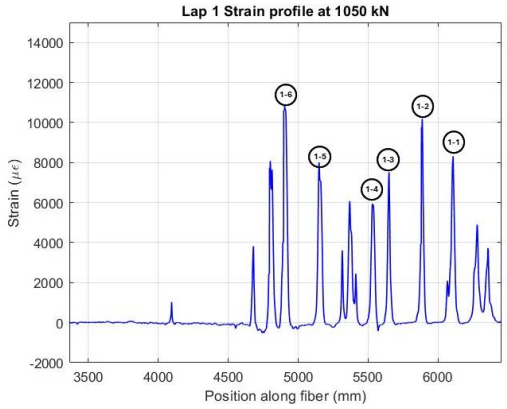

(b) Strain profile at Lap 1.

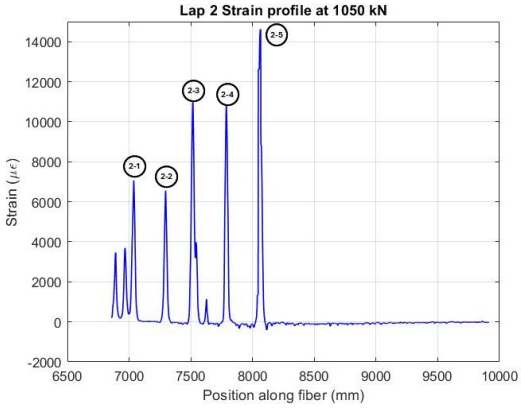

(c) Strain profile at Lap 2.

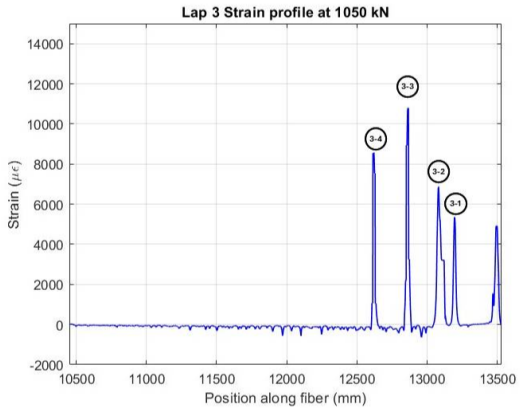

(d) Strain profile at Lap 3.

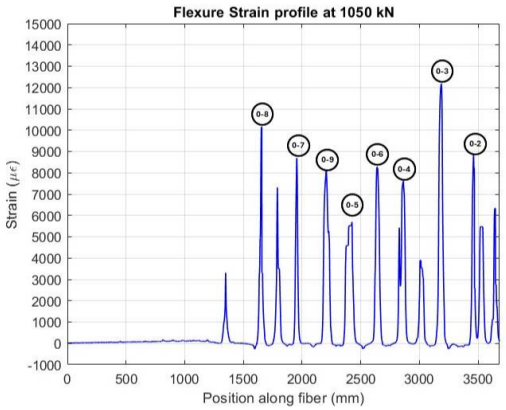

(e) Strain profile at Lap 0: Flexure.

Figure 4.7: Crack development at 1050 kN load: (a) overall crack pattern and (b–e) DFOS strain profile at different laps.

8. Crack development at 1100 kN Load

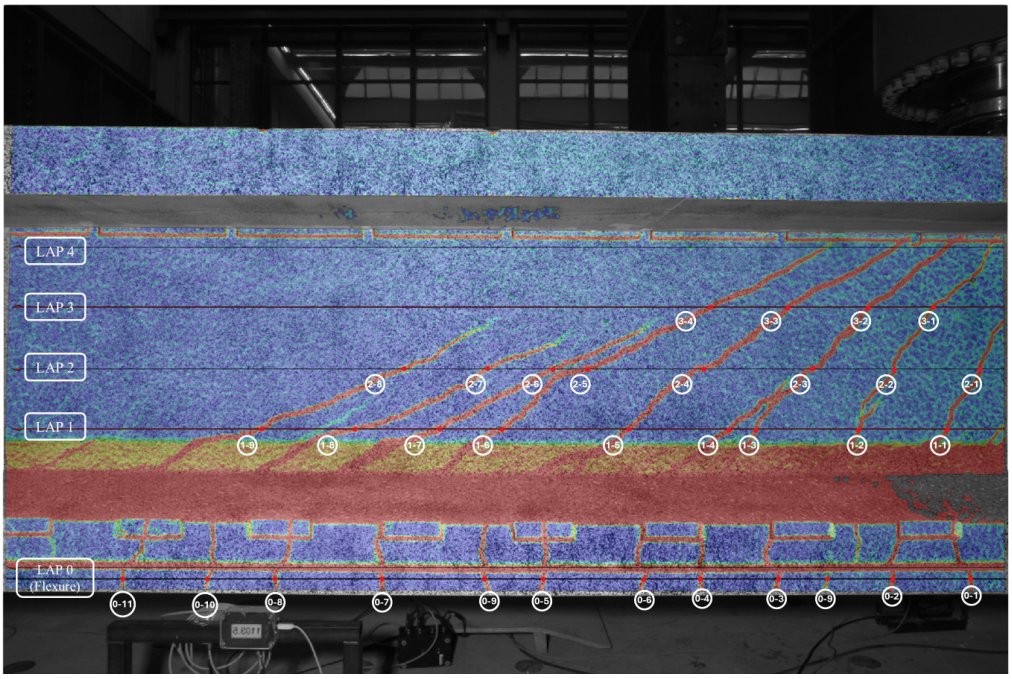

(a) Overall crack pattern at 1100 kN.

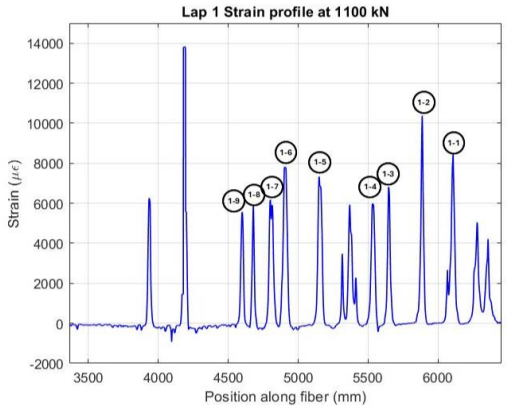

(b) Strain profile at Lap 1.

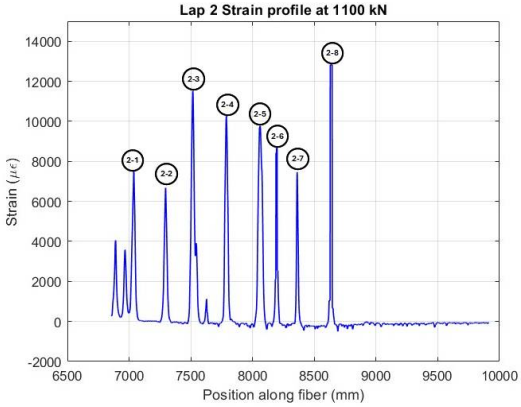

(c) Strain profile at Lap 2.

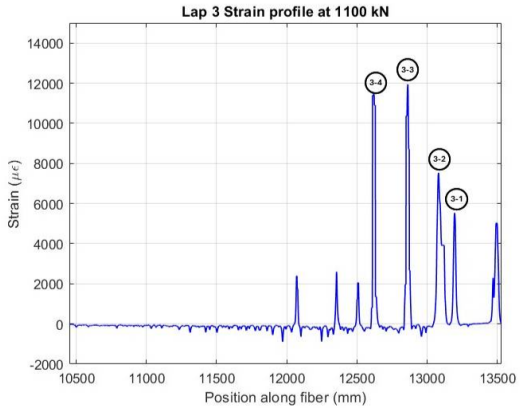

(d) Strain profile at Lap 3.

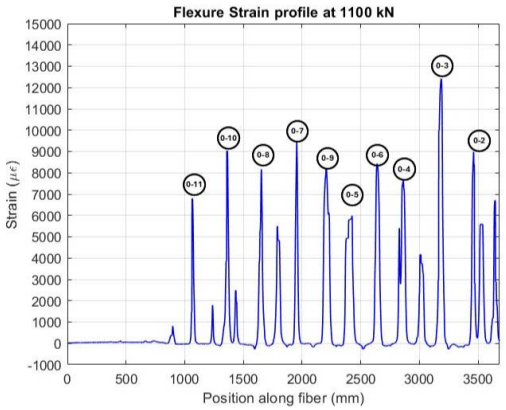

(e) Strain profile at Lap 0: Flexure.

Figure 4.8: Crack development at 1100 kN load: (a) overall crack pattern and (b–e) DFOS strain profile at different laps.

9. Specimen at failure

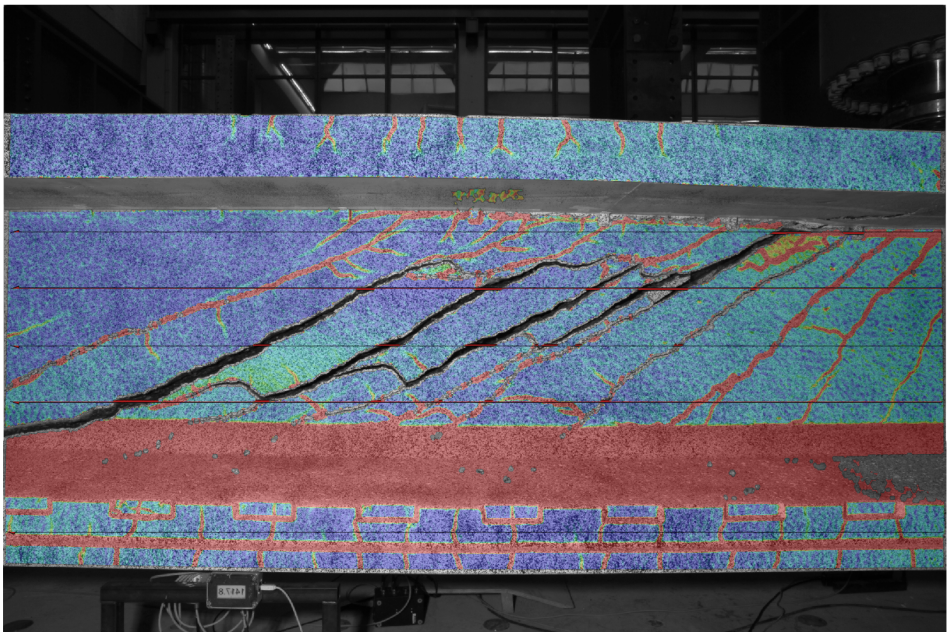

(a) Failure state of the specimen - DIC side (flipped)

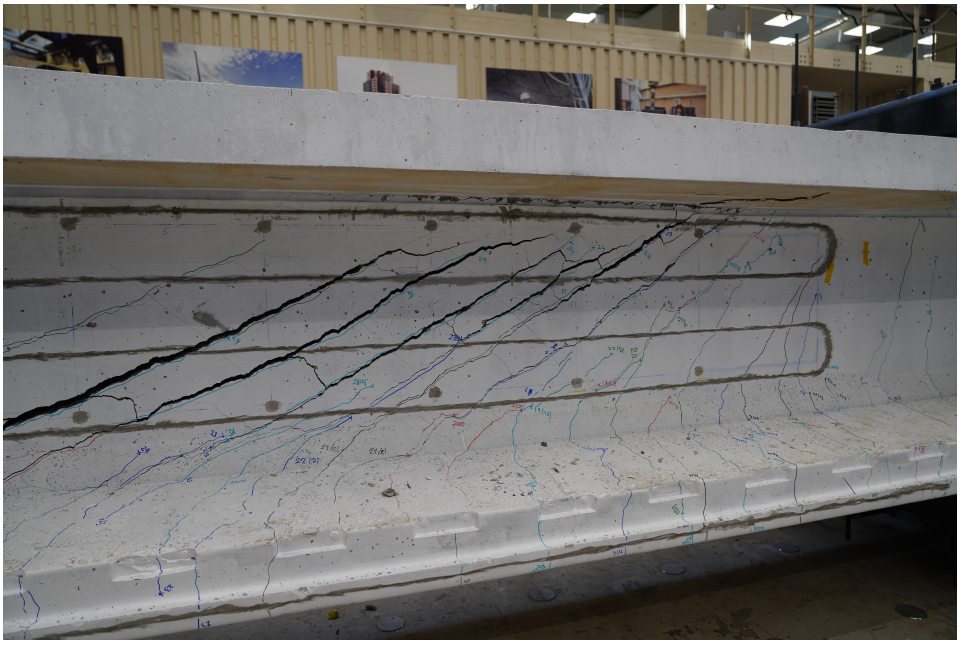

(b) Failure state of the specimen - DFOS side

Figure 4.9: Specimen at failure

4.2.1. Discussion on qualitative crack detection using DFOS

The inverted T-girder test confirms that surface-bonded DFOS can qualitatively detect and localise cracks in reinforced concrete members. Localised peaks in the distributed strain profiles coincide well with the cracks identified by DIC, both for flexural cracks in the flange and for inclined shear cracks in the web. As the load increases, the evolution of peak number and magnitude provides a clear indication of crack initiation, propagation and relative severity along the monitored length. In this sense, DFOS offers a one-dimensional “crack map” with a spatial resolution that would be impractical to achieve using conventional point sensors.

At the same time, the T-girder results also highlight several limitations that are relevant for practical use. The quality of the crack signatures is sensitive to installation issues such as non-uniform adhesive thickness, local debonding at surface imperfections and incomplete fibre pretension. These imperfections manifest as noisy regions, attenuated peaks or short data gaps around some cracks. In addition, small spatial offsets between DFOS peaks and DIC cracks suggest that crack paths may not be perfectly symmetric through the thickness, and that DFOS readings on one face may not be the representation of the exact position of cracks observed on the opposite face.

Overall, the experiment demonstrates that DFOS is well-suited for crack detection and localisation in reinforced concrete members, provided that installation quality is adequately controlled. However, the observed attenuation and occasional distortion of strain peaks underline that the direct use of DFOS peak amplitudes for quantitative crack-width estimation requires careful calibration. This qualitative assessment therefore motivates the more detailed investigation of DFOS-derived crack widths in the four-point bending beams presented in the following sections.

4.3. Quantitative crack-width estimation using DFOS

The purpose of this section is to quantify crack widths along the tension surface of the four-point bending beams using distributed fibre optic sensor (DFOS) data and to compare these results with reference measurements from Digital Image Correlation (DIC). The theoretical background and general workflow for deriving crack widths from DFOS strain profiles were introduced in Section 2.3.1 (after Richter et al. [50]). Here, the same approach is applied to the experimental data from the beams, using the calibrated strain-transfer efficiency from Chapter 3 to relate DFOS strains to concrete surface strains.

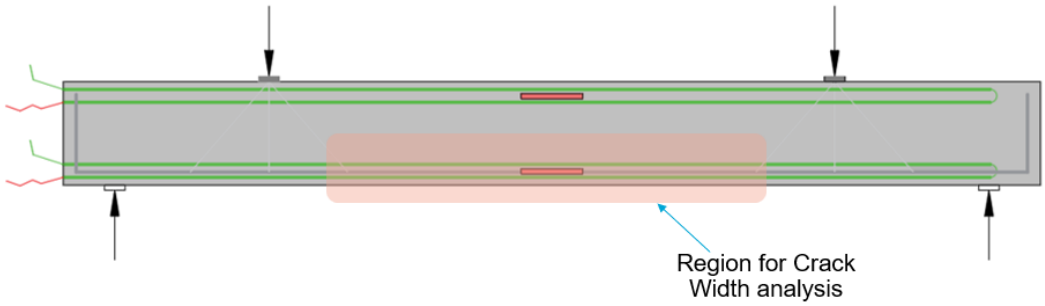

Figure 4.10: Region for crack width analysis

While several studies have estimated crack widths using DFOS, most focus on embedded or near-surface fibres; fewer address surface-bonded sensors on concrete structures. In this work, we evaluate the capability of surface-bonded DFOS to recover crack widths in our beam tests and establish a quantitative relationship between DFOS-derived crack widths and reference measurements from digital image correlation (DIC). The specific objective is to compare DFOS-inferred crack widths against DIC at matched load steps, assess accuracy (bias) and scatter, and discuss practical limits arising from strain-transfer effects.

4.3.1. Experimental Methodology

The methodology for identifying crack width follows the approach established by Richter et al. [50], as detailed in Chapter 2. The experimental workflow is outlined below:

1. Data acquisition

   DFOS data were acquired using the Luna ODiSI 6100 interrogator with a gauge pitch of 1.3 mm. For each considered load stage, the interrogator output was exported as a `.tsv` file containing gage positions and strain values along the fibre, together with metadata on the measurement settings. The DIC system provided full-field displacement and strain fields on the tension face of the beams, from which reference crack widths were obtained at matching load levels.

2. Data pre-processing

   DFOS data typically contains three disturbance types: measurement noise, strain reading anomalies (SRAs) and dropouts. Pre-processing was implemented in Python using the `fosanalysis` framework and consisted of:

   Strain reading anomalies (SRA) implausibly large point-to-point jumps along the fibre were converted to dropouts using a gradient-threshold masking (GTM) criterion. Samples where the absolute difference between consecutive gauges exceeded a threshold $\Delta_{\max}$ were flagged and set to NaN. The threshold was chosen high enough to preserve sharp but physically plausible crack peaks.

   Repair of dropouts. Dropouts (non-finite values, `NaN`) were replaced via interpolation. Short gaps were filled using the default Akima 1-D interpolator (`Akima1DInterpolator`), which is shape-preserving and avoids the overshoot typical of standard cubic splines, thereby maintaining crack-peak amplitude and location.

   Spatial filtering (sliding median). For minimal smoothing, a sliding median with radius $= 1$ (3-sample window) was also used. The median operator (`nanmedian`) ignores `NaN` values and is robust to isolated outliers. A small radius was chosen deliberately to preserve the amplitude and location of narrow crack-related peaks while providing only minimal baseline smoothing; larger windows were avoided to prevent attenuation or merging of neighbouring peaks.

   The pre-processed data was then plotted as a processed strain profile (See Figure 4.11).

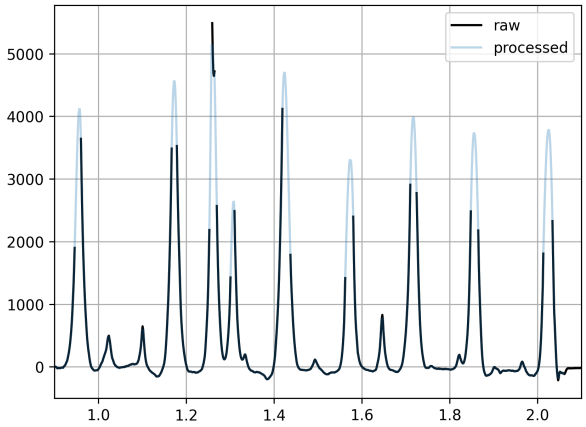

Figure 4.11: Raw data versus pre-processed data

3. Crack detection

   The peak-detection thresholds (height, prominence) were referenced to the concrete's mean tensile strain at cracking, estimated as $\varepsilon_{ctu} \approx f_{ctm}/E_{cm}$. For C35/45 concrete this gives $\varepsilon_{ctu} \approx 94.2\ \mu\varepsilon$. Because the DFOS was bonded to the surface and measured only a fraction of the true concrete strain (Section 3.9), a strain-transfer efficiency $STE = 0.40$ was applied. Accordingly, the detection thresholds were set relative to the observed level $\varepsilon_{ctu,crack} = STE \cdot \varepsilon_{ctu} \approx 38\ \mu\varepsilon$. This anchors prominence- and height-based crack identification to a physically meaningful tensile-strain scale while accounting for strain-transfer losses in the adhesive layer.

4. Estimation of transfer length

   Strain measurements in DFOS are obtained exclusively from the fibre core, with strain transferred via bonding from the surrounding material. This transfer mechanism introduces a strain lag, causing the theoretically infinite strain peak at a crack location to be distributed across a finite region along the fibre. If the transfer length is excessively long, strain peaks from adjacent cracks may overlap, resulting in merged signals that compromise the reliability of crack detection. Therefore, selecting an appropriate DFOS type and installation method is critical to ensure accurate strain localization.

In this study, we employed the minimum strain approach to estimate the transfer length. This method defines the transfer length as the region between local minima of the measured strain signal, situated between adjacent strain peaks. Where, $x_{\min,l,i}$ and $x_{\min,r,i}$ are the locations of the minimum strain $\varepsilon^{\mathrm{DFOS}}$ between the ith peak at the position $x_{cr,i}$ and its left neighbor (at $x_{cr,i-1}$) or its right neighbor (at $x_{cr,i+1}$). Consequently, the transfer lengths to the left and right of the ith crack are

$$l^{-}_{t,\min,i} = x_{cr,i} - x_{\min,l,i}, \tag{4.1a}$$

$$l^{+}_{t,\min,i} = x_{\min,r,i} - x_{cr,i}. \tag{4.1b}$$

5. Tension stiffening compensation

   The load bearing contribution of the concrete in between cracks is called tension stiffening. Generally, the strains measured by DFOS are influenced by tension stiffening [50]. However, they are more prominent in embedded DFOS. But in our study, for the surface bonded fibre the tensioning stiffening compensation did not seem to have any noticeable influence on the crack width estimation. Hence, the tension stiffening compensation was redundant.

6. Obtaining crack widths

   The strains for individual cracks were integrated over the transfer length to obtain the crack widths as shown in Figure 4.12. For each identified crack, the crack width w_{DFOS} was computed by numerically integrating the excess tensile strain around the crack location:

$$w_{\mathrm{DFOS}} = \int_{x_1}^{x_2} \varepsilon_c(x)\,\mathrm{d}x, \tag{4.2}$$

   where, x_1 and x_2 define the integration interval around the peak. The limits x_1 and x_2 were chosen such that the integrand returned to the baseline level on both sides of the crack.

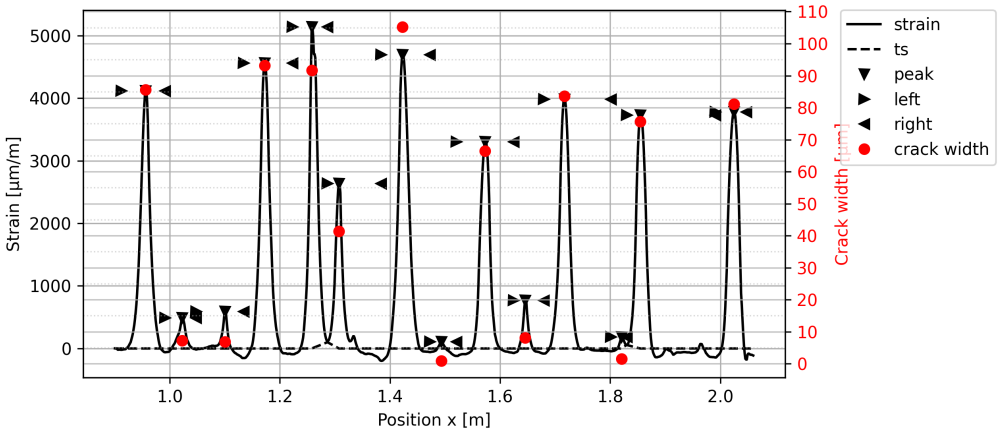

Figure 4.12: Final output of crack width analysis for DFOS

4.3.2. Results and comparison

The results for crack width analysis and a comparison between the crack widths obtained by DFOS and DIC, along with their error, is presented for each specimen individually here from different load stages. For each specimen, DFOS-derived crack widths are reported at selected load stages and compared to the corresponding DIC measurements using a consistent co-registration and quality-control protocol. The figures display representative crack profiles, the inferred widths from DFOS, the reference widths from the optical system, and the associated error measures. The results are organised by specimen and load stage to show how crack development and estimation accuracy evolve together.

The acceptable threshold for crack width discrepancy between DIC and DFOS measured crack widths we set to 50 μm . This limit was selected based on prior validation as a plausible error margin for both measurement techniques [20].

4.3.2.1. Specimen 1: R3D8-AR47

The figures below show the crack widths captured by DIC (Figure 4.13 (a)) and the crack widths identified using the DFOS data (Figure 4.13) for the yielding load.

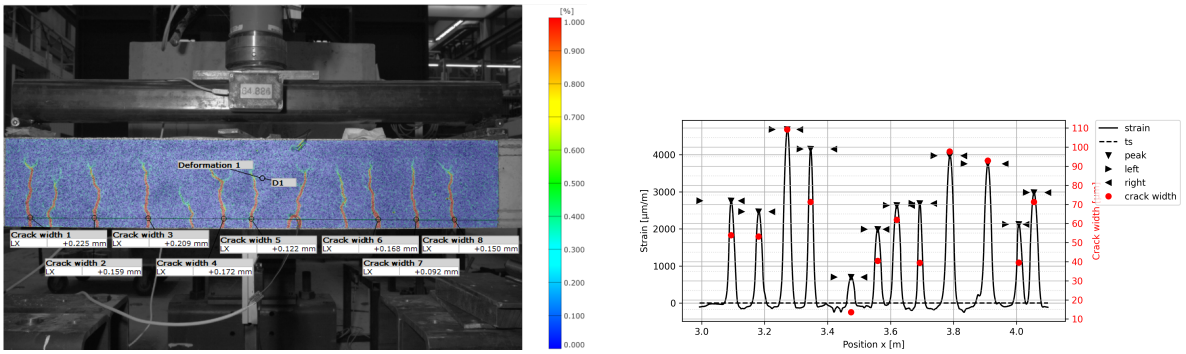

(a) Reference crack width using DIC at $P_{yielding}$

(b) Crack width using DFOS at $P_{yielding}$

Figure 4.13: Crack width comparison for Specimen 1 (R3D8-AR47).

The crack widths identified using DIC and DFOS exhibit noticeable discrepancies. These differences are evaluated across various cracks and load stages. Figure 4.14 illustrates the deviation in crack width measurements between the two methods, with individual crack-wise errors plotted against predefined acceptable error thresholds.

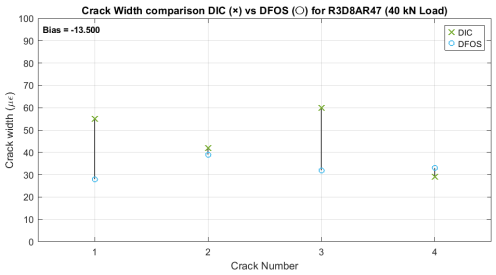

(a) Bias at $0.6P_y$

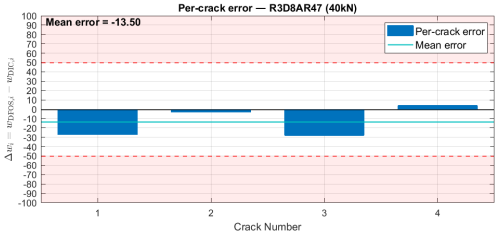

(b) Error at $0.6P_y$

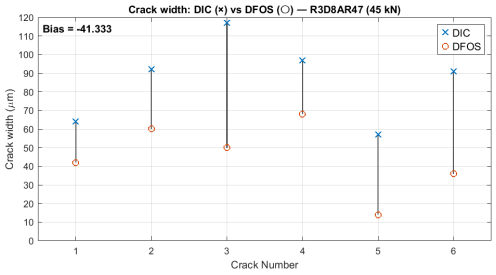

(c) Bias at $0.7P_y$

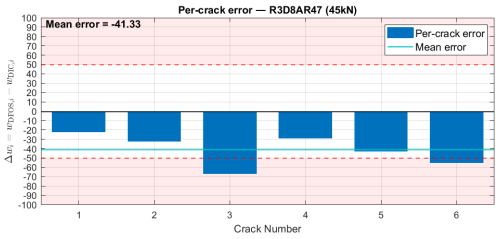

(d) Error at $0.7P_y$

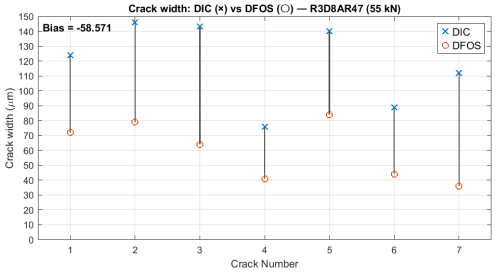

(e) Bias at $0.8P_y$

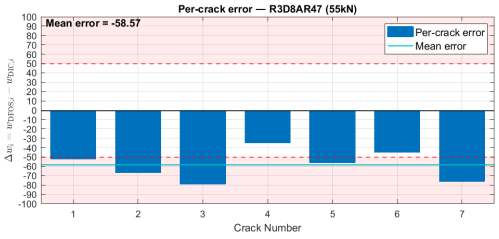

(f) Error at $0.8P_y$

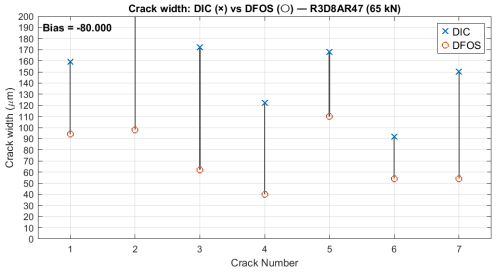

(g) Bias at P_y

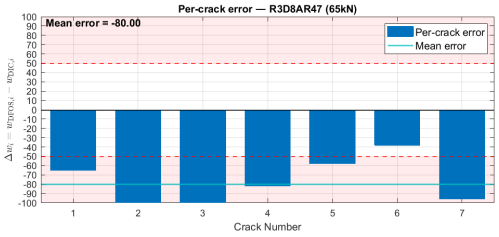

(h) Error at P_y

Figure 4.14: Bias and error per crack (Specimen 1)

4.3.2.2. Specimen 2: R4D8-DB

The figures below show the crack widths captured by DIC (Figure 4.15 (a)) and the crack widths identified using the DFOS data (Figure 4.15 (b)) for the yielding load.

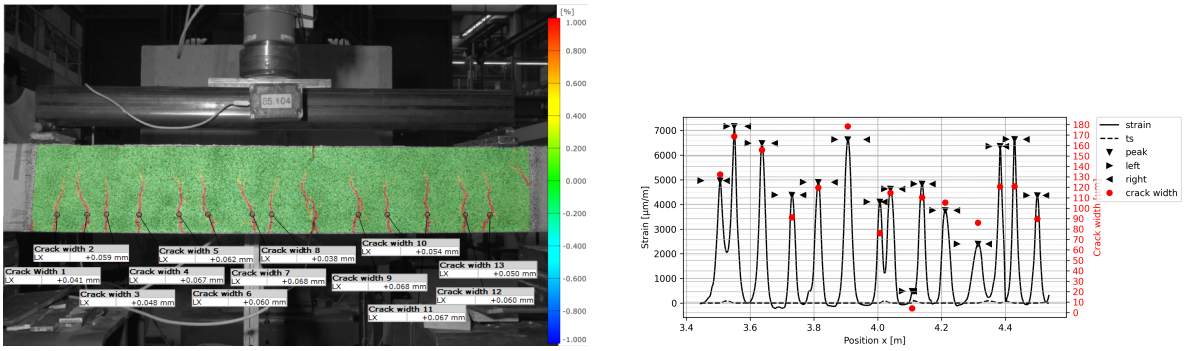

(a) Reference crack width using DIC at $P_{yielding}$

(b) Crack width using DFOS at $P_{yielding}$

Figure 4.15: Crack width comparison for Specimen 2 (R4D8-DB).

The crack widths identified using DIC and DFOS exhibit noticeable discrepancies. These differences are evaluated across various cracks and load stages. Figure 4.16 illustrates the deviation in crack width measurements between the two methods, with individual crack-wise errors plotted against predefined acceptable error thresholds.

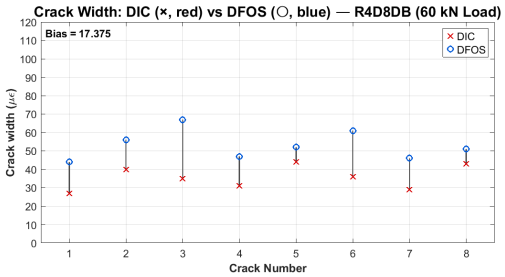

(a) Bias at $0.7P_y$

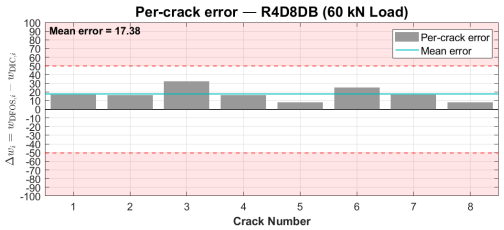

(b) Error at $0.7P_y$

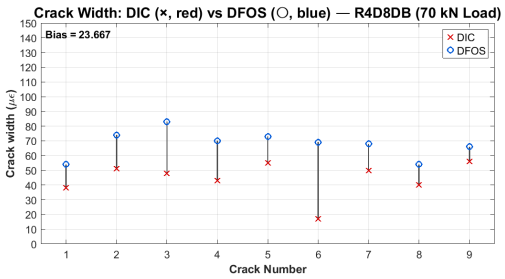

(c) Bias at $0.8P_y$

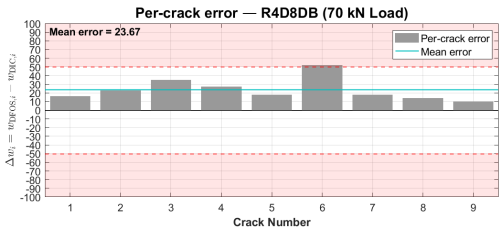

(d) Error at $0.8P_y$

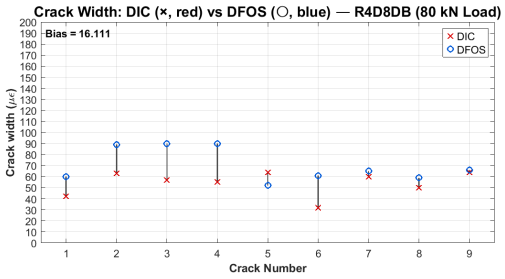

(e) Bias at $0.9P_y$

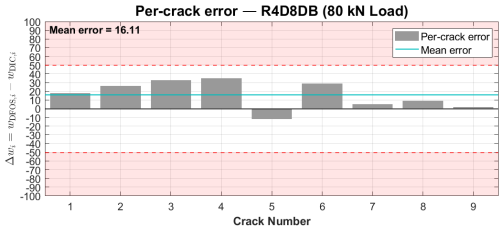

(f) Error at $0.9P_y$

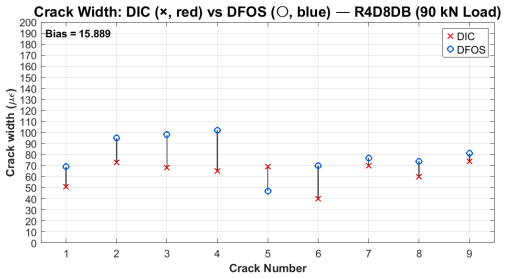

(g) Bias at P_y

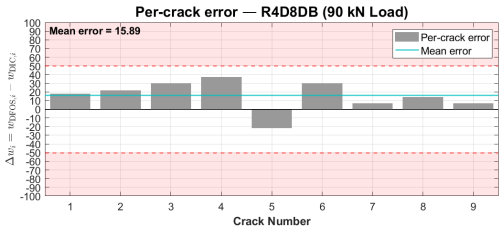

(h) Error at P_y

Figure 4.16: Bias and error per crack (Specimen 2).

4.3.2.3. Specimen 3: R3D10-CN

The figures below show the crack widths captured by DIC (Figure 4.17 (a)) and the crack widths identified using the DFOS data (Figure 4.17 (b)) for the yielding load.

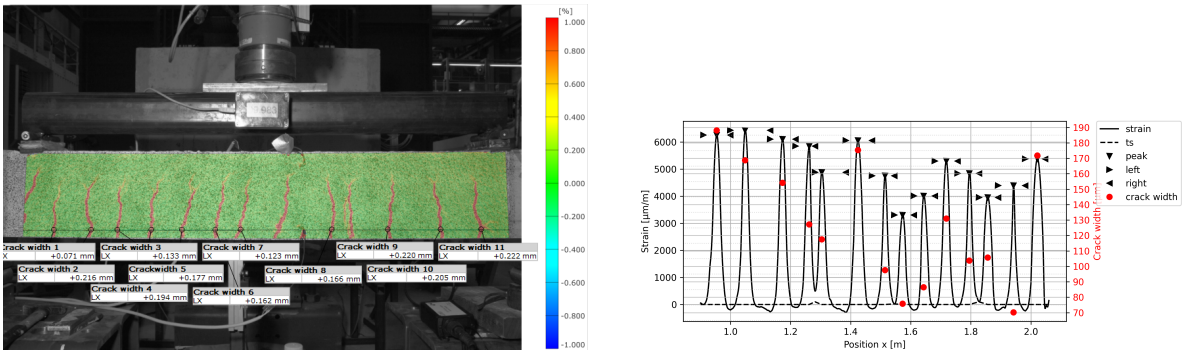

(a) Reference crack width using DIC at $P_{yielding}$

(b) Crack width using DFOS at $P_{yielding}$

Figure 4.17: Crack width comparison for Specimen 3 (R3D10-CN).

The crack widths identified using DIC and DFOS exhibit noticeable discrepancies. These differences are evaluated across various cracks and load stages. Figure 4.18 illustrates the deviation in crack width measurements between the two methods, with individual crack-wise errors plotted against predefined acceptable error thresholds.

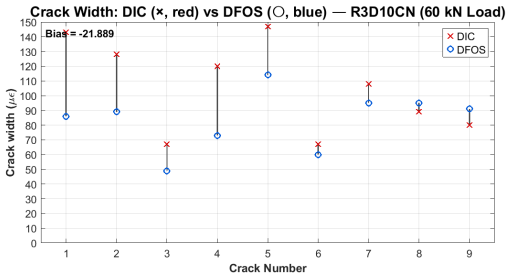

(a) Bias at $0.6P_y$

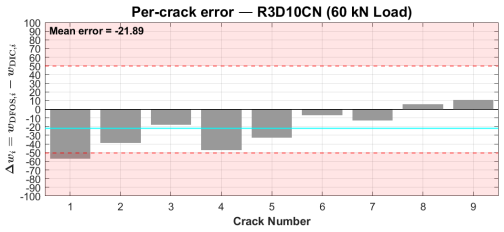

(b) Bias at $0.6P_y$

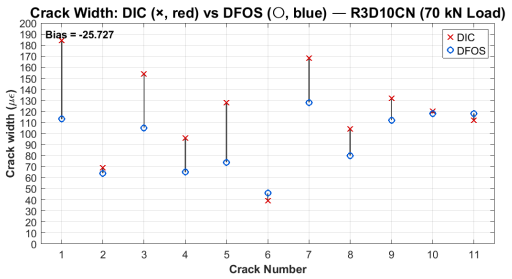

(c) Bias at $0.7P_y$

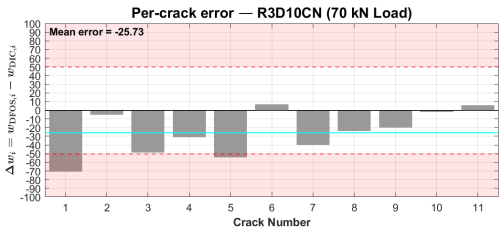

(d) Bias at $0.7P_y$

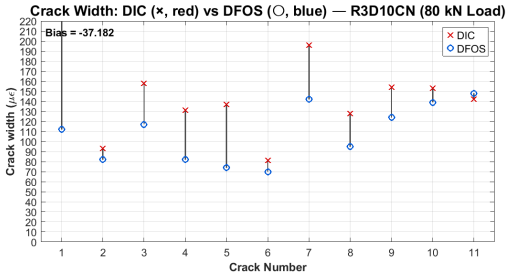

(e) Bias at $0.8P_y$

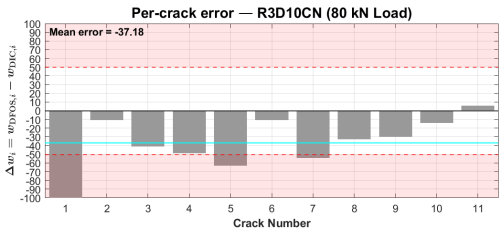

(f) Bias at $0.8P_y$

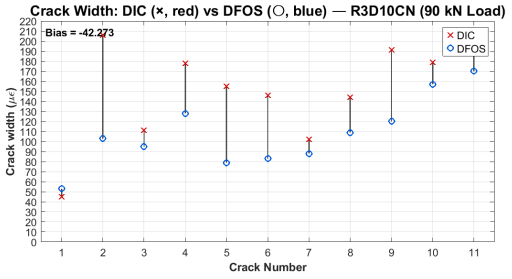

(g) Bias at $0.9P_y$

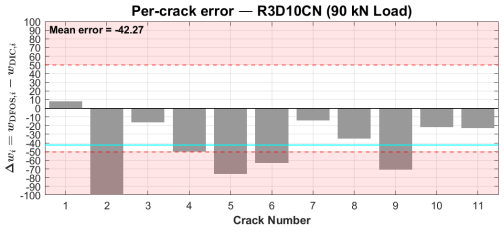

(h) Bias at $0.9P_y$

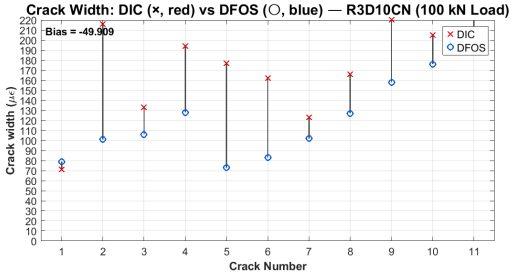

(i) Bias at P_y

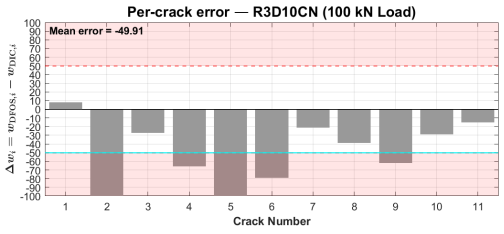

(j) Bias at P_y

Figure 4.18: Bias and error per crack (Specimen 3).

4.3.2.4. Specimen 4: R3D12-AR14

The figures below show the crack widths captured by DIC (Figure 4.19 (a)) and the crack widths identified using the DFOS data (Figure 4.19) for the yielding load.

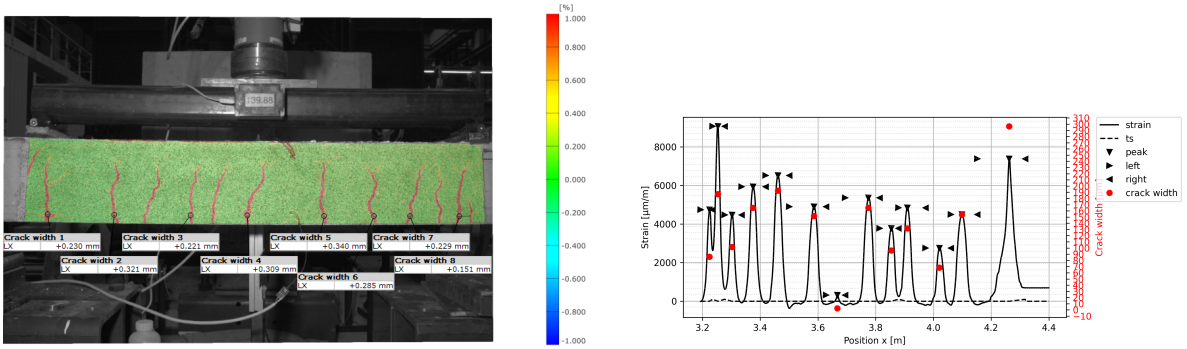

(a) Reference crack width using DIC at $P_{yielding}$

(b) Crack width using DFOS at $P_{yielding}$

Figure 4.19: Crack width comparison for Specimen 3 (R3D12-AR14).

The crack widths identified using DIC and DFOS exhibit noticeable discrepancies. These differences are evaluated across various cracks and load stages. Figure 4.20 illustrates the deviation in crack width measurements between the two methods, with individual crack-wise errors plotted against predefined acceptable error thresholds.

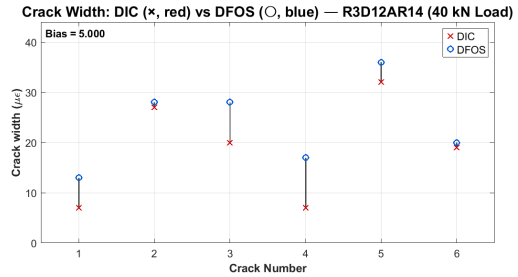

(a) Bias at $0.3P_y$

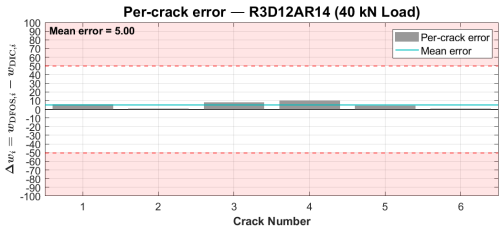

(b) Error at $0.3P_y$

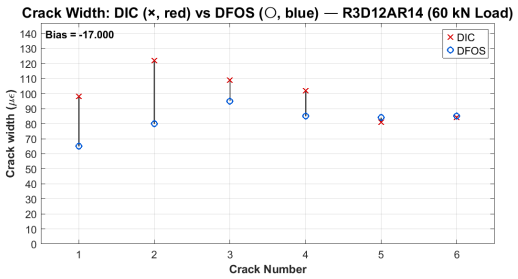

(c) Bias at $0.4P_y$

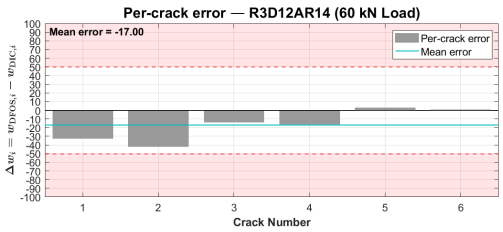

(d) Error at $0.4P_y$

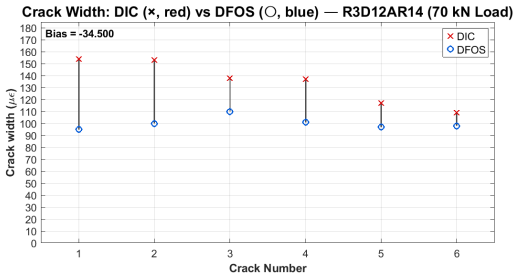

(e) Bias at $0.5P_y$

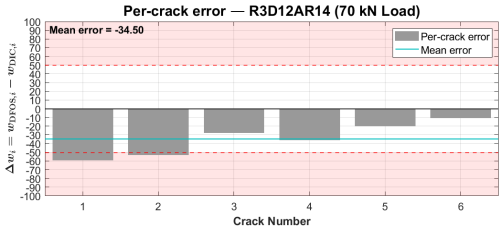

(f) Error at $0.5P_y$

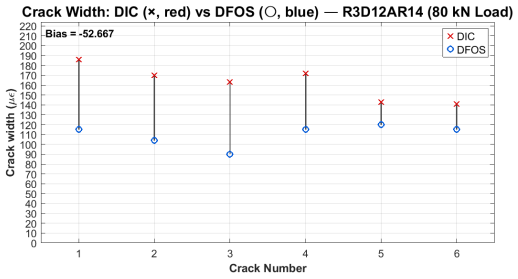

(g) Bias at $0.6P_y$

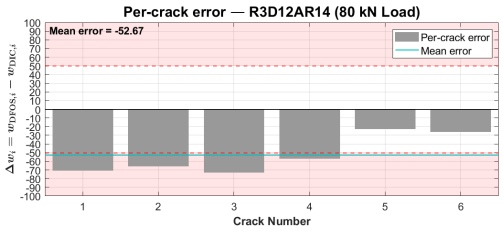

(h) Error at $0.6P_y$

Figure 4.20: Bias and error per crack (Specimen 3).

4.3.3. Mean error for all specimens

Figures 4.21–4.24 present the comparison between

- Mean error for Specimen 1 (R3D8-AR47)

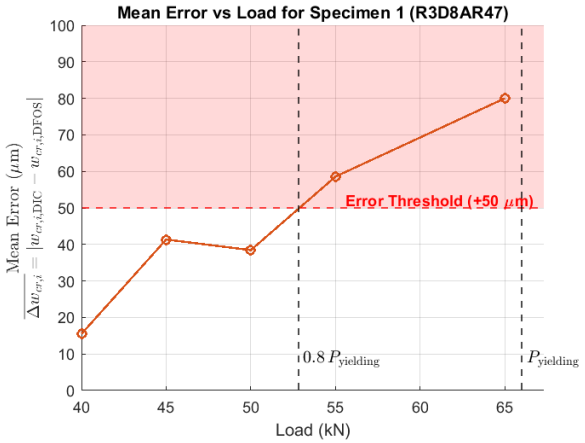

Figure 4.21: Mean error for Specimen 1

- Mean error for Specimen 2 (R4D8-DB)

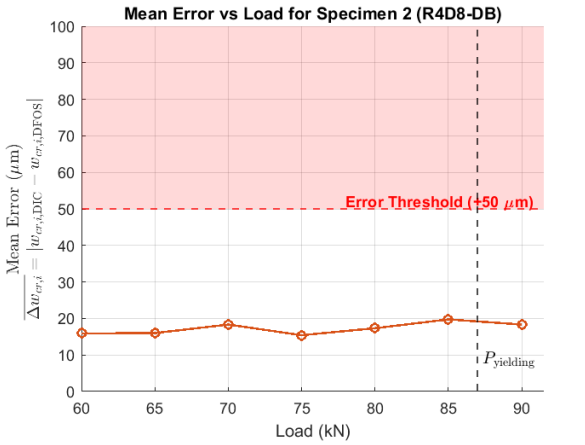

Figure 4.22: Mean error for Specimen 2

- Mean error for Specimen 3 (R3D10-CN)

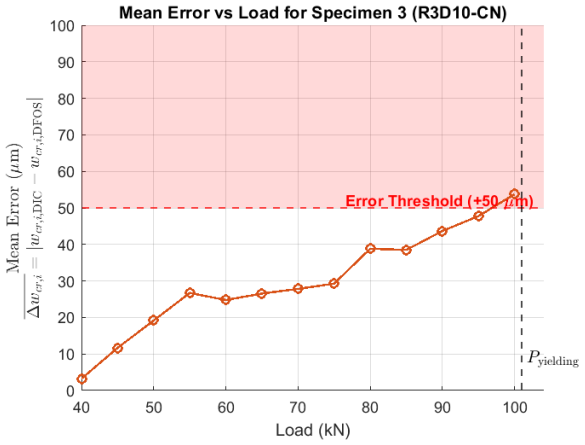

Figure 4.23: Mean error for Specimen 3

- Mean error for Specimen 4 (R3D12-AR14)

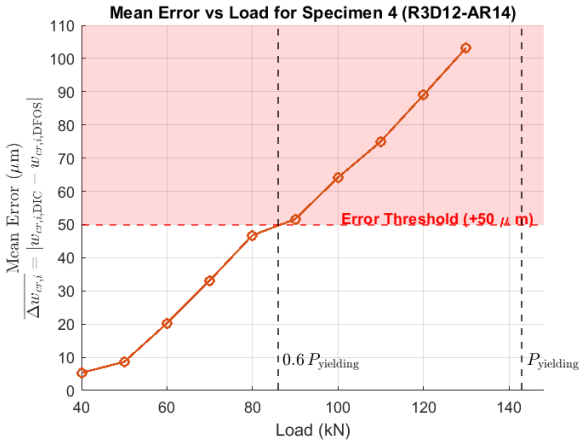

Figure 4.24: Mean error for Specimen 4

The mean error observed in Specimens 2 and 3 remained well within the acceptable threshold limits up to the point of yielding load, $P_{yielding}$. In Specimen 1, reliable crack identification was achievable up to $0.8P_y$, which is considered satisfactory. However, in Specimen 4, the error threshold was exceeded prematurely at $0.6P_y$, indicating reduced reliability in early-stage strain measurements which can be traced back to larger crack widths.

These observations indicate that for relatively small crack widths, the discrepancy between measurement methods remains minimal. However, as crack widths increase, the DFOS system tends to exhibit a higher incidence of missing data, particularly around strain peaks. This missing data must be reconstructed through interpolation, which inherently introduces approximation errors. When such gaps coincide with critical strain features, the accuracy of interpolation becomes pivotal. Therefore, it is essential to evaluate the acceptable level of interpolation accuracy to ensure that crack width estimates derived from DFOS remain valid and reliable.

4.3.4. Discussion on quantitative crack-width estimation using DFOS

Overall, the following trends were observed:

- DFOS reliably detected the majority of cracks identified by DIC in the constant moment region.All crack even the one with very small widths, were picked up by the DFOS algorithm.
- For most cracks, DFOS-derived widths were in reasonable agreement with DIC, with absolute errors on the order of a few tenths of a millimetre. The scatter increased with crack width, but no strong systematic over- or underestimation was observed across all beams.
- It was also observed that the crack widths that were found the exceed the permissible threshold of 50 μm were mostly cracks that had larger widths as observed by the DIC.
- In cases where the DFOS strain peaks were affected by missing data in the crack zone, the reconstructed peaks still allowed a crack width to be computed, but the associated error tended to be larger. This effect is analysed more systematically in Section 4.4.

4.4. Quantifying the Impact of Missing DFOS Peaks: An Le/L Analysis on Dominant Cracks

In the previous section we showed how crack widths can be estimated from DFOS strain data in concrete. When cracks form, the strain gradient near the crack changes very fast, and the DFOS signal often has dropouts (missing or unusable points), which is traced back to failed cross-correlation of the data from its reference state [50]. We usually fill these gaps by interpolation. If the gap is between peaks and valleys, a simple sliding filter works well. This becomes uncertain when the peak itself is

missing, because the peak shape controls the crack-width estimate. Using our crack-width algorithm we can rebuild missing peaks (see Figure 4.25), but this is still an approximation and may not be the true representation of the actual peak. In this section, we check how much this affects the result. We define a symmetric window L which is the distance of the peak at the baseline or zero around each crack and measure the total missing length Le that is the distance of the top two points of the peak and the ratio $\mathrm{Le}/L \in [0, 1]$ tells us how much data is missing as shown in Figure 4.26 (0 = perfect peak, 1 = poor peak). For each of the four specimens, we choose one dominant crack in the constant-moment region and study several load stages from first cracking to yield. We interpolate the DFOS data, compute crack widths from it, and compare them with DIC crack widths to measure the error. This lets us see how interpolation accuracy changes with Le/L and if the interpolation method used is reliable for crack-width estimation.

In most cases, the strain curve detected from the raw data is not symmetric i.e. one part of the curve detects more data than the other (see Figure 4.27). In this case, the horizontal distance from the lower point in the missing peak to the other end of the curve is considered as L_e

This section quantifies how the interpolation accuracy of distributed fibre optic sensing degrades with the missing-data ratio Le/L around a crack. We analyse one dominant crack in the constant-moment region per specimen, across standardised load stages, and validate interpolated DFOS crack widths against Digital Image Correlation (DIC).

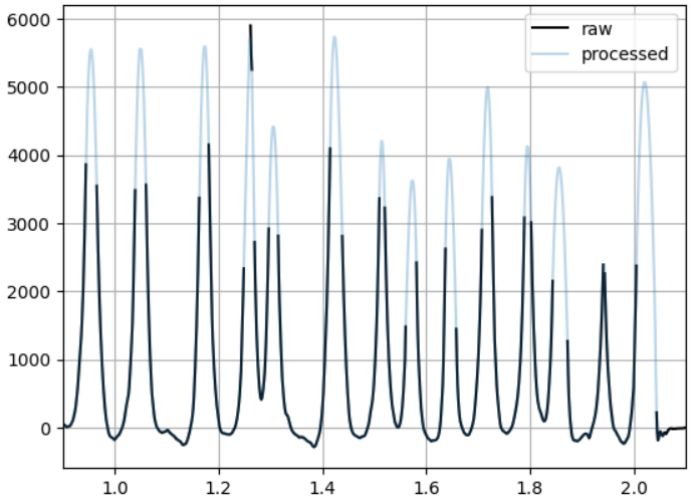

Figure 4.25: Raw data vs Interpolated data used for crack width analysis

By definition,

Le: L_e is the length of the strain curve's missing region.

L: L is the length of the strain curve at baseline or zero strain.

The ratio $\mathrm{Le}/L \in [0, 1]$ tells us how much of the window is missing:

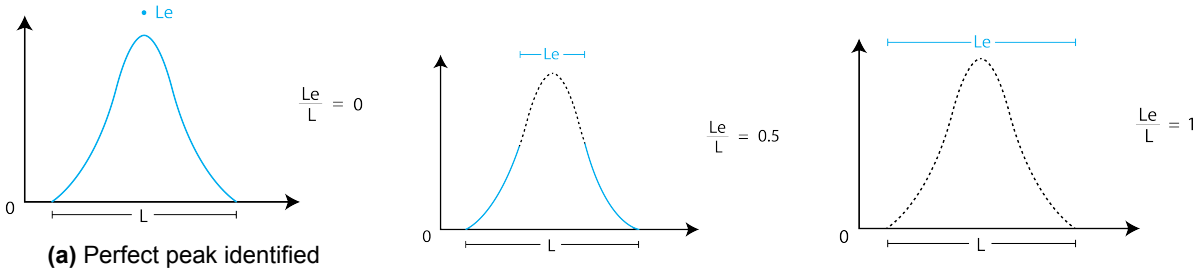

(a) Perfect peak identified ($Le/L = 0$)

(b) Partial data for the peak

(c) No data ($Le/L = 1$)

Figure 4.26: (Le/L) for different data quality

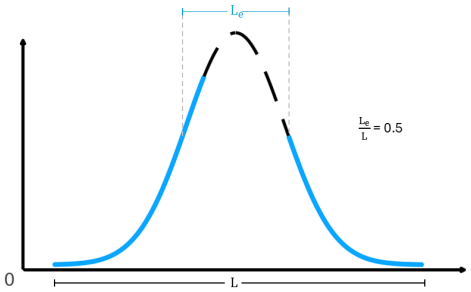

Figure 4.27: Unsymmetrical strain peak

We quantify the accuracy of the DFOS reconstruction using the relative absolute crack-width error in percentage. This is done by taking the crack widths obtained using DIC measurement as reference (4.3.

$$e_w = \min\left(1,\ \frac{|\hat{w}_{\mathrm{DFOS,\,interp}} - w_{\mathrm{DIC}}|}{w_{\mathrm{DIC}}}\right) * 100\% \tag{4.3}$$

4.4.1. Data selection

We selected one dominant crack per specimen in the constant-moment region (CMR). The selection criteria were:

i. The crack lies well outside the disturbed regions of the specimen.

ii. The crack is clearly identifiable in both DIC and DFOS.

iii. The crack remains prominent across most load stages up to yielding, with a visibly changing Le/L and a sufficiently large DIC crack width.

4.4.2. Results and Summary

For Specimen 2 (R4D8–DB), no crack satisfied all the criteria as mentioned in 4.4.1; therefore, this specimen is omitted from the analysis below. The observations from other specimens have been listed in Table 4.1 and plotted in Figure 4.28-Figure 4.30. We plot the missing-data ratio L_e/L on the x-axis and the normalized crack-width error e_w on the y-axis, one point per load stage. A rising trend indicates that wider gaps around the peak lead to larger crack-width error after interpolation.

Table 4.1: L_e/L summary with crack widths and relative absolute error

Specimen	Stage (kN)	L_e	L	L_e/L	w_{DIC}	w_{DFOS}	$e_w(\%)$
Specimen 1	40	9.8	35.35	0.277	29	33	13.7
	45	18.66	41	0.455	92	60	34.7
	50	18.5	45.9	0.40	117	77	34.1
	55	20.9	46.6	0.448	146	79	45.8
	60	23.7	49.3	0.48	209	98	53
Specimen 3	40	0	55	0	51	54	5.8
	45	3	51.9	0.057	77	80	3.8
	50	9	53.3	0.168	100	103	3
	55	24.7	56.09	0.44	132	104	21.2
	60	24.5	56.8	0.431	150	113	24.6
Specimen 4	50	9.1	42	0.216	62	62	0
	60	15	50	0.3	109	95	12.8
	70	29.9	51	0.586	138	110	20
	80	33	65	0.507	163	90	44.7
	90	29.9	55	0.543	189	113	40.2
	100	32.4	50	0.558	205	120	41.4
	110	32.4	60	0.54	234	136	41.8
	120	32.3	60.1	0.537	256	139	45.7

On the basis of these results, practical limits can be defined for the present configuration. For $L_e/L \leq 0.30$, the relative absolute error e_w is typically below 15 $\%$ and only rarely exceeds 25 $\%$. In this range, DFOS-derived crack widths are therefore considered *reliable*. Once $L_e/L > 0.40$, a substantial part of the crack-induced strain peak is missing and the relative error frequently reaches 30–50 $\%$; such cases are classified as *unreliable* in this thesis.

Specimen 1

The error increases clearly with the missing-data ratio. From $L_e/L \approx 0.27$ to 0.48, the normalized crack-width error e_w rises from about 14% to 53%. Around $L_e/L \gtrsim 0.40$, the error is already large ($\sim 35\%$), so interpolation becomes unstable well before $L_e/L = 0.5$ (Figure4.28).

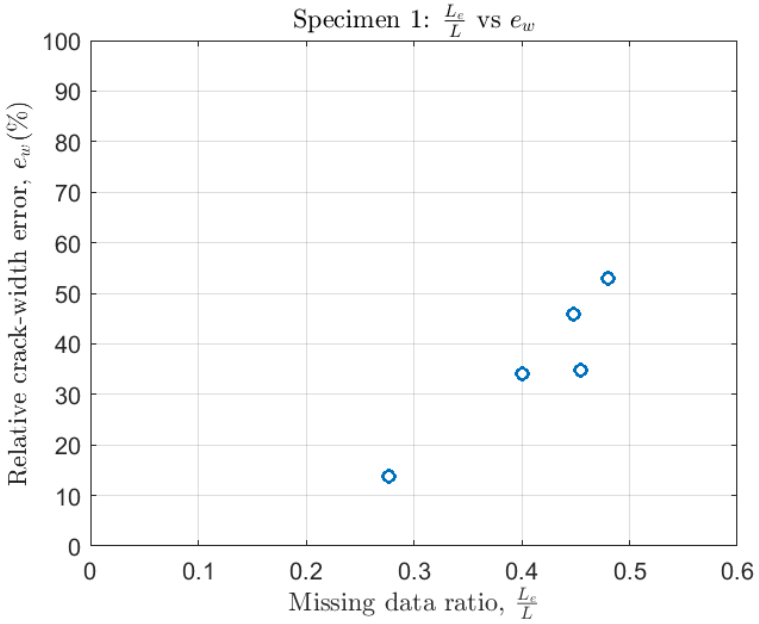

Figure 4.28: Specimen 1 (dominant crack): relative crack-width error (e_w) versus missing-data ratio (L_e/L).

Specimen 3

Small ratios give small errors and are usually observed at lower load stages and low crack widths. For $L_e/L \leq 0.17$, e_w is $\sim 3\%$. When L_e/L increases to about 0.43–0.44, e_w grows to $\sim 21\%$–25% (Figure 4.29). The trend is monotone but gentler than Specimen 1.

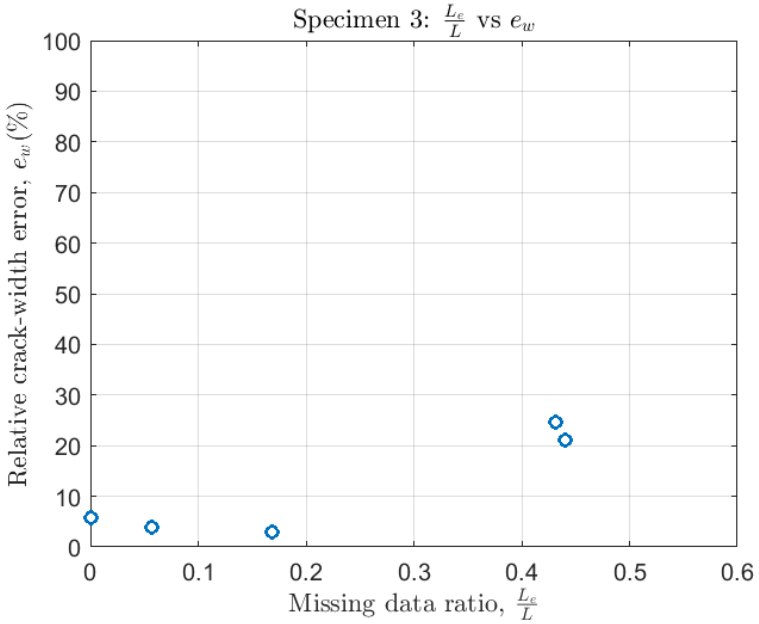

Figure 4.29: Specimen 3 (dominant crack): relative crack-width error (e_w) versus missing-data ratio (L_e/L).

Specimen 4

Specimen 4 had the highest yielding load and hence the error could be examined for higher loads (> 100 kN). At high L_e/L ratios the error is consistently large. A cluster at $L_e/L \approx 0.52$–0.56 shows $e_w \approx 40\%$–46%. Lower ratios (e.g., 0.30) have lower error ($\sim 13\%$). This indicates a strong loss of reliability once $L_e/L \gtrsim 0.5$.

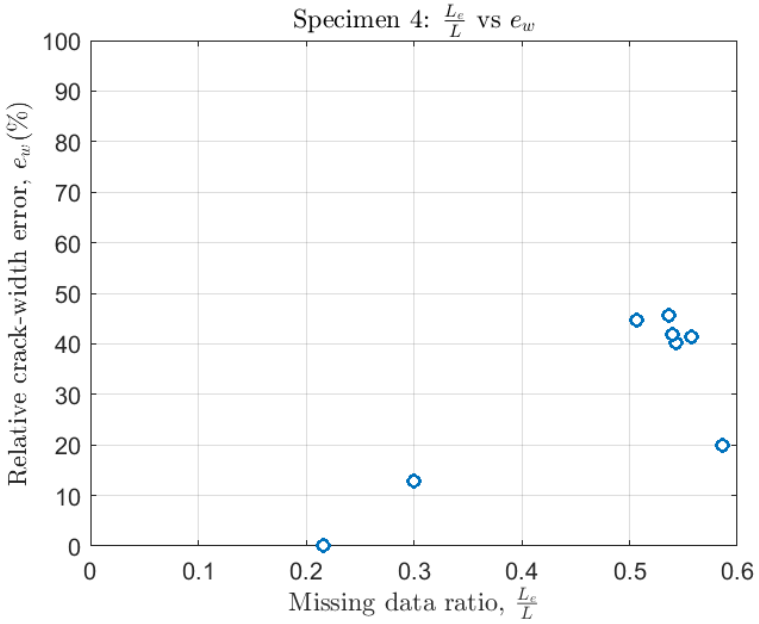

Figure 4.30: Specimen 4 (dominant crack): relative crack-width error (e_w) versus missing-data ratio (L_e/L).

Figure 4.28-Figure 4.30 shows the relation between the relative absolute crack-width error e_w and the missing-data ratio L_e/L for all beams where DFOS crack widths could be evaluated. A clear tendency can be observed: for $L_e/L \lesssim 0.3$, the majority of cracks exhibit relatively small errors, typically below 15–20%. In contrast, when the missing-data ratio exceeds about $L_e/L \approx 0.4$, the relative error often increases to 30–50%, with only a few cases remaining below 20%. After a point, the glass structure of the fibre core gets damaged to an extent that no new data can be obtained by the DFOS hence, as observed from the data, the L_e ratio stabilizes after a certain point. Although some scatter and occasional outliers are present, these results indicate that DFOS-based crack widths are most reliable when at least two-thirds of the crack-induced strain peak is captured by the sensor ($L_e/L \lesssim 0.3$), whereas crack-width estimates become increasingly uncertain and should be treated with caution once a substantial portion of the peak is missing ($L_e/L \gtrsim 0.4$).

4.5. Discussion

Crack detection and localisation

The inverted T-girder test confirms that DFOS is well-suited for crack detection and localisation. Distributed strain profiles along the fibre showed distinct tensile peaks that corresponded closely to flexural cracks in the flange and inclined shear cracks in the web, as independently identified by DIC. The evolution of the number and magnitude of these peaks with increasing load provided a detailed, one-dimensional “crack map” of the girder, which would be very difficult to obtain using conventional point sensors.

However, the T-girder also illustrated the sensitivity of crack signatures to installation quality. Non-uniform adhesive thickness, local debonding at surface imperfections and incomplete fibre pretension led to noisy regions, attenuated peaks and local data dropouts. These artefacts do not prevent qualitative identification of cracks, but they already suggest that quantitative crack-width estimation will be more demanding and will require a carefully controlled installation.

Accuracy of DFOS-derived crack widths

In the four-point bending beams, where the refined installation strategy and calibrated strain-transfer efficiency were used, DFOS-derived crack widths showed generally good agreement with DIC measurements. For most matched cracks, absolute errors were of the order of $0.05\,\mathrm{mm}$–$0.10\,\mathrm{mm}$, and the overall bias across all beams was small, indicating no strong systematic over- or underestimation. The scatter in relative error was larger for very small cracks ($w_{\mathrm{DIC}} \lesssim 0.1$ mm), where both DFOS

and DIC approach their resolution limits, but became more stable for cracks wider than approximately 0.2–0.3 mm.

These observations suggest that, under the present installation and processing conditions, DFOS can provide quantitatively reliable crack-width estimates for flexural cracks in the constant moment region, provided that (i) the strain-transfer efficiency is accounted for and (ii) the underlying strain peaks are sufficiently well captured.

Influence of missing data around crack peaks

The analysis of the missing-data ratio L_e/L clarifies how gaps in the DFOS signal at crack locations affect crack-width reliability. A clear tendency was observed for the relative absolute error e_w to increase with L_e/L. For $L_e/L \leq 0.30$, the majority of cracks exhibited relatively small errors, typically below 15–20% and only rarely exceeding 25%. In this range, DFOS-based crack widths can be considered reliable for structural assessment purposes.

Between $0.30 < L_e/L \leq 0.40$, and for corresponding errors in the range $25\% < e_w \leq 40\%$, the estimates enter a questionable zone where they may still provide useful indications but should be interpreted with caution. Once $L_e/L > 0.40$, a substantial portion of the crack-induced strain peak is missing and relative errors frequently reach 30–50%; such cases are classified as unreliable in this thesis. Although some scatter and occasional outliers are present, these thresholds provide a practical criterion: for the present configuration, at least two-thirds of the crack-induced strain peak should be captured by DFOS if crack-width estimates are to be trusted.

5

Discussion

This chapter synthesises the findings of the experimental work and discusses their implications for the use of Distributed Fibre Optic Sensing (DFOS) in existing concrete structures. The discussion is organised around the three sub-questions introduced in Chapter 1:

- Sub-question 1: Installation strategy for surface-bonded DFOS on concrete,
- Sub-question 2: Quantification of strain-transfer effects and recovery of the true concrete strain,
- Sub-question 3: Reliability of DFOS-based crack-width estimates.

Building on this synthesis, the final part of the chapter illustrates how the experimental insights can be translated into a practical DFOS monitoring concept for an existing prestressed concrete box-girder bridge (The Zeeland Bridge). This example is not a full design, but a conceptual application that shows how DFOS layouts and data-quality rules may be derived from laboratory calibration.

5.1. Implications for installation strategy

The inverted T-girder test and the four-point bending beams together provided a stepwise assessment of installation procedures for surface-bonded DFOS on concrete.

In the first, qualitative phase on the T-girder, the fibre was installed following generic manufacturer guidelines. The resulting strain maps were useful for visualising shear-crack patterns and for showing that DFOS can detect strain concentrations associated with crack initiation before visible cracking. However, the measurements also revealed several weaknesses of the initial installation: locally excessive adhesive thickness, small voids under the fibre, loss of fibre tension and local debonding. These defects did not prevent crack detection, but they introduced noise, occasional data gaps and clear variability in strain-transfer behaviour along the fibre.

In the second phase, these observations were used to refine the installation strategy for the four-point bending beams. Key changes included: stricter surface preparation (mechanical grinding and careful cleaning), control of adhesive thickness using a sliding-plate technique, systematic fibre pretension before curing, and clearer anchorage detailing. With this refined procedure, the DFOS profiles became much smoother, data loss was significantly reduced, and the strain-transfer efficiency stabilised along the bonded length.

From these combined observations, several practical conclusions can be drawn for surface-bonded DFOS on existing concrete structures:

- **Bondline control is essential.**

  Even for high-stiffness adhesives, local build-ups or voids in the bondline reduce strain transfer and increase the risk of missing data. Simple on-site tools to control adhesive thickness can

substantially improve performance. It is not strictly necessary that the bondline thickness should resemble a specific value at all points, but more importantly it should be uniform throughout the length of the fibre.

- **Fibre pretension is particularly important before bonding.**

  A lightly pre-tensioned fibre avoids local slack and improves contact in regions where the concrete surface is primarily in compression, which would otherwise tend to unload the fibre. Additionally, light pretension is required in the tension zone; however, excessive tensioning should be avoided, as it may damage the fibre during early loading stages and at low strain levels.

Overall, the experiments show that installation cannot be treated as a purely practical step that follows from a generic manual. Instead, it must be considered a design variable that is calibrated and verified for the specific DFOS type, adhesive and structural context. This directly addresses Sub-question 1 by demonstrating how an installation strategy can be derived and refined based on observed strain-transfer behaviour.

5.2. Strain-transfer calibration and true concrete strain

The four-point bending beams provided a controlled environment to quantify how much of the actual concrete surface strain is transmitted to the DFOS fibre. Across all specimens and load stages within the service range, DFOS consistently measured lower strain magnitudes than conventional strain gauges mounted next to the fibre. The ratio between DFOS strain and strain-gauge strain remained relatively constant, leading to a strain-transfer efficiency in the order of 40–50 %.

Two main causes explain this reduction:

- the presence of intermediate layers (fibre coating and adhesive), which deform in shear and act as a buffer between the concrete and the fibre core, and
- the surface-bonded configuration, which inherently provides less contact between the fibre's perimeter than embedded sensors.

Despite this reduction, the nearly constant ratio suggests that, for a given combination of fibre type, adhesive and installation method, a simple correction factor can be used to recover an estimate of the true concrete strain from DFOS measurements. This is particularly relevant for existing structures, where DFOS readings are often implicitly treated as the surface strain. The present results show that such an assumption is not valid without prior calibration.

For practical applications, this implies that:

- A project-specific strain-transfer calibration is required whenever a new fibre-adhesive system or installation procedure is introduced. Short laboratory tests on representative specimens can provide the necessary correction factor.
- Once calibrated, DFOS can resolve very small strain levels (of the order of a few tens of microstrain), provided that noise and temperature effects are controlled. These levels are comparable to strains expected in proof-load testing of bridges, making DFOS suitable for serviceability assessment when appropriately corrected.

This addresses Sub-question 2 by showing that strain-transfer effects can be quantified in a simple yet robust manner, and that corrected DFOS strains can be used as realistic estimates of the concrete surface strain in existing structures.

5.3. Reliability of DFOS-based crack-widths

Using the calibrated beams, crack widths were derived from DFOS strain profiles and compared with reference crack widths obtained from digital image correlation. Up to intermediate load levels (approximately $0.6\,P_y$), DFOS-based crack widths generally agreed well with DIC, both in terms of crack localisation and magnitude. At higher load stages, where cracks became more localised and strain gradients steeper, discrepancies increased.

A key factor in this loss of accuracy was the presence of missing or degraded strain peaks in the

DFOS profiles. To quantify this effect, an effective missing-data ratio L_e/L was introduced for each crack, representing the length of the interpolated gap relative to the crack influence length. Across all specimens, a clear trend emerged:

- **Low missing data ($L_e/L \leq 0.30$):** interpolation is reliable and the relative crack-width error e_w typically remains below about 15 %.
- **High missing data ($L_e/L > 0.40$):** errors often exceed 35 % and may become much larger. DFOS-only crack-width estimates in this regime should be flagged as provisional and cross-checked with an independent reference method wherever possible.

These findings lead to two main conclusions. First, DFOS is highly effective for **crack detection and localisation**: even when some data are missing, crack positions and patterns remain clearly identifiable from the strain profiles. Second, the **quantitative reliability of crack widths** depends strongly on data quality. A simple threshold in terms of L_e/L provides a practical, per-crack quality indicator that can be implemented in monitoring software to automatically flag potentially unreliable crack-width estimates.

Sub-question 3 is therefore answered by stating that DFOS-based crack widths are reliable within a defined range of missing-data ratios and loading levels, and by providing explicit criteria for judging when DFOS alone is sufficient and when additional reference measurements are advisable.

5.4. Application example: DFOS concept for an existing balanced cantilever bridge

The experimental results were finally translated into a conceptual DFOS monitoring layout for an existing prestressed concrete box-girder bridge, represented here by the Zeeland Bridge. Previous structural assessment of this bridge identified three main areas of concern: (i) limited moment capacity in the top slab under negative bending in several spans, (ii) a bottom slab location where the unity check approaches one, and (iii) several regions where the web shear capacity is exceeded or close to its limit. These are extended zones rather than isolated points, making DFOS an attractive option due to its distributed strain sensing over long distances.

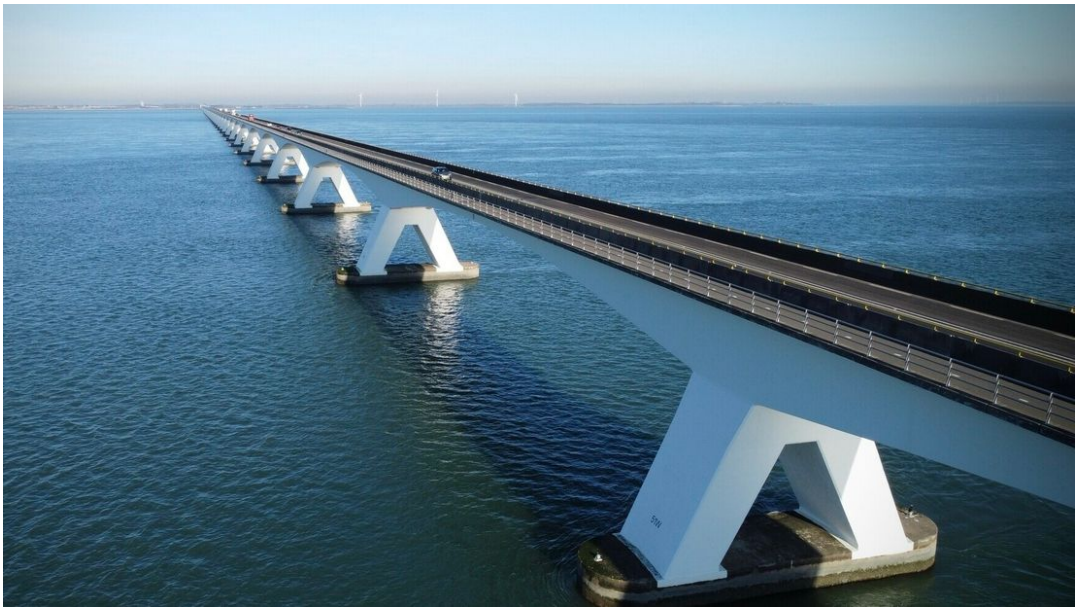

Figure 5.1: The Zeeland Bridge [64]

The Zeeland Bridge is a prestressed concrete box-girder bridge situated in the province of Zeeland, in the southwest of the Netherlands. It forms part of a network of major regional infrastructure works, which also includes the Westerscheldetunnel and the Oosterscheldekering storm-surge barrier. The bridge spans the Oosterschelde estuary, providing a vital connection between the islands of Noord-Beveland and Schouwen-Duiveland along the national road N256. Ownership and maintenance of the structure fall under the responsibility of the Province of Zeeland [65]. Construction of the Zeeland Bridge was carried out using the balanced-cantilever method between 1963 and 1965. Since its completion, the bridge has undergone several maintenance and rehabilitation programs to ensure its continued serviceability. An overall view of the structure is presented in Figure 5.1.

5.4.1. Bridge description and Structural Geometry

The Zeeland Bridge is a prestressed concrete box-girder structure composed of both fixed and movable parts. The total bridge length, including abutments, is approximately 5020 m, of which the fixed portion consists of 50 T-frames, each spanning 95 m, while the movable bascule span measures about 40 m.

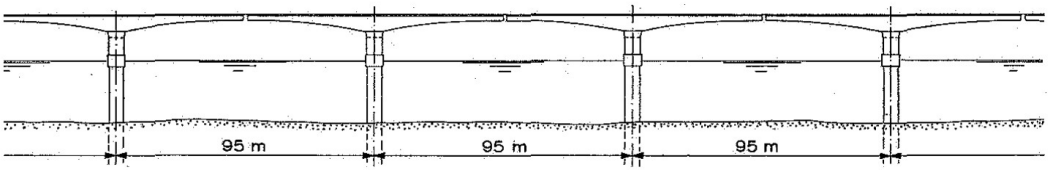

Figure 5.2: Longitudinal section of the Zeeland Bridge for a few spans [66]

5.4.2. Longitudinal Structural Assessment

To determine the most critical sections of the Zeeland Bridge in terms of bending and shear demand, existing calculation by Stoop (2024) [67] were used. The internal force distributions were analyzed along the longitudinal axis. In the study, the objective of these checks is not structural design verification, but to identify locations of high stress concentration where Distributed Fiber Optic Sensors (DFOS) would provide the most valuable strain information for long-term monitoring.

In the context of Distributed Fiber Optic Sensing (DFOS), the longitudinal direction of the bridge is of particular interest, as this technology enables continuous strain monitoring over extended distances along the structure. Unlike discrete sensors or point-based measurements, DFOS can capture the global strain distribution along the entire span, making it ideally suited for identifying variations in axial strain, flexural response, and potential cracking along the bridge length.

For this reason, the following section focuses on the longitudinal performance assessment of the Zeeland Bridge, based on the checks and analytical evaluations described in [67]. These analyses assess the stress state, reinforcement utilization, and prestressing efficiency in the longitudinal direction of the box girder, providing valuable insight into the structural behaviour most relevant to DFOS monitoring applications.

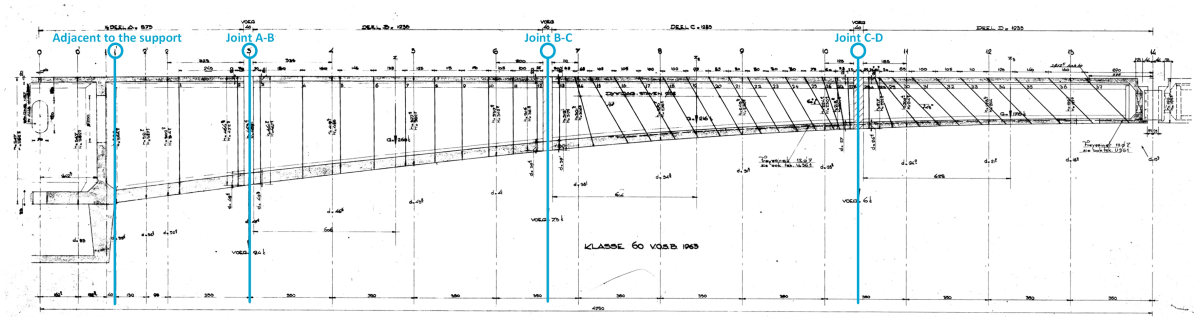

Figure 5.3: Cross-sections in the longitudinal section of the Zeeland Bridge [67]

5.4.3. Moment capacity of top and bottom slab

This check verifies whether the top slab in tension and the bottom slab in compression can resist the longitudinal bending effects at representative cross-sections: adjacent to a support and at construction joints A–B, B–C, and C–D within a cantilever. These locations are indicated in the original longitudinal section and are used here to identify critical monitoring regions for DFOS.

Figure 5.4 shows the specific locations along the bridge's longitudinal axis where this analysis is performed. The evaluation is conducted at four cross-sections: near the support and at the construction joints between different segment types within each cantilever, as illustrated in Figure 5.3.

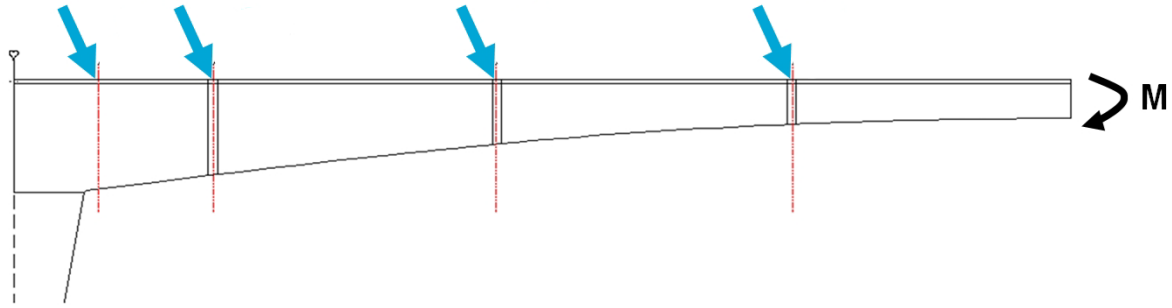

Figure 5.4: Check for moment capacity of the box girder's top and bottom slab [67]

5.4.3.1. Top slab (tension)

Table 5.1: Unity check: bending moment top slab with $\theta = 30°$ [67]

	M_{Ed} [MNm]	h' [m]	$d_{\text{top slab}}$ [m]	$d_{\text{bottom slab}}$ [m]	z [m]	F_{Ed} [MN]	ΔF_{Ed} [MN]	n [number]	$\sum F_p$ [MN]	U.C.
Adjacent to the support	317	5.44	0.20	0.53	5.08	62.46	13.86	143	81.30	0.94
Joint A–B	269	4.69	0.20	0.50	4.34	61.98	12.47	123	69.93	**1.06**
Joint B–C	126	3.18	0.20	0.39	2.89	43.67	8.14	87	49.46	**1.05**
Joint C–D	38	2.22	0.20	0.27	1.99	19.14	4.33	45	25.58	0.92

Table 5.2: Unity check: bending moment top slab with $\theta = 21.8°$ [67]

Location	M_{Ed} [MNm]	h' [m]	$d_{\text{top slab}}$ [m]	$d_{\text{bottom slab}}$ [m]	z [m]	F_{Ed} [MN]	ΔF_{Ed} [MN]	n [number]	$\sum F_p$ [MN]	U.C. [-]
Adjacent to the support	317	5.44	0.20	0.53	5.08	62.46	20.00	143	81.30	**1.01**
Joint A–B	269	4.69	0.20	0.50	4.34	61.98	18.00	123	69.93	**1.14**
Joint B–C	126	3.18	0.20	0.39	2.89	43.67	11.75	87	49.46	**1.12**
Joint C–D	38	2.22	0.20	0.27	1.99	19.14	6.25	45	25.58	0.99

5.4.3.2. Bottom slab (compression)

Table 5.3: Unity check: bending moment bottom slab [67]

	M_{Ed} [MNm]	F_{Ed} [MN]	b' [mm]	$d_{\text{bottom slab}}$ [mm]	f_{cd} [N/mm^2]	$N_{Rd,c}$ [MN]	U.C.
Adjacent to the support	317	62.46	6412	530	20	67.97	0.92
Joint A–B	269	61.98	6524	500	20	65.24	0.95
Joint B–C	126	43.67	6720	390	20	52.42	0.83
Joint C–D	38	19.14	6850	270	20	36.99	0.52

5.4.4. Shear capacity of the webs

This check verifies whether the webs can resist the transverse shear effects at representative cross-sections: adjacent to a support and at construction joints A–B, B–C, and C–D within a cantilever. These locations are indicated in the original longitudinal section (see Figure 5.3 and are used here to identify critical DFOS monitoring regions in the webs. The evaluation is conducted at four cross-sections—near the support and at the construction joints between different segment types within each cantilever—as illustrated in Figure 5.5.

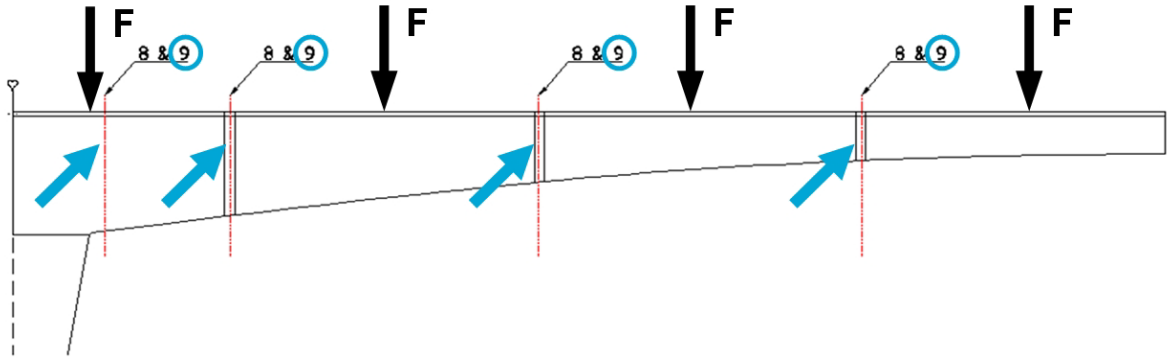

Figure 5.5: Check for shear force capacity of the box girder's webs [67]

Table 5.4: Unity check shear force capacity webs (per web) with $\theta = 30°$ and C30/37

	$V_{Ed,tot}$ [MN]	$V_{Rd,s}$ [MN]	V_{ccd} [MN]	V_{td} [MN]	$V_{Rd,c}$ [MN]	V_{Rd} [MN]	$V_{Rd,\max}$ [MN]	U.C.
Adjacent to the support	8.89	2.80	4.15	0	0.76	7.71	9.51	**1.15**
Joint A–B	8.09	2.39	3.97	0	0.67	7.03	8.04	**1.15**
Joint B–C	5.33	2.87	2.25	0	0.48	5.60	5.01	**1.06**
Joint C–D	2.99	2.99	0.42	0	0.36	3.77	3.95	0.79

5.4.5. Interpretation of the results

The recalculation by Stoop [67] provides clear insight into the current condition of the Zeeland Bridge and highlights regions that warrant priority monitoring. The key observations are:

1. **Top slab (negative bending):** At several locations the unity check (U.C.) for bending in the top slab is high and exceeds 1. In these regions, tension in the top fibre is critical and should be monitored closely. A continuous, distributed sensing system such as DFOS is well-suited for this purpose, particularly during proof-load tests in which allowable strain thresholds can be predefined and directly checked against DFOS measurements.
2. **Bottom slab (positive bending):** The moment capacity of the bottom slab is currently adequate, with U.C. < 1 at most assessed sections. However, at Joint A–B the U.C. approaches unity and warrants precautionary monitoring. The laboratory experiments have shown that, after strain-transfer calibration, surface-bonded DFOS can also provide reliable measurements of compressive strains, making it a suitable option for this zone as well.
3. **Web shear:** In several regions the shear capacity of the box-girder webs is at or above acceptable limits (U.C. ≥ 1). These webs represent a primary concern and require targeted monitoring of shear cracking. The inverted T-girder test demonstrated that DFOS can detect and localise inclined shear cracks with high spatial resolution, indicating that a similar DFOS layout in the webs of the Zeeland Bridge would be effective for tracking the development of shear-related damage.

Given these findings, continuous monitoring has become essential. Because the areas of concern are extended regions rather than single points, DFOS is a promising solution due to its distributed, high-resolution strain sensing over long lengths.

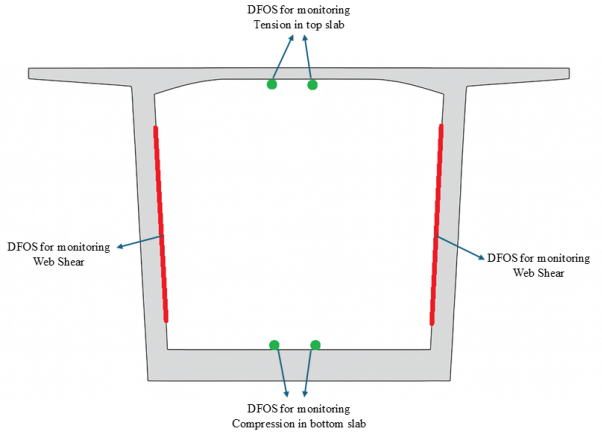

Figure 5.6: Sensor placement in cross-section view

5.4.6. Sensor topology for flexure

As discussed before, in the longitudinal direction, the top slab is critical with Unity check exceeding 1 at three sections. Hence, these regions are to be prioritized for monitoring using DFOS. The bottom slab of is not critical in the longitudinal direction, however, the concrete in the bottom slab is prone to deterioration and hence to avoid unexpected behavior it is beneficial to also monitor the compression in the bottom slab. Two sensors are placed in the middle of the box girder section at the top and the bottom (Figure 5.7). This is done in order to ensure functionality if one of the sensors unexpected fails or gives spurious measurements. Another benefit of placing the sensors in this manner is that, it can help us to identify curvature, which is very crucial in identifying other parameters like deflection and bending moment of the bridge.

While flexure monitoring is well served by two backbone slab lines, shear behaviour in the webs is more heterogeneous and demands tailored topologies. The next subsection therefore, presents five alternative DFOS strategies for web shear.

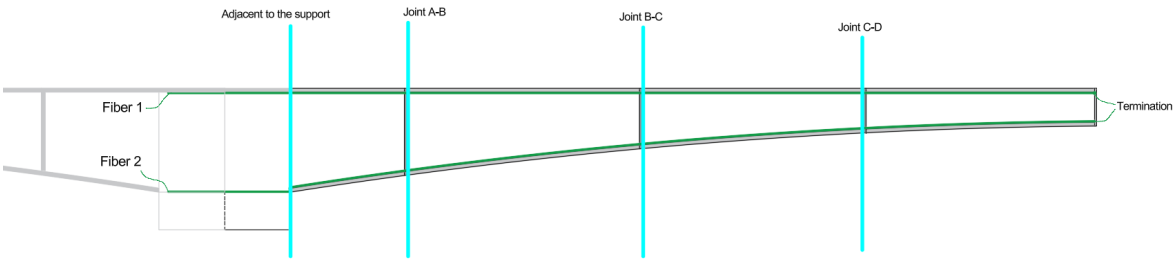

Figure 5.7: Sensor layout for flexure monitoring

5.4.7. Sensor topology for web shear

1. Strategy 1

   This topology follows the sensor layout used in the qualitative analysis experiment (see Chapter 3). In those tests it successfully identified and localised shear cracks on the concrete web;

notably, DFOS registered small strain peaks that indicated impending crack formation even before visible cracks were captured by the DIC system. A practical drawback is total path length. The continuous run can approach $\sim 75\,\mathrm{m}$. For Rayleigh backscattering interrogators, the effective single run range is typically ≈ 50–$70\,\mathrm{m}$, which may challenge signal quality

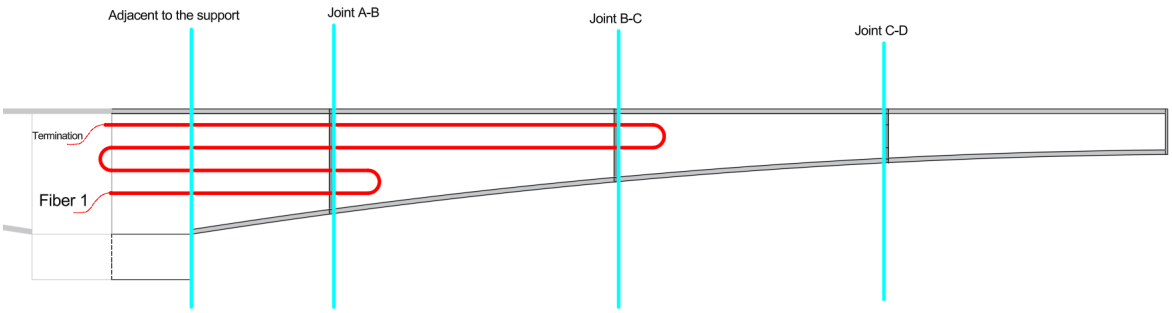

Figure 5.8: Sensor layout for web shear : Strategy 1

2. Strategy 2

This topology addresses the length restriction by splitting the web sensor layout into multiple laps, each terminated at the end of the critical section (Joint B-C) and connected to the interrogator as an individual channel. Each lap covers a defined web window (e.g., ± 12–$20\,\mathrm{m}$ from the support) so that no single continuous run exceeds the interrogator's effective Rayleigh range.

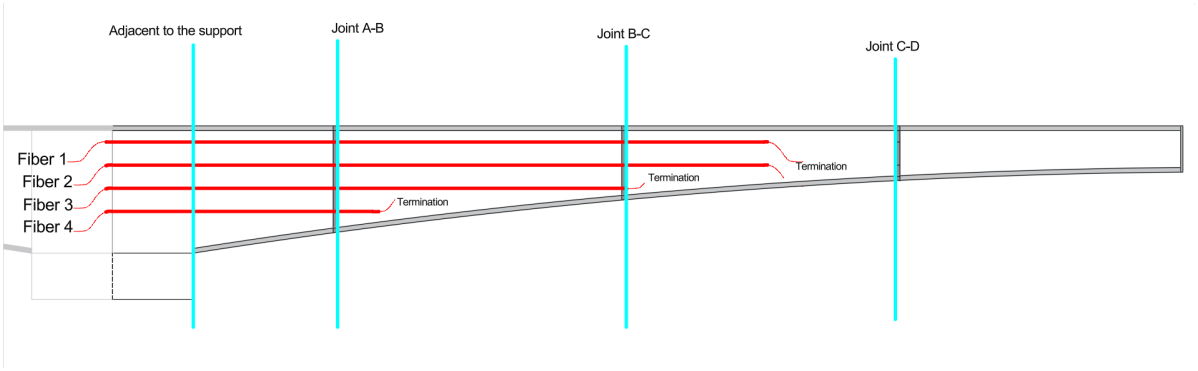

Figure 5.9: Sensor layout for web shear: Strategy 2

3. Strategy 3

An early field application on a reinforced–concrete bridge by Regier and Hoult [53] (Black River Bridge, Ontario) demonstrated an inclined "chevron" routing for web monitoring. This strategy replicates that concept. The total fibre path is kept to $\sim 50\,\mathrm{m}$ to remain within typical Rayleigh–backscatter interrogator ranges. The fibre runs in repeated 45° inclined segments across the web so that it intersects likely diagonal–tension crack paths.

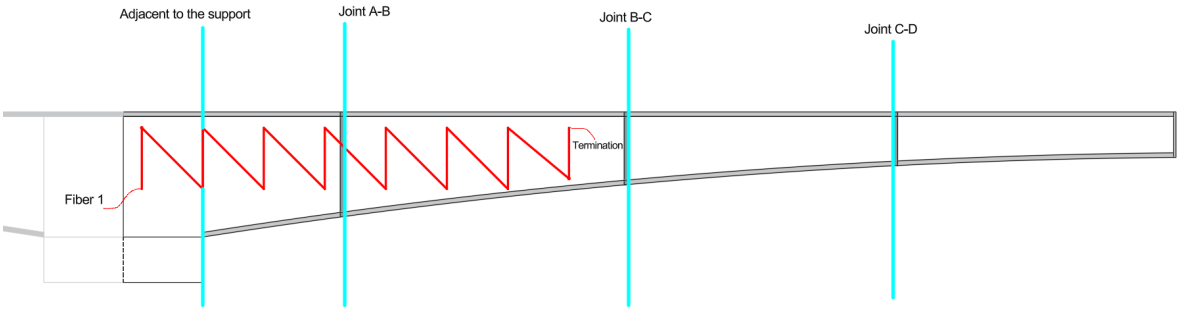

Figure 5.10: Sensor layout for web shear : Strategy 3

4. Strategy 4

   Because the maximum cantilever shear demand occurs near the supports, this strategy concentrates instrumentation within a short window adjacent to the bearing. Similar web instrumentation has been used on the Kalix Bridge in Sweden [68] and mirrors the approach adopted in our qualitative experiment (see Chapter 3).

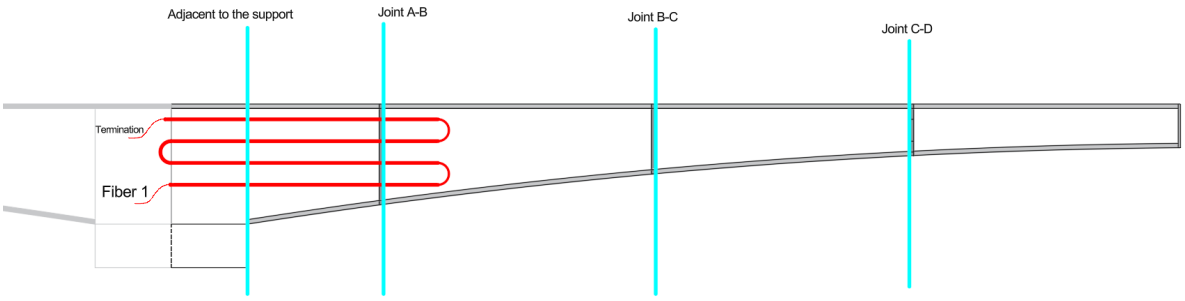

Figure 5.11: Sensor layout for web shear : Strategy 4

5. Strategy 5

   To enhance the spatial resolution of the shear–crack pattern, this topology uses a dense orthogonal grid of DFOS that runs across the web. The approach is adapted from laboratory work by Rodriguez et al. [52], which showed strong performance in resolving shear–cracks and estimating crack angles.

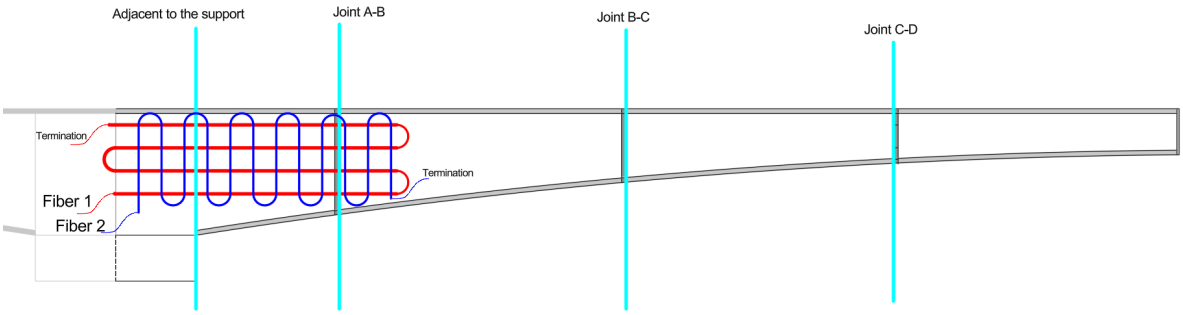

Figure 5.12: Sensor layout for web shear : Strategy 5

The proposed sensor topology follows directly from the monitoring objectives observed from the previous assessment results. Longitudinal fibres along the inner faces of the top and bottom slabs provide strains with minimal routing complexity, while web-oriented runs in selected cantilever panels target the most likely diagonal strain paths.

In summary, the case study validates that a DFOS system designed around balanced-cantilever mechanics, installed with bondline discipline, and governed by explicit data-quality rules can deliver reliable, high-resolution strain intelligence on a complex, long-span concrete bridge. The approach links laboratory calibration to field observables, balances sensitivity with robustness, and provides a practical path to long-term monitoring of strains and cracking.

5.5. Overall implications for DFOS in existing concrete structures

The findings from this study highlight the promising potential of DFOS for application in existing bridge infrastructure. Notably, the system demonstrated the ability to detect strain peaks associated with crack initiation prior to the appearance of visible surface cracks. This early detection capability is particularly valuable for monitoring shear and flexure-critical regions, where timely identification of damage can significantly enhance structural assessment and maintenance strategies. These results support the integration of DFOS as a reliable tool for proactive condition monitoring and performance evaluation of ageing bridge structures, provided that three conditions are met:

1. Installation strategies must be explicitly designed, tested and documented rather than adopted directly from generic guidelines.
2. Strain-transfer behaviour must be calibrated so that DFOS readings are interpreted as corrected estimates of the true concrete strain.
3. Crack-width estimation procedures must incorporate objective data-quality metrics, such as the missing-data ratio L_e/L, to distinguish between reliable and uncertain results.

Existing bridge structures may already exhibit cracking prior to DFOS installation. Consequently, DFOS can only detect changes in crack width post-installation, expressed as

$$\Delta w_{\mathrm{DFOS}} = w(t) - w(t_0).$$

To estimate the absolute crack width, this change must be added to the pre-existing crack width w_0, which should be measured using an independent method (e.g. crack width ruler). The total crack width is then given by

$$w_{\mathrm{abs}} = w_0 + \Delta w_{\mathrm{DFOS}}.$$

Given that many existing bridges have been in service for extended periods, micro-cracks may already be present, resulting in relatively small crack width variations. The results demonstrate that DFOS is capable of detecting such low-magnitude changes with high precision. Crack widths as small as 30 μm were reliably identified and showed strong agreement with reference measurements obtained via Digital Image Correlation (DIC).

Under these conditions, DFOS offers unique capabilities: high-resolution crack localisation along long lengths, early detection of damage, and the possibility to link distributed strain fields to structural behaviour of complex elements such as box-girder bridges. The next chapter builds on this discussion to formulate concise answers to the research questions and to provide recommendations for further research and future field implementations.

6

Conclusions and Recommendations

This chapter summarises the main findings of the thesis and answers the research questions introduced in Chapter 1. The experimental work on an inverted T-girder and four-point bending beams, together with the discussion and conceptual bridge application in Chapter 5, provide the basis for drawing conclusions on the use of Distributed Fibre Optic Sensing (DFOS) for strain and crack-width monitoring in existing concrete structures. On this basis, recommendations are formulated for practical implementation and for future research.

6.1. Research Questions

The main research question guiding this thesis was formulated as:

> *How can Distributed Fibre Optic Sensing (DFOS) be effectively utilized for strain and crack-width monitoring in existing concrete structures?*

To address this question, three sub-questions were formulated. The conclusions for each are summarised below, followed by an overall answer to the main research question.

1. *What installation strategy for surface-bonded Distributed Fibre Optic Sensors on concrete ensures reliable bonding and effective strain transfer?*

   The inverted T-girder test showed that applying generic guidelines for surface-bonded DFOS does not automatically lead to a reliable installation. Non-uniform adhesive thickness, small voids, local fibre slack and debonding resulted in noisy strain profiles, data gaps and spatially variable strain-transfer behaviour. While crack detection was still possible, these issues limited the suitability of the data for quantitative use.

   Based on these observations, a refined installation strategy was developed and implemented in the four-point bending beams. The main elements of this strategy are:

   - Rigorous and continuous surface preparation (grinding, cleaning and treatment of surface defects) along the full fibre route;
   - Controlled bondline thickness using a consistent application technique for the epoxy adhesive, avoiding local build-ups and voids; and
   - Light, standardised pretension of the fibre before bonding to eliminate slack, particularly in compression zones.

   With this refined strategy, DFOS profiles became significantly smoother, data loss decreased, and strain-transfer efficiency stabilised along the bonded length. The refined installation strategy, therefore, provides a practical answer to Sub-question 1: effective use of surface-bonded DFOS on concrete requires explicitly designed and calibrated installation procedures, rather than a direct adoption of generic guidelines.

2. *How can strain-transfer effects be quantified so that DFOS-measured strains can be converted into accurate estimates of the concrete surface strains?*

   The four-point bending beams allowed a direct comparison between DFOS strains and strains measured by electrical strain gauges bonded next to the fibre in both tension and compression zones. In the uncracked loading range, DFOS consistently measured lower strain magnitudes than the strain gauges, but the ratio between the two remained almost constant for a given installation.

   For the surface-bonded configuration studied in this thesis, the ratio between DFOS strain and concrete surface strain was found to be of the order of 0.4–0.5 in both tension and compression. This ratio was only weakly affected by the different adhesives used in the compression zone, indicating that the presence of intermediate layers (coating and adhesive, along with the contact perimeter of the fibre is the main cause of strain reduction, rather than the exact adhesive stiffness within the tested range.

   On this basis, a simple strain-transfer efficiency factor (STE) was defined and calibrated. Correcting DFOS strains by the inverse of this factor yields estimates of the concrete surface strain that agree well with strain-gauge measurements in the uncracked range. The study thus shows that strain-transfer effects can be quantified experimentally with a relatively simple procedure and that DFOS strains can be used as realistic estimates of concrete strain, provided that a project-specific STE is determined.

   This addresses Sub-question 2 by demonstrating that strain-transfer effects do not prevent quantitative use of DFOS, but they must be measured and explicitly accounted for.

3. *How reliable are crack widths obtained from Distributed Fibre Optic Sensing for reinforced concrete members?*

   Crack widths were derived from DFOS strain profiles in the constant moment region of the four-point bending beams, using a procedure based on integration of corrected concrete strains around crack-induced peaks. The results were compared with reference crack widths from Digital Image Correlation.

   In general, DFOS was able to detect and locate almost all cracks visible in DIC. For cracks wider than approximately 0.2–0.3 mm, DFOS-based crack widths agreed with DIC within absolute errors of about 0.05–0.10 mm and showed only a small overall bias, indicating that there is no strong tendency towards systematic over- or underestimation.

   However, the accuracy of DFOS crack widths was strongly influenced by missing or degraded data at crack locations. This effect was captured through a missing-data ratio L_e/L, which represents the length of the interpolated or missing signal relative to the effective influence length of the crack peak. Across all beams, a clear tendency was observed:

   - for $L_e/L \leq 0.30$, most cracks had relative absolute errors below about 15–20 %;
   - for $L_e/L > 0.40$, errors frequently reached 35–50 % or more.

   On this basis, DFOS-derived crack widths are considered reliable in this thesis when $L_e/L \leq 0.30$, questionable when $0.30 < L_e/L \leq 0.40$, and unreliable when $L_e/L > 0.40$. These thresholds provide a simple quality indicator that can be applied on a crack-by-crack basis in monitoring applications. However, this is also highly dependent on the method of interpolation used. Hence, for a different type of fibre, adhesive used, and interpolation method used, this ratio (L_e) might be different.

   Sub-question 3 is therefore answered by stating that DFOS-based crack widths can be quantitatively reliable, but only when strain-transfer is calibrated, cracks are above a practical resolution limit, and the missing-data ratio around each crack remains below a defined threshold.

6.1.1. Main research question

Combining the answers to the three sub-questions, the main research question can be addressed as follows:

DFOS can be effectively utilised for strain and crack-width monitoring in existing concrete structures when it is implemented as a calibrated monitoring system rather than a plug-and-play sensor. This requires (i) an installation strategy that ensures a uniform and robust bond between fibre and concrete, (ii) an experimentally derived strain-transfer efficiency factor to convert DFOS strains to concrete surface strains, and (iii) crack-width estimation procedures that incorporate data-quality metrics such as the missing-data ratio L_e/L to distinguish reliable from uncertain crack-width estimates. Under these conditions, DFOS provides high-resolution information on strain distribution and crack development that cannot be obtained with conventional point sensors alone.

6.2. Recommendations for practical implementation

Based on the findings of this thesis, the following recommendations are made for engineers and practitioners considering DFOS for monitoring existing concrete structures.

Installation and system design

- Treat DFOS installation as a design task. Define fibre routes, surface preparation, adhesive type and anchorage details explicitly, and document them in the monitoring plan.
- Carry out small-scale trial installations on representative concrete surfaces before large-scale deployment, in order to verify bond quality and refine practical procedures.
- Use high-stiffness adhesives (such as structural epoxies) for quantitative strain and crack-width monitoring, and control bondline thickness along the entire fibre route.
- Avoid sharp bends, abrupt direction changes and unrestrained transitions near anchorages. Wherever possible, keep fibre routing smooth and continuous, especially in regions where crack formation is expected.

Calibration and data processing

- Perform a project-specific strain-transfer calibration by comparing DFOS strains with co-located strain gauges in a representative element or zone, and derive an effective STE for the adopted fibre/adhesive/installation combination.
- Implement a standard pre-processing pipeline for DFOS data that includes masking of obvious spike artefacts, conservative interpolation of short gaps and minimal spatial filtering along the fibre.
- In crack-width calculation, correct DFOS strains using the calibrated STE and evaluate the missing-data ratio L_e/L around each crack. Use this ratio as an automatic quality flag for crack-width estimates.

Use of DFOS crack widths in assessment

- Use DFOS primarily as a tool for detailed crack detection and localisation along long lengths of an element.
- Treat DFOS crack widths as reliable when $L_e/L \leq 0.30$ and as qualitative indicators only when $L_e/L > 0.40$. In the intermediate range, combine DFOS results with visual inspection or local reference sensors.
- When designing DFOS layouts for bridges or other large structures, place fibres in regions where conventional analysis indicates low reserve capacity (for example webs with high shear utilisation or slabs in negative bending), and use the laboratory-calibrated STE and L_e/L thresholds as initial interpretation rules.
- In a real structure, it is quite challenging to work with the fragile optical fibre that is used in the laboratory test. Hence, a more robust fibre should be used that can withstand harsh environments and exposure conditions.

6.3. Recommendations for future research

The work in this thesis has been limited to laboratory-scale members with surface-bonded DFOS and short-term loading. Several topics deserve further investigation before the proposed approaches can be generalised to a wider range of structures and conditions.

- **Long-term and cyclic behaviour.** The present experiments were monotonic and short in duration. The influence of fatigue loading, shrinkage, creep and environmental effects on strain-transfer efficiency, bond durability and crack-width estimation should be studied in long-term tests.
- **Pre-existing cracks and repair situations.** Existing concrete structures often contain pre-existing cracks at the time of DFOS installation. Future work should investigate how surface-bonded DFOS respond to such cracks, how initial crack widths can be combined with DFOS-based width changes and how repair materials influence strain transfer.
- **Field validation on bridges.** Full-scale field applications on bridges, combined with independent reference measurements (for example displacement monitoring, strain gauges or periodic DIC campaigns), are needed to validate the laboratory-based STE factors and L_e/L thresholds under real environmental and operational conditions.
- **Improved signal processing and automated interpretation.** The crack detection and crack-width algorithms used in this thesis can be extended with more advanced peak-tracking and pattern-recognition techniques. Automated classification of cracks based on DFOS data quality and structural relevance would further support practical decision-making.
- **Alternative fibre and adhesive systems.** The present study focused on a specific polyimide-coated fibre and a limited set of adhesives. Systematic testing of other fibre types, coatings, cables and bonding materials would help to identify combinations that optimise both strain-transfer efficiency and robustness for field use.

6.4. Closing statement

This thesis has shown that DFOS, when installed and interpreted with due care, can significantly enhance the monitoring of strain and cracking in existing concrete structures. By explicitly addressing installation strategy, strain-transfer calibration and crack-width reliability, the work provides a structured framework for moving DFOS from a promising technology to a practical tool in structural assessment and asset management.

The laboratory-calibrated procedures developed in this study, combined with disciplined installation and clear data-quality rules, offer a transferable basis for DFOS applications on real structures. The illustrative example of the Zeeland Bridge demonstrates how the proposed workflows and sensor layouts can be translated into a monitoring concept for a prestressed concrete box-girder bridge, while still allowing for complementary measurements and project-specific constraints. Together, the conclusions and recommendations provide a coherent roadmap—from design to interpretation—for using DFOS as a long-term decision-support tool for the safety, serviceability and life extension of existing concrete structures.

References

[1] D. I. Branko Glisic, *Fiber Optic Methods For Structural Health Monitoring*. 2007.

[2] M. Weisbrich, D. Messerer, and K. Holschemacher, "The Challenges and Advantages of Distributed Fiber Optic Strain Monitoring in and on the Cementitious Matrix of Concrete Beams", en, *Sensors*, vol. 23, no. 23, p. 9477, Nov. 2023, Publisher: MDPI AG, ISSN: 1424-8220. DOI: 10.3390/s23239477. Accessed: Jul. 24, 2025. [Online]. Available: https://www.mdpi.com/1424-8220/23/23/9477.

[3] A. Reshak, M. Shahimin, S. Murad, and S. Azizan, "Simulation of Brillouin and Rayleigh scattering in distributed fibre optic for temperature and strain sensing application", en, *Sensors and Actuators A: Physical*, vol. 190, pp. 191–196, Feb. 2013, Publisher: Elsevier BV, ISSN: 0924-4247. DOI: 10.1016/j.sna.2012.11.034. Accessed: Jul. 24, 2025. [Online]. Available: https://linkinghub.elsevier.com/retrieve/pii/S0924424712007157.

[4] T. Howiacki, R. Sieńko, Ł. Bednarski, and K. Zuziak, "Crack Shape Coefficient: Comparison between Different DFOS Tools Embedded for Crack Monitoring in Concrete", en, *Sensors*, vol. 23, no. 2, p. 566, Jan. 2023, Publisher: MDPI AG, ISSN: 1424-8220. DOI: 10.3390/s23020566. Accessed: Jul. 24, 2025. [Online]. Available: https://www.mdpi.com/1424-8220/23/2/566.

[5] Ł. Bednarski, R. Sieńko, T. Howiacki, and K. Zuziak, "The Smart Nervous System for Cracked Concrete Structures: Theory, Design, Research, and Field Proof of Monolithic DFOS-Based Sensors", en,

[6] C. G. Berrocal, I. Fernandez, and R. Rempling, "Crack monitoring in reinforced concrete beams by distributed optical fiber sensors", en, *Structure and Infrastructure Engineering*, vol. 17, no. 1, pp. 124–139, Jan. 2021, ISSN: 1573-2479, 1744-8980. DOI: 10.1080/15732479.2020.1731558. Accessed: Aug. 11, 2025. [Online]. Available: https://www.tandfonline.com/doi/full/10.1080/15732479.2020.1731558.

[7] H. Wenzel, *Health Monitoring of Bridges*. John Wiley & Sons, Ltd., 2009, ISBN: 9780470031735. DOI: 10.1002/9780470740170.ch2. [Online]. Available: https://onlinelibrary.wiley.com/doi/abs/10.1002/9780470740170.

[8] A. Bassil, X. Chapeleau, D. Leduc, and O. Abraham, "Concrete Crack Monitoring Using a Novel Strain Transfer Model for Distributed Fiber Optics Sensors", en, *Sensors*, vol. 20, no. 8, p. 2220, Apr. 2020, Publisher: MDPI AG, ISSN: 1424-8220. DOI: 10.3390/s20082220. Accessed: Jul. 24, 2025. [Online]. Available: https://www.mdpi.com/1424-8220/20/8/2220.

[9] K. Kishida, Y. Yamauchi, and A. Guzik, "Study of optical fibers strain-temperature sensitivities using hybrid Brillouin-Rayleigh system", en, *Photonic Sensors*, vol. 4, no. 1, pp. 1–11, Mar. 2014, Publisher: Springer Science and Business Media LLC, ISSN: 1674-9251, 2190-7439. DOI: 10.1007/s13320-013-0136-1. Accessed: Jul. 24, 2025. [Online]. Available: http://link.springer.com/10.1007/s13320-013-0136-1.

[10] T. Howiacki, R. Sieńko, and Ł. Bednarski, "Structural concrete measurements: New distributed approach for standard specimens", en, *Measurement*, vol. 235, p. 115 003, Aug. 2024, Publisher: Elsevier BV, ISSN: 0263-2241. DOI: 10.1016/j.measurement.2024.115003. Accessed: Jul. 24, 2025. [Online]. Available: https://linkinghub.elsevier.com/retrieve/pii/S0263224124008881.

[11] C. J. Larosche, "Types and causes of cracking in concrete structures", pp. 57–83, 2009. DOI: 10.1533/9781845697037.1.57.

[12] X. Zhang, L. Long, W. Broere, and X. Bao, “Smart sensing of concrete crack using distributed fiber optics sensors: Current advances and perspectives”, en, *Case Studies in Construction Materials*, vol. 22, e04493, Jul. 2025, Publisher: Elsevier BV, ISSN: 2214-5095. DOI: 10.1016/j.cscm.2025.e04493. Accessed: Jul. 24, 2025. [Online]. Available: https://linkinghub.elsevier.com/retrieve/pii/S2214509525002918.

[13] S. B. Lin and Y. J. Wang, “Crack-depth estimation in concrete elements using ultrasonic shear-horizontal waves”, *Journal of Performance of Constructed Facilities*, vol. 34, no. 4, 2020. DOI: 10.1061/(ASCE)CF.1943-5509.0001473.

[14] W. Jin, “Multiplexed FBG sensors and their applications”, en,

[15] D. Inaudi et al., “SOFO: Structural Monitoring with Fiber Optic Sensors”, in *Monitoring and Safety Evaluation of Existing Concrete Structures*, Fédération Internationale du Béton (FIB), Vienna, Austria, Feb. 1999, pp. 1–13.

[16] TATSUTA Electric Wire & Cable Co., Ltd. “Fiber bragg gratings (fbg)”. Accessed: 2025□08□07.

[17] A. Barrias, G. Rodriguez, J. R. Casas, and S. Villalba, “Application of distributed optical fiber sensors for the health monitoring of two real structures in Barcelona”, en, *Structure and Infrastructure Engineering*, vol. 14, no. 7, pp. 967–985, Jul. 2018, Publisher: Informa UK Limited, ISSN: 1573-2479, 1744-8980. DOI: 10.1080/15732479.2018.1438479. Accessed: Jul. 24, 2025. [Online]. Available: https://www.tandfonline.com/doi/full/10.1080/15732479.2018.1438479.

[18] Information Gatekeepers Inc., *Photonic sensor consortium market survey report*, https://www.igigroup.com/st/pages/photonic_sensor_report.html#Anchor-Overview-17691, Accessed: 2025□08□07, n.d.

[19] A. Barrias, J. R. Casas, and S. Villalba, “Distributed optical fiber sensors in concrete structures: Performance of bonding adhesives and influence of spatial resolution”, en,

[20] M. Herbers, B. Richter, D. Gebauer, M. Classen, and S. Marx, “Crack monitoring on concrete structures: Comparison of various distributed fiber optic sensors with digital image correlation method”, en, *Structural Concrete*, vol. 24, no. 5, pp. 6123–6140, Oct. 2023, Publisher: Wiley, ISSN: 1464-4177, 1751-7648. DOI: 10.1002/suco.202300062. Accessed: Jul. 24, 2025. [Online]. Available: https://onlinelibrary.wiley.com/doi/10.1002/suco.202300062.

[21] O. Fischer, S. Thoma, and S. Crepaz, “Distributed fiber optic sensing for crack detection in concrete structures”, en, *Civil Engineering Design*, vol. 1, no. 3-4, pp. 97–105, Sep. 2019, Publisher: Wiley, ISSN: 2625-073X, 2625-073X. DOI: 10.1002/cend.201900008. Accessed: Jul. 24, 2025. [Online]. Available: https://onlinelibrary.wiley.com/doi/10.1002/cend.201900008.

[22] Ł. Bednarski, R. Sieńko, T. Howiacki, and K. Badura, “Thermal compensation of monolithic distributed fibre optic sensors: From the lab to the field”, en, *Measurement*, vol. 238, p. 115 280, Oct. 2024, Publisher: Elsevier BV, ISSN: 0263-2241. DOI: 10.1016/j.measurement.2024.115280. Accessed: Jul. 24, 2025. [Online]. Available: https://linkinghub.elsevier.com/retrieve/pii/S0263224124011655.

[23] C. M. Monsberger, W. Lienhart, and M. Hayden, “Distributed fiber optic sensing along driven ductile piles: Design, sensor installation and monitoring benefits”, en, *Journal of Civil Structural Health Monitoring*, vol. 10, no. 4, pp. 627–637, Sep. 2020, ISSN: 2190-5452, 2190-5479. DOI: 10.1007/s13349-020-00406-3. Accessed: Aug. 7, 2025. [Online]. Available: https://link.springer.com/10.1007/s13349-020-00406-3.

[24] B. Piątek, T. Howiacki, M. Kulpa, T. Siwowski, R. Sieńko, and Ł. Bednarski, “Strain, crack, stress and shape diagnostics of new and existing post-tensioned structures through distributed fibre optic sensors”, en, *Measurement*, vol. 221, p. 113 480, Nov. 2023, Publisher: Elsevier BV, ISSN: 0263-2241. DOI: 10.1016/j.measurement.2023.113480. Accessed: Jul. 24, 2025. [Online]. Available: https://linkinghub.elsevier.com/retrieve/pii/S0263224123010448.

[25] Luna Innovations Incorporated, *Odisi fiber optic sensor installation guide*, Application Note EN-FY1701, Revision B, Luna Innovations Incorporated, Roanoke, VA, USA, May 2017. [Online]. Available: https://www.lunainc.com.

[26] T. Howiacki, “Analysis of cracks in concrete structures with the use of distributed optical fibre measurements”, en,

[27] M. Weisbrich, K. Holschemacher, and T. Bier, *Comparison of Different Fiber Coatings for Distributed Strain Measurement in Cementitious Matrices*, en, Mar. 2020. DOI: 10.20944/preprints201911.0046.v2. Accessed: Jul. 24, 2025. [Online]. Available: https://www.preprints.org/manuscript/201911.0046/v2.

[28] T. Galkovski, Y. Lemcherreq, J. Mata-Falcón, and W. Kaufmann, "Fundamental Studies on the Use of Distributed Fibre Optical Sensing on Concrete and Reinforcing Bars", en, *Sensors*, vol. 21, no. 22, p. 7643, Nov. 2021, Publisher: MDPI AG, ISSN: 1424-8220. DOI: 10.3390/s21227643. Accessed: Jul. 24, 2025. [Online]. Available: https://www.mdpi.com/1424-8220/21/22/7643.

[29] Thorlabs, *SM1550P Polyimide-Coated Single Mode Fiber Spec Sheet*, Thorlabs Specification Sheet, TAP-SD-013 Rev C, 2025. Accessed: Oct. 11, 2025. [Online]. Available: https://www.thorlabs.com/drawings/3208b1888b1f74f4-42F5DE8A-9C84-7FEA-7CAFACBCC21BE866/SM1550P-SpecSheet.pdf.

[30] S.-C. Her, "Effect of Coating on the Strain Transfer of Optical Fiber Sensors", en,

[31] F. Falcetelli, L. Rossi, R. Di Sante, and G. Bolognini, "Strain Transfer in Surface-Bonded Optical Fiber Sensors", en, *Sensors*, vol. 20, no. 11, p. 3100, May 2020, ISSN: 1424-8220. DOI: 10.3390/s20113100. Accessed: Aug. 11, 2025. [Online]. Available: https://www.mdpi.com/1424-8220/20/11/3100.

[32] M. Weisbrich and K. Holschemacher, "Comparison between different fiber coatings and adhesives on steel surfaces for distributed optical strain measurements based on Rayleigh backscattering", en, 2018.

[33] A. Skontorp, K. Levin, and M. Benmoussa, "Surface-mounted optical strain sensors for structural health monitoring of composite structures", in *Proceedings of the 16th Technical Conference of the American Society for Composites*, Blacksburg, VA, USA, Sep. 2001, pp. 1–12.

[34] H. Abdel□Jaber and B. Glisic, "Monitoring of prestressing forces in prestressed concrete structures—An overview", en, *Structural Control and Health Monitoring*, vol. 26, no. 8, Aug. 2019, Publisher: Wiley, ISSN: 1545-2255, 1545-2263. DOI: 10.1002/stc.2374. Accessed: Jul. 24, 2025. [Online]. Available: https://onlinelibrary.wiley.com/doi/10.1002/stc.2374.

[35] X. Tan, Y. Bao, Q. Zhang, H. Nassif, and G. Chen, "Strain transfer effect in distributed fiber optic sensors under an arbitrary field", en, *Automation in Construction*, vol. 124, p. 103 597, Apr. 2021, Publisher: Elsevier BV, ISSN: 0926-5805. DOI: 10.1016/j.autcon.2021.103597. Accessed: Jul. 24, 2025. [Online]. Available: https://linkinghub.elsevier.com/retrieve/pii/S0926580521000480.

[36] F. Ansari and Y. Libo, "Mechanics of Bond and Interface Shear Transfer in Optical Fiber Sensors", en, *Journal of Engineering Mechanics*, vol. 124, no. 4, pp. 385–394, Apr. 1998, ISSN: 0733-9399, 1943-7889. DOI: 10.1061/(ASCE)0733-9399(1998)124:4(385). Accessed: Aug. 15, 2025. [Online]. Available: https://ascelibrary.org/doi/10.1061/%28ASCE%290733-9399%281998%29124%3A4%28385%29.

[37] F. Bastianini, R. Di Sante, F. Falcetelli, D. Marini, and G. Bolognini, "Optical Fiber Sensing Cables for Brillouin-Based Distributed Measurements", en, *Sensors*, vol. 19, no. 23, p. 5172, Nov. 2019, Publisher: MDPI AG, ISSN: 1424-8220. DOI: 10.3390/s19235172. Accessed: Jul. 24, 2025. [Online]. Available: https://www.mdpi.com/1424-8220/19/23/5172.

[38] I. Alj et al., "Experimental and Numerical Investigation on the Strain Response of Distributed Optical Fiber Sensors Bonded to Concrete: Influence of the Adhesive Stiffness on Crack Monitoring Performance", en, *Sensors*, vol. 20, no. 18, p. 5144, Sep. 2020, Publisher: MDPI AG, ISSN: 1424-8220. DOI: 10.3390/s20185144. Accessed: Jul. 24, 2025. [Online]. Available: https://www.mdpi.com/1424-8220/20/18/5144.

[39] G. Duck, G. Renaud, and R. Measures, "The mechanical load transfer into a distributed optical fiber sensor due to a linear strain gradient: Embedded and surface bonded cases", en,

[40] K. T. Wan, C. K. Y. Leung, and N. G. Olson, "Investigation of the strain transfer for surface-attached optical fiber strain sensors", en, *Smart Materials and Structures*, vol. 17, no. 3, p. 035 037, Jun. 2008, ISSN: 0964-1726, 1361-665X. DOI: 10.1088/0964-1726/17/3/035037. Accessed: Aug. 13, 2025. [Online]. Available: https://iopscience.iop.org/article/10.1088/0964-1726/17/3/035037.

[41] D. Li, “Strain transferring analysis of fiber Bragg grating sensors”, en, *Optical Engineering*, vol. 45, no. 2, p. 024 402, Feb. 2006, ISSN: 0091-3286. DOI: 10.1117/1.2173659. Accessed: Aug. 31, 2025. [Online]. Available: http://opticalengineering.spiedigitallibrary.org/article.aspx?doi=10.1117/1.2173659.

[42] “Analysis of the strain transfer mechanism between a truly distributed optical fiber sensor and the surrounding medium”, en, in *Concrete Repair, Rehabilitation and Retrofitting III*, 0th ed., CRC Press, Aug. 2012, pp. 288–289, ISBN: 978-0-429-21717-3. DOI: 10.1201/b12750-122. Accessed: Jul. 24, 2025. [Online]. Available: https://www.taylorfrancis.com/books/9780203124253/chapters/10.1201/b12750-122.

[43] M. Yan, X. Tan, S. Mahjoubi, and Y. Bao, “Strain transfer effect on measurements with distributed fiber optic sensors”, en, *Automation in Construction*, vol. 139, p. 104 262, Jul. 2022, Publisher: Elsevier BV, ISSN: 0926-5805. DOI: 10.1016/j.autcon.2022.104262. Accessed: Jul. 24, 2025. [Online]. Available: https://linkinghub.elsevier.com/retrieve/pii/S0926580522001352.

[44] D. C. Betz, G. Thursby, B. Culshaw, and W. J. Staszewski, “Acousto-ultrasonic sensing using fiber bragg gratings”, *Smart Materials and Structures*, vol. 12, no. 1, pp. 122–128, 2003, ISSN: 0964-1726.

[45] Y. B. Lin, K. C. Chang, J. C. Chern, and L. A. Wang, “Packaging methods of fiber-bragg grating sensors in civil structure applications”, *IEEE Sensors Journal*, vol. 5, no. 3, pp. 419–424, 2005, ISSN: 1530-437X.

[46] W. Y. Li, C. C. Cheng, and Y. L. Lo, “Investigation of strain transmission of surface-bonded fbgs used as strain sensors”, *Sensors and Actuators A: Physical*, 2008, ISSN: 0091-3286.

[47] J. Zhou, Z. Zhou, and D. Zhang, “Study on strain transfer characteristics of fiber bragg grating sensors”, *Journal of Intelligent Material Systems and Structures*, 2010, ISSN: 1045-389X.

[48] K. Jahani and A. Nobari, “Identification of dynamic (young’s and shear) moduli of a structural adhesive using modal based direct model updating method”, *Experimental Mechanics*, vol. 48, no. 5, pp. 599–611, 2008, ISSN: 0014-4851.

[49] “Monitoring of shear cracking in partially prestressed concrete beams by distributed optical fiber sensors”, en, in *Maintenance, Monitoring, Safety, Risk and Resilience of Bridges and Bridge Networks*, 1st ed., CRC Press, Nov. 2016, pp. 225–225, ISBN: 978-1-315-20768-1. DOI: 10.1201/9781315207681-79. Accessed: Jul. 24, 2025. [Online]. Available: https://www.taylorfrancis.com/books/9781498777032/chapters/10.1201/9781315207681-79.

[50] B. Richter, M. Herbers, and S. Marx, “Crack monitoring on concrete structures with distributed fiber optic sensors—Toward automated data evaluation and assessment”, en,

[51] A. Jędrzejewska et al., “Standardized models for cracking due to restraint of imposed strains—the state of the art”, *Structural Concrete*, vol. 24, no. 4, pp. 5388–5405, 2023. DOI: https://doi.org/10.1002/suco.202200301. eprint: https://onlinelibrary.wiley.com/doi/pdf/10.1002/suco.202200301. [Online]. Available: https://onlinelibrary.wiley.com/doi/abs/10.1002/suco.202200301.

[52] G. Rodriguez, J. R. Casas, and S. Villalba, “Shear crack width assessment in concrete structures by 2D distributed optical fiber”, en, *Engineering Structures*, vol. 195, pp. 508–523, Sep. 2019, Publisher: Elsevier BV, ISSN: 0141-0296. DOI: 10.1016/j.engstruct.2019.05.079. Accessed: Jul. 24, 2025. [Online]. Available: https://linkinghub.elsevier.com/retrieve/pii/S0141029618330682.

[53] R. Regier and N. A. Hoult, “Distributed Strain Behavior of a Reinforced Concrete Bridge: Case Study”, en, *Journal of Bridge Engineering*, vol. 19, no. 12, Dec. 2014, Publisher: American Society of Civil Engineers (ASCE), ISSN: 1084-0702, 1943-5592. DOI: 10.1061/(asce)be.1943-5592.0000637. Accessed: Jul. 24, 2025. [Online]. Available: https://ascelibrary.org/doi/10.1061/%28ASCE%29BE.1943-5592.0000637.

[54] “Odisi 6100: Optical distributed sensor interrogator — data sheet”, Luna Innovations Incorporated, 3155 State Street, Blacksburg, VA, USA, Tech. Rep. LTODiSI6 Rev4, May 2018, Product data sheet. [Online]. Available: https://www.lunainc.com.

[55] M. S. Ibrahim, Y. Yang, M. Roosen, and M. Hendriks, “Challenges on the shear behavior of existing continuous precast girder bridges”, Sep. 2022.

[56] E. A. Andrade Borges, Y. Yang, M. A. Roosen, and M. A. N. Hendriks, “Concrete-to-concrete interface behaviour in precast girder bridges made continuous: Deficiencies and challenges”, in *Proceedings of the 15th fib International PhD Symposium in Civil Engineering*, G. L. Balázs, S. Sólyom, and S. Foster, Eds., International Federation for Structural Concrete (fib), 2024, pp. 465–472.

[57] “Dtg coating ormocer®-t for temperature sensing applications”, FBGS International N.V., Bell Telephonelaan 2H, B-2440 Geel, Belgium, Tech. Rep., Feb. 2015, Application note. [Online]. Available: https://www.fbgs.com.

[58] “Drei bond 8142: Two-component epoxy adhesive — technical data sheet”, Drei Bond Polska Sp. z o.o., ul. Bagrowa 1, 30-733 Kraków, Poland, Tech. Rep., Jun. 2022, Rev. 15.06.2022 (original issue: 06.2021). [Online]. Available: https://www.dreibond.com.pl.

[59] H. Becks, M. Högemann, J. Hegger, and M. Classen, “Assessing crack formation and strain distribution in concrete structures using externally installed fiber optic sensors”, en, *Case Studies in Construction Materials*, vol. 22, e04744, Jul. 2025, ISSN: 22145095. DOI: 10.1016/j.cscm.2025.e04744. Accessed: Aug. 12, 2025. [Online]. Available: https://linkinghub.elsevier.com/retrieve/pii/S221450952500542X.

[60] G. Rodríguez, J. R. Casas, and S. Villaba, “Cracking assessment in concrete structures by distributed optical fiber”, en, *Smart Materials and Structures*, vol. 24, no. 3, p. 035 005, Mar. 2015, ISSN: 0964-1726, 1361-665X. DOI: 10.1088/0964-1726/24/3/035005. Accessed: Aug. 11, 2025. [Online]. Available: https://iopscience.iop.org/article/10.1088/0964-1726/24/3/035005.

[61] Tokyo Measuring Instruments Laboratory (TML), *Concrete Material Use Strain Gauge*, TML Official Website, P-series strain gauges; operational temperature –20 °C to +80 °C, polyester backing, gauge factor ≈2.1, 2025. Accessed: Oct. 11, 2025. [Online]. Available: https://tml.jp/e/product/strain_gauge/concrete.html.

[62] Althen Sensors, *Fdrf603 series laser triangulation sensor — technical specifications*, https://www.althensensors.com/sensors/laser-position-sensors/single-point-laser-distance-sensors/fdrf603-series-laser-triangulation-sensor/#technical-specifications, Accessed: 2025-10-13, 2025.

[63] Nerve-Sensors, *Nerve-sensors*, https://nerve-sensors.com/, Accessed: Oct. 29, 2025.

[64] O. Zeeland, *Reden waarom man zich opsloot in de zeelandbrug groot raadsel: Provincie doet aangifte*, https://www.omroepzeeland.nl/nieuws/17678405/reden-waarom-man-zich-opsloot-in-de-zeelandbrug-groot-raadsel-provincie-doet-aangifte, Online; accessed Oct. 15, 2025, 2025.

[65] Provincie Zeeland, *Zeelandbrug*, https://www.zeeland.nl/onderwerpen/verkeer-en-openbaar-vervoer/zeelandbrug, Online; accessed Oct. 15, 2025, 2025.

[66] H. T. Hoving, A. C. Krijn, and J. H. van Loenen, “Brug over de oosterschelde”, *Cement*, vol. XVI, no. 11, pp. 685–693, 1964.

[67] V. Stoop, “Investigation of monitoring strategies for the Zeelandbrug”, en,

[68] A. A. Chávez, A. Ulfberg, J. Gonzalez-Libreros, L. Elfgren, and G. Sas, “Data validation of strain-based monitoring systems in low temperature conditions, case study: The kalix bridge”, in *Proceedings of the International Conference on Bridge Maintenance, Safety, Management, Life-Cycle Sustainability and Innovations*, Chapter in edited volume, Cham: Springer, 2023, pp. –-. DOI: 10.1007/978-3-031-32511-3_101.

A

Crack Widths Identified from DFOS Measurements

A.1. DFOS identified crack widths for Specimen 1 (R3D8-AR47)

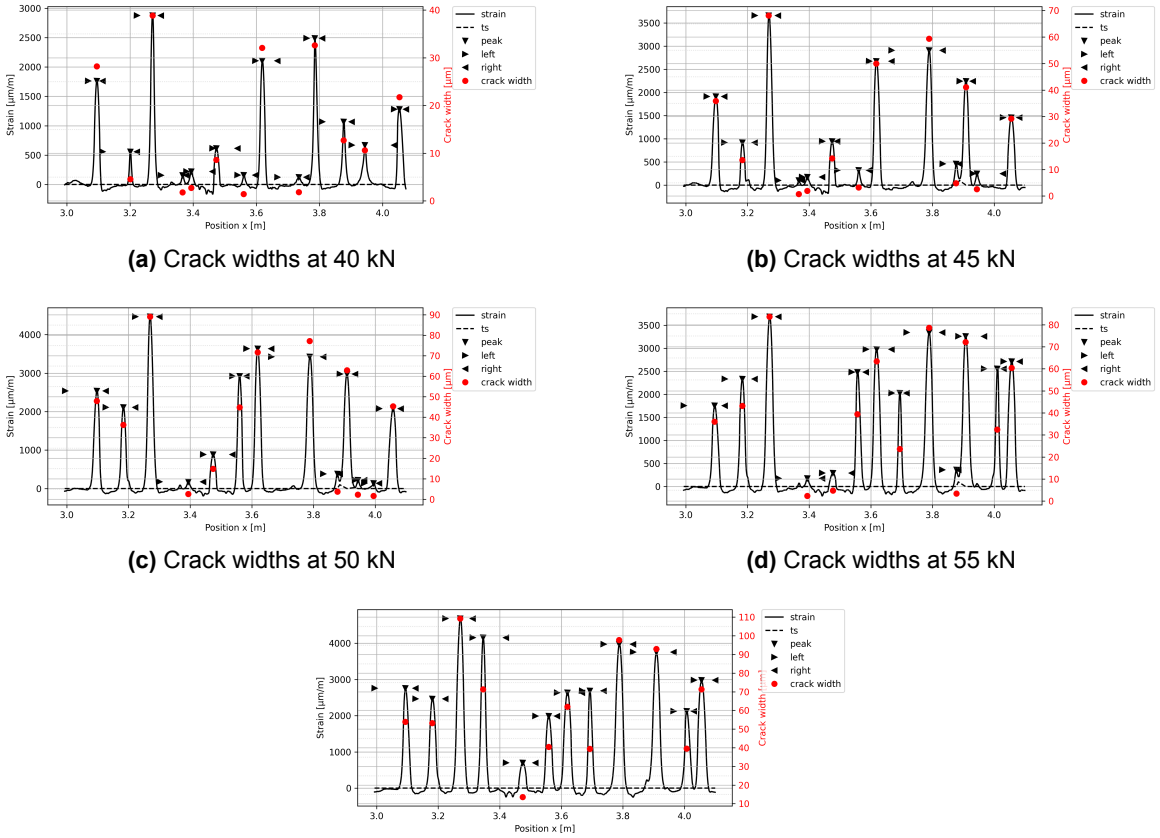

(a) Crack widths at 40 kN

(b) Crack widths at 45 kN

(c) Crack widths at 50 kN

(d) Crack widths at 55 kN

(e) Crack widths at 65 kN

Figure A.1: DFOS identified crack widths for Specimen 1 (R3D8-AR47) at different load levels.

A.2. DFOS identified crack widths for Specimen 2 (R4D8-DB)

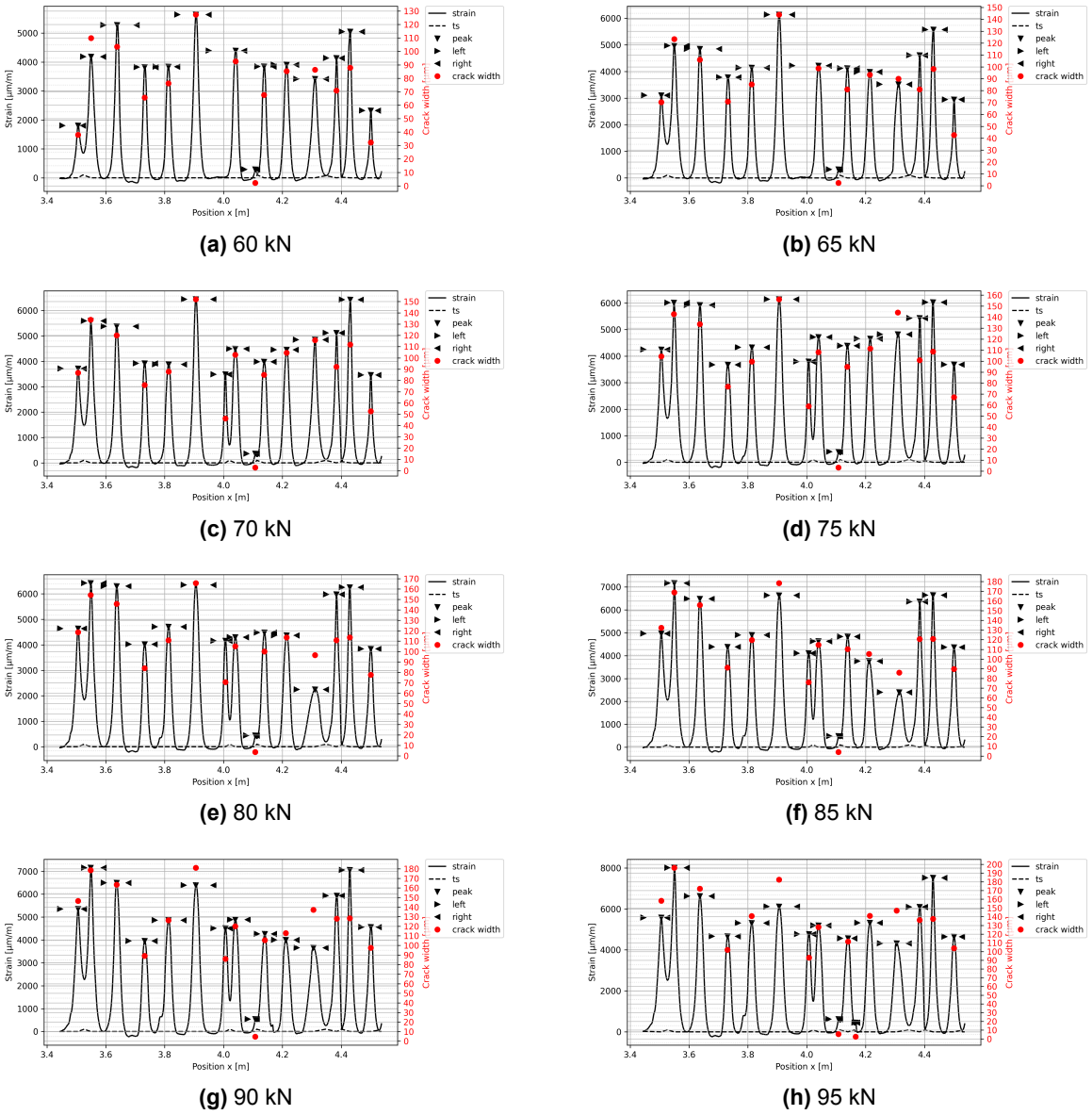

(a) 60 kN **(b)** 65 kN

(c) 70 kN **(d)** 75 kN

(e) 80 kN **(f)** 85 kN

(g) 90 kN **(h)** 95 kN

Figure A.2: DFOS identified crack widths for Specimen 2 (R4D8-DB) at different load levels.

A.3. DFOS identified crack widths for Specimen 3 (R3D10-CN)

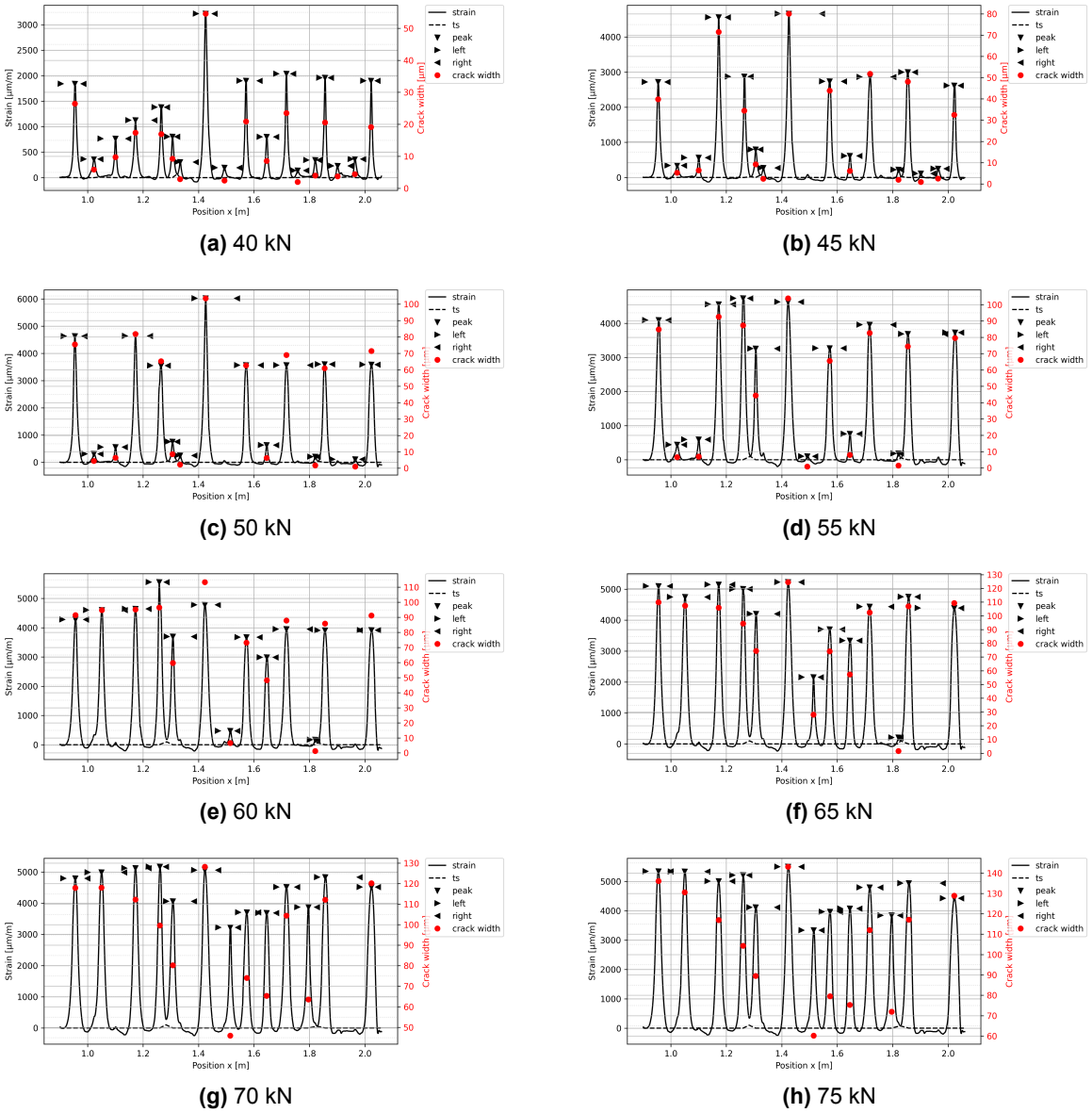

(a) 40 kN **(b)** 45 kN

(c) 50 kN **(d)** 55 kN

(e) 60 kN **(f)** 65 kN

(g) 70 kN **(h)** 75 kN

Figure A.3: DFOS identified crack widths for Specimen 3 (R3D10-CN), load levels 40–75 kN.

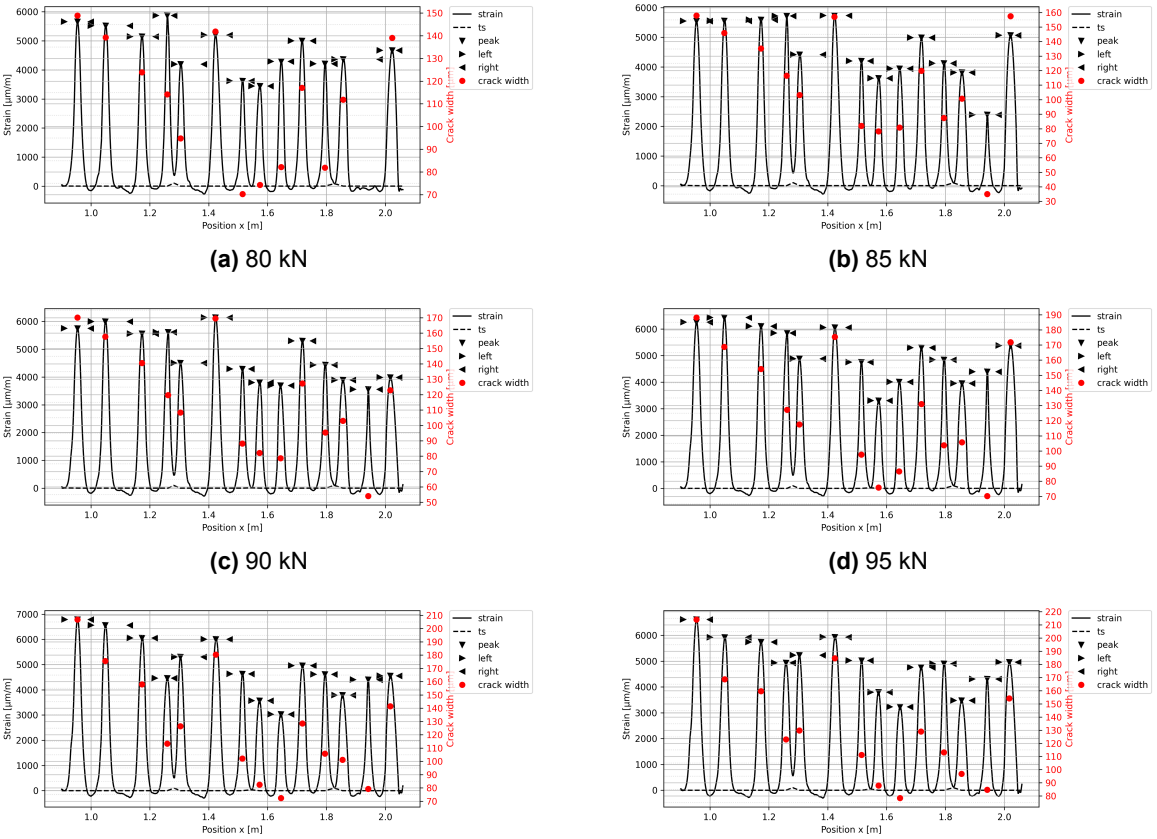

(a) 80 kN **(b)** 85 kN

(c) 90 kN **(d)** 95 kN

(e) 100 kN **(f)** 105 kN

Figure A.4: DFOS identified crack widths for Specimen 3 (R3D10-CN), load levels 80–105 kN.

A.4. DFOS identified crack widths for Specimen 4 (R3D12-AR14)

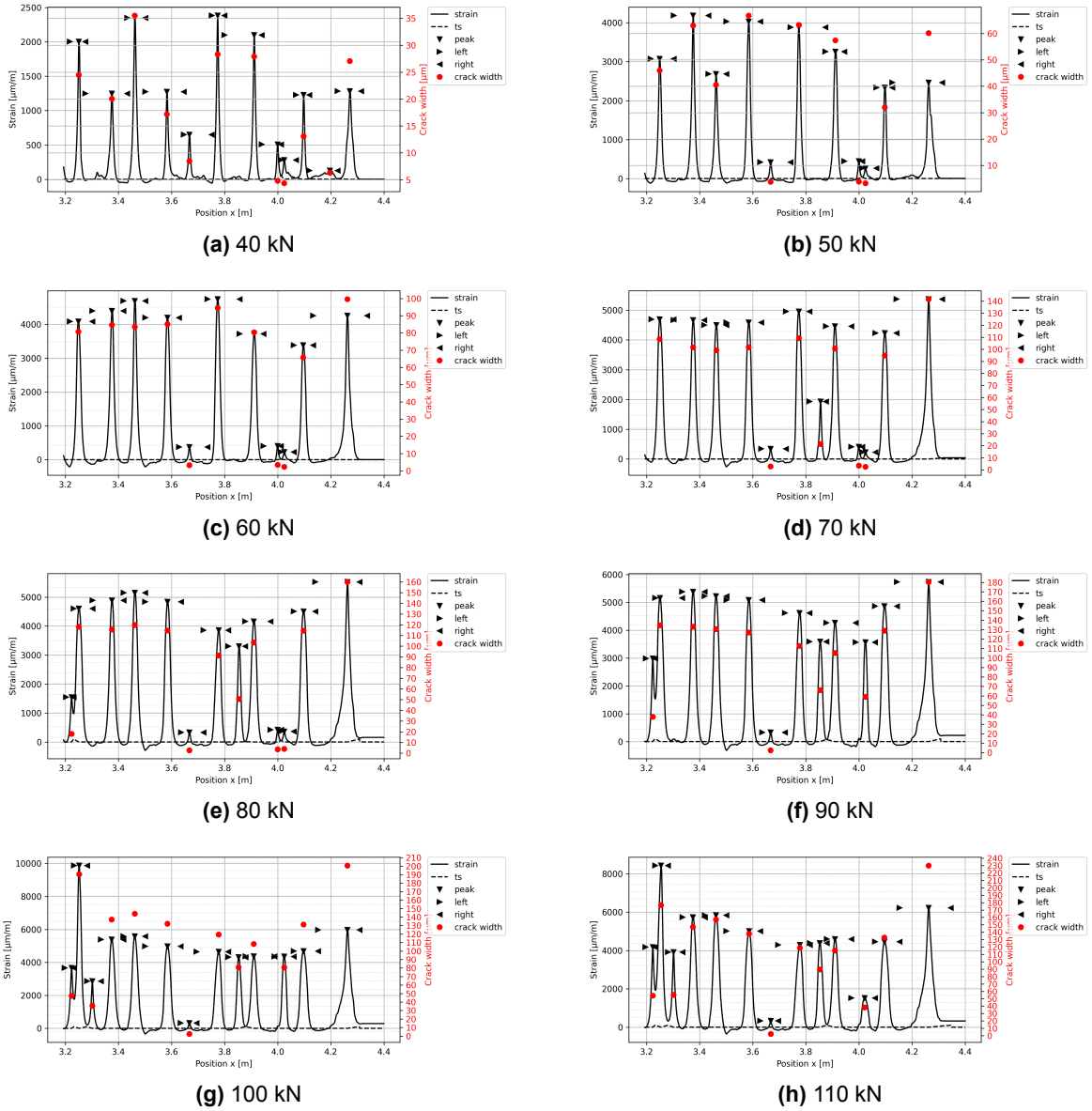

(a) 40 kN **(b)** 50 kN

(c) 60 kN **(d)** 70 kN

(e) 80 kN **(f)** 90 kN

(g) 100 kN **(h)** 110 kN

Figure A.5: DFOS identified crack widths for Specimen 4 (R3D12-AR14), load levels 40–110 kN.

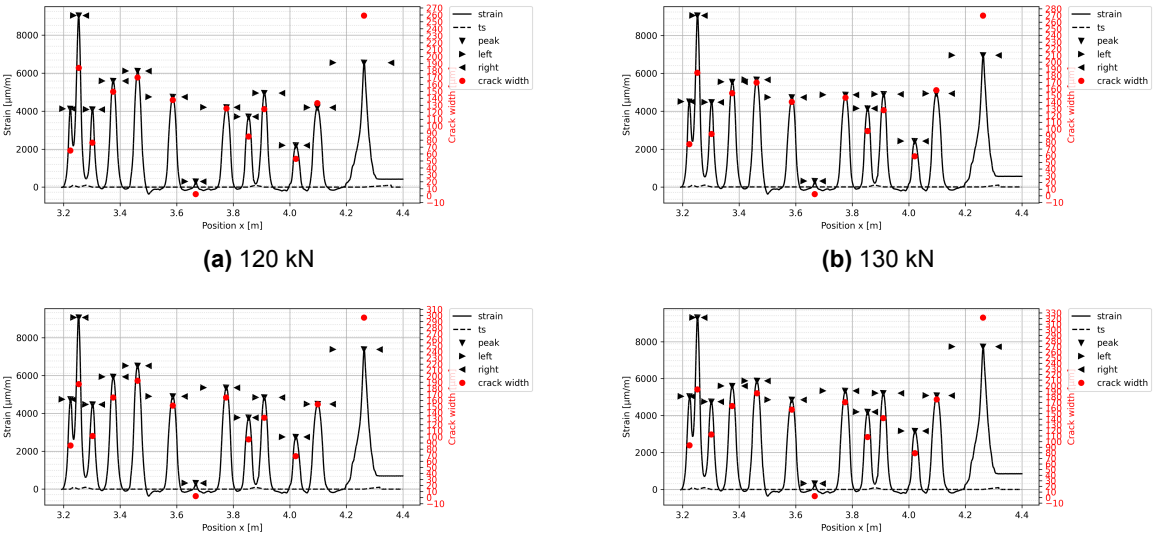

(a) 120 kN **(b)** 130 kN

(c) 140 kN **(d)** 150 kN

Figure A.6: DFOS identified crack widths for Specimen 4 (R3D12-AR14), load levels 120–150 kN.